MICROMECHANICAL BEHAVIOR INVESTIGATION OF METALLIC GLASSES

LIU ZHIYUAN

PhD

The Hong Kong Polytechnic University

2012

The Hong Kong Polytechnic University

Department of Mechanical Engineering

Micromechanical Behavior Investigation of Metallic Glasses

Liu Zhiyuan

A thesis submitted in partial fulfillment of the requirements for

the degree of Doctor of Philosophy

August 2011

CERTIFICATE OF ORIGINALITY

I hereby declare that this thesis is my own work and that, to the best of my knowledge and belief, it reproduces no material previously published or written, nor material that has been accepted for the award of any other degree or diploma, except where due acknowledgement has been made in the text.

_____ (Signed)

_____Liu Zhiyuan_____(Name of student)

Dedication

This dissertation is dedicated with love to my parents and Xiaoxiao, who always support my research studies and bring the greatest joy into my life.

ABSTRACT

As a new class of materials, metallic glasses (MGs) have stimulated extensive interest in the academic community, because they possess unique disordered atomic structure lacking long range translational symmetry, and thus have excellent mechanical and chemical properties such as high strength, large fracture toughness and good corrosion resistance. These excellent properties render MGs with a great potential for engineering applications. However, low plasticity at room temperature seriously hinders MGs' application, besides the atomic structure of the MGs has not been well captured and the deformation mechanism has not been fully understood. In this thesis, I start with an investigation of the cooling rate effect on the elastic properties of MGs using quasi-static and dynamic methods, then extend the investigation to the plastic deformation of MGs and characterize the speed of shear band as a function of shear offset.

Cooling rate is thought to play the most important role in the vitrification of glass-forming liquids. It is known that the cooling rate can affect MGs' atomic structure and thus may possibly has influence on their mechanical properties. Quasi-static micromechanical study of the cooling-rate effect on Young's moduli and hardness of the as-cast bulks and melt-spun ribbons for $Zr_{55}Pd_{10}Cu_{20}Ni_5Al_{10}$ MG was carried out. Using the classic nanoindentation method, the Young's moduli of the ribbon samples obtained at higher cooling rates were measured which appeared to be much lower than those of the bulk samples. Through further experiments on slice samples cut from the as-cast bulks

MG and finite-element (FE) analyses, we have clearly demonstrated that the measured difference in elastic moduli was mainly caused by the sample thickness effect in nanoindentation tests. To overcome such a confounding effect, microcompression experiments were performed on the as-cast and as-spun MG samples, respectively. Being consistent with the findings from nanoindentation, the microcompression results showed that the cooling rate, as ranging from ~10^2 to ~10^6 K/s, essentially has no influence on the Young's modulus and hardness of the MGs.

Then, we turn to using dynamic microcompression test to investigate the cooling rate effect. First of all, to understand and analyze the anelastic deformation of MGs, theoretical framework based on the energy barrier concept was developed. The theoretical results clearly show that the stress-induced reversible local structural transition in MGs is equivalent to a Kelvin-type anelastic deformation process, and this reflects a core-shell atomic configuration in MGs, which consists of free volume zones (FVZs) and surrounding dense packed atomic clusters. Using this theoretical model, dynamic test results of micropillars carved out from bulk and ribbon MGs were analyzed, no discernable difference in effective modulus and viscosity can be revealed, indicating that similar content of dense packed cluster and FVZs in the bulk and ribbon MGs despite the cooling rate difference in about four orders of magnitude.

Apart from the cooling rate effect, the shear bands, as the plastic deformation carrier of MGs, were investigated. Important experimental finding and theoretical analysis of the shear-band speed measured in a variety of bulk metallic-glasses (BMGs) were presented.

Unlike the other research work, in which the shear-band speed was regarded as a constant, our study, based on carefully designed loading-holding cyclic tests, reveals that the speed of shear band correlates with its resultant shear offset. Such a correlation arises as a ‘size’ effect, which could be rationalized by the energy balance principle.

LIST OF PUBLICATIONS

1. **Liu Z Y**, Yang Y. A Mean-Field Model for Anelastic Deformation in Metallic Glasses, under review.

2. **Liu Z Y**, Yang Y, Liu C T. Size-Affected Shear-Band Speed in Metallic Glasses, **Applied Physics Letters**, (2011) vol. 99 pp. 171904.

3. **Liu Z Y**, Guo S, Liu X J, Ye J C, Yang Y, Wang X L, Yang L, An K, Liu C T. Micromechanical characterization of casting-induced inhomogeneity in an Al0.8CoCrCuFeNi High-entropy alloy. **Scripta Materialia** (2011) vol. 64 pp. 868-871.

4. **Liu Z Y**, Yang Y, Guo S, Liu X J, Lu J, Liu Y H, Liu C T. Cooling rate effect on Young's modulus and hardness of a Zr-based metallic glass. **Journal of Alloys and Compounds** (2011) vol. 509 pp. 3269-3273.

ACKNOWLEDGMENTS

I wish to express my deep gratitude and sincere appreciation to my supervisor, Professor LIU Chain Tsuan and Dr. YANG Yong, for their timely and untiring guidance, and personal commitment throughout this research. Their exceptional insight into structure and mechanical properties of metallic glasses has deeply fascinated me. This dissertation could definitely not be possible without their invaluable supervision.

In addition, special thanks must be extended to my research team members Dr. Liu Xiong-jun, Dr. Guo Sheng and Dr. Wang Qing for generously sharing their expertise and ideas. I also wish to thank the experimental and technical support provided by Mr. Curtis Ng and Mr. Wong Kwok-wai in the Department of Mechanical Engineering, Mr. Yeung in the Materials Research Center of The Hong Kong Polytechnic University.

Last but not least, I would like to express my utmost love and gratitude to my family, and my wife for their love, understanding, patience and endless encouragement over the years.

TABLES OF CONTENTS

LIST OF FIGURES

LIST OF TABLES

CHAPTER 1 Introduction

Metallic glass (MG) is a new class of material characterized by a series of impressive mechanical properties and having great potential for broad engineering applications [1, 2]. Over the past decades, it has attracted considerable attention, and substantial research efforts have been dedicated to solving puzzles in this field.

1.1 Research Background

Metallic glasses or amorphous metallic alloys are metals and metallic alloys lack of long range periodicity in atomic structure. Normally, they are formed by rapid solidification of the alloys from their liquid states. Solidification occurs so rapidly that there is no time for the crystallization to take place, thus the atoms are frozen to metastable solid state in their liquid configuration. These amorphous structures contribute to many superior mechanical, chemical and electrical properties compared with the traditional crystalline metals, for example, metallic glasses are exceptionally hard and have extremely high strengths; they have excellent corrosion resistance; and some of them are good soft magnetic materials with distinctly lower magnetic losses.

Traditionally, metallic materials are utilized in their crystalline state, because metals tend to crystallize during the solidification process based on the thermodynamics theory. The first metallic glass, $Au_{75}Si_{25}$, in a thin disk form with a thickness less than 0.1 mm, was made by Duwez et al. in 1960, who rapidly solidified the liquid at rate approaching 10^6 K/s through the process of splat quenching [3]. Then, in 1974, the first bulk metallic glass (BMG), which is defined by the size with one dimension larger than 1 mm, Pu-Cu-Si was prepared by Chen et al. utilizing the suction casting method with a cooling rate of about 10^3 K/s [4]. Since the first discovery of the BMG, great enthusiasm has been stimulated to study this class of metallic materials. Extensive efforts have been devoted to enlarging the size of the metallic glasses and to utilizing their excellent properties in more fields. Considerable progresses have been achieved in the synthesis of larger metallic glasses at relatively slower quenching rates [5-8], and numerous metallic glasses with various compositions have been developed so far.

In the meantime, in order to better utilize these newly emerging materials, a great amount of investigations have been carried out to reveal the underlying mechanisms which give rise to the impressive mechanical, physical and chemical properties of BMGs. To this end, various structural/mechanistic models and theories have been developed, which will be described briefly in the following text. From the structure aspect, metallic glasses have no regular arrangement of atoms; in other words, the atomic arrangement appears random. Since there is no periodical symmetry in these non-crystalline materials, it is difficult to characterize their atomic configuration. Experimentally, traditional methods of structural characterization established for crystalline materials, such as X-ray diffraction (XRD),

transmission electron microscope (TEM), small angle neutron scattering, have been employed to characterize the atomic configuration of MGs. Based on these methods, information related to the statistical aspects of the atomic structure can be extracted. However, a 3D atomic structure is still absent because of the limitation of the experimental methods. Apart from the experimental observations, computer simulations have also been carried out to reveal the atomic structure of MGs. Various structural models, such as Bernal's dense random packing model [9], Gaskel's short range order model [10] and the solute-centered quasi-equivalent cluster model [11, 12], have been proposed.

Another enduring attraction of MGs is their impressive mechanical properties owing to the amorphous structure. The deformation mechanism of MGs has been proven to be of fundamental scientific interest [13], and can provide theoretical support for their application as engineering materials. MGs generally possess elastic moduli on the same order as those of traditional engineering metals, but they have significantly higher strengths and hardness than their crystalline counterparts at room temperature (as shown in Figure 1.1). However, when the plastic deformation occurs, they usually suffer from a strong tendency for shear localization or shear banding, and as a result get failure macroscopically at ambient temperature [14]. Nevertheless, the vein pattern presented on the fracture surface of MGs, as shown in Figure 1.2, clearly indicates that MGs are capable of carrying a certain amount of plastic shear flow in the localized shear plane [15, 16]. The consequent promise of the high strength with localized plasticity and decent

fracture toughness stimulated considerable research effort devoted to the investigation on the deformation mechanism of MGs.

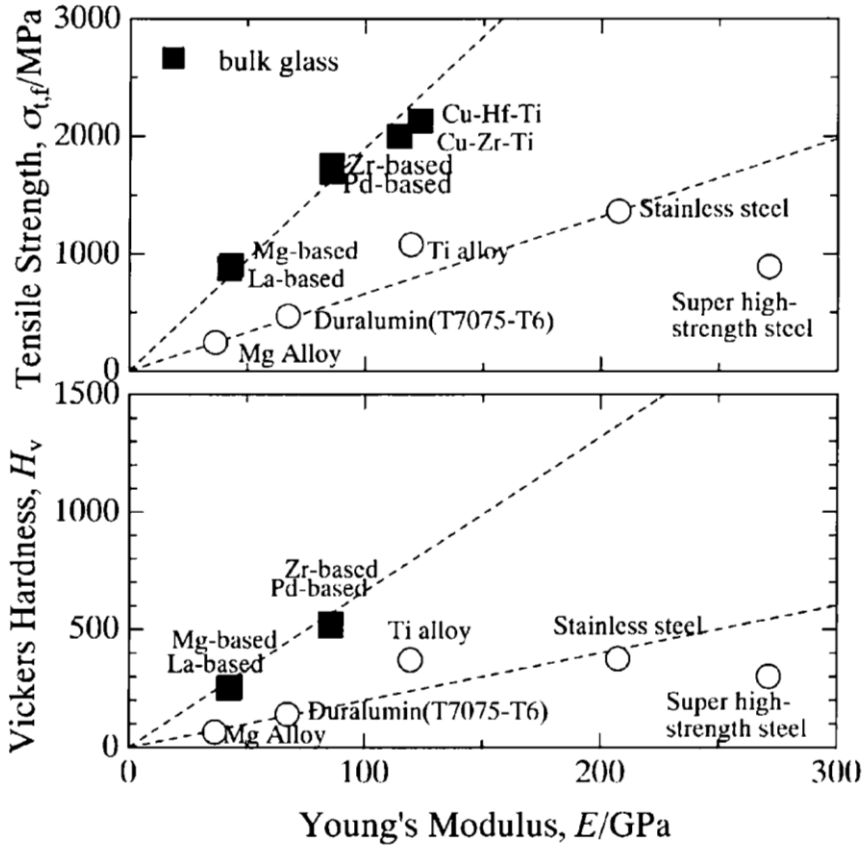

Figure 1.1. The relations between mechanical properties of typical BMGs: (a) tensile fracture strength with Young's modulus; (b) Vickers hardness with Young's modulus [2].

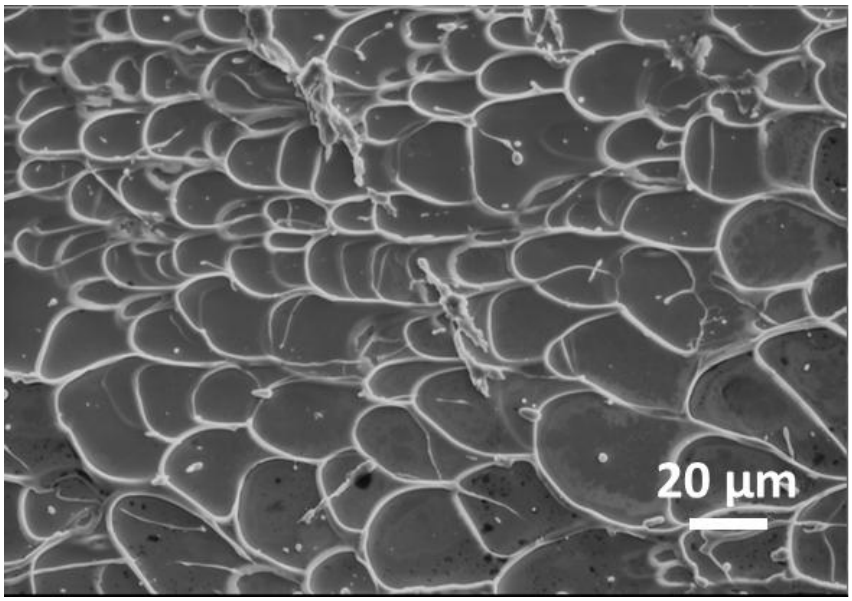

Figure 1.2. The vein pattern on a typical facture surface of a Zr-based metallic glass suggesting legitimate plastic shear flow occurs in shear plane.

It is widely accepted that the fundamental process underlying MGs' deformation must be the local rearrangement of atoms that can accommodate the shear strain; however, the exact nature of local atomic motion during the deforming process is not yet fully understood. Two models of such local rearrangement unit are depicted in the schematic drawing of Figure 1.3. One is the free volume model, which was developed by Turnbull and Spaepen [17, 18]. This model essentially views deformation as a series of discrete atomic jumps in the glass, as depicted schematically in Figure 1.3(a), these jumps are obviously favored near sites of high free volume which can more readily accommodate them. The other model is the shear transformation zone (STZ) model [19], which takes deformation unit as a local cluster of atoms that undergoes an inelastic shear distortion

under applied stress, as presented in Figure 1.3(b). These two models have been widely used to interpret the basic deformation features of MGs [13, 20].

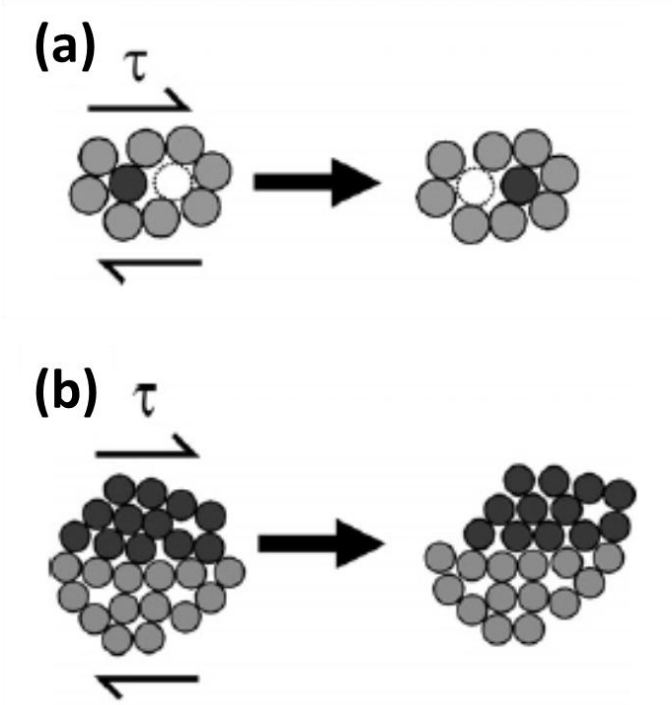

Figure 1.3. Two-dimensional schematics of the atomistic deformation mechanisms proposed for metallic glasses. (a) Free volume model; (b) Shear transformation zone (STZ) Model.

1.2 Synthesis of Metallic Glasses

Metallic glass was firstly produced by rapidly solidifying molten metal with high cooling rates of about 10^6 Ks^{-1} [3]. The prepared MG possesses an interesting disordered atomic structure, which is quite different from the periodic configuration of ordinary crystalline

metals. This early success of preparation of metal alloys in amorphous state stimulated enormous enthusiasm from the academic community, and led to the development of a variety of techniques to obtain metallic glasses in different sizes and shapes (ribbons, wires, powders, etc.). Generally, high cooling rate can be achieved by promoting rapid heat removal from the bulk. The simplest way is to maximize the contact area between melt and cooling medium by rapidly increasing the liquid alloy surface area. In the following sections, four primary techniques adopted to prepare MGs will be described.

Sputtering and Evaporation Techniques

Sputtering and evaporation techniques are based on an atom-by-atom constitution of the amorphous alloy and require that the kinetic energy of the condensing atom exceed the binding energy of the atoms in the substrate surface. The substantially high quench rate inherent in sputtering and evaporation methods (over 10^{18} K/s) allows the formation of some metallic glasses which cannot be produced by melt quenching methods, but the sample mass accumulation rate is very low.

Splat Quenching Technique

The earliest melt quenching method used in fabrication of amorphous alloy was the gun splat quenching technique [3]. In the process, the molten alloy is atomized by expulsion from a shock tube, and propelled against a substrate surface having high thermal conductivity. A large contact area conducting the heat of molten alloy in short time leads to thin discs of amorphous alloys. Numerous variations of the splat quenching techniques

have evolved, for example, the piston and anvil and twin piston methods which rapidly flatten and quench molten alloy droplets between impacting substrate surfaces.

Melt Spinning Technique

Akin to that used for manufacturing synthetic textile fibers, the melt spinning process involves ejecting the molten metal through an orifice to solidify the melt stream either in flight or against a chill. If the melt stream is solidified in flight, the process is referred to as free flight melt spinning (FFMS), while if it is solidified on a chill, the process is called chill block melt spinning (CBMS). The CBMS process is the most commonly used methods to fabricate amorphous alloys. Specifically, in the CBMS process, constituent elements of the alloy are melted first, then through an orifice under external force the molten metal jet is directed onto a cold rotating heat sink, where the jet is reshaped and allowed to solidify with high quenching rate, and amorphous structure are frozen into the solid state, forming metallic glass. The typical quenching rates achieved in this process are about 10^5-10^6 K/s, and dimensions of the ribbons produced using this technique are about 2~5 mm in width and 20~50 μm in thickness. This technique has been widely used in the synthesis of amorphous alloy in the early stage of MGs research.

Copper Mold Casting Technique

Copper mold casting is the most common and popular method to synthesize bulk metallic glasses. With this technique, an alloy is melted repeatedly several times using an electric arc or induced current to ensure compositional homogeneity. After that, the metallic melt

is poured into a copper mold where it solidifies rapidly because of the rapid heat extraction by the copper mold. Usually, a low pressure (about 0.05 MPa) is applied to eject the molten metal from the crucible toward the mold, in order to ensure the fully filling of the mold and lager contact area between the sample and mold. Generally, the casting was performed in inert atmosphere to avoid oxidation. Figure 1.4 shows a schematic drawing of the equipment used for copper mold casting [21].

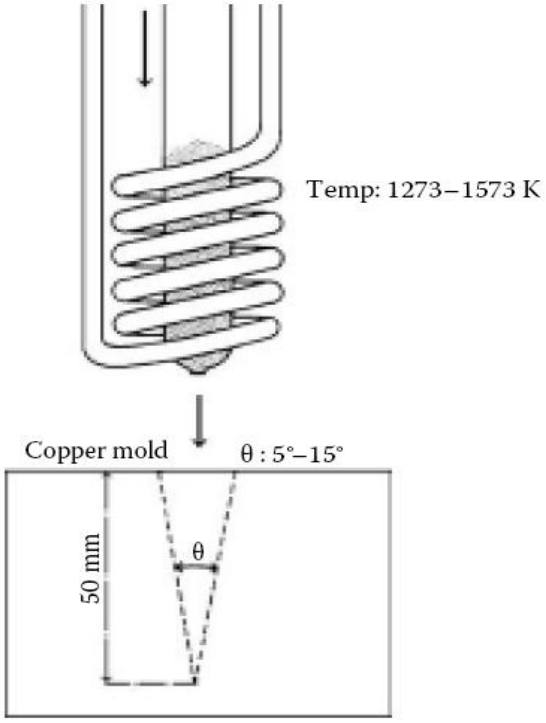

Figure 1.4. Schematic drawing of the equipment used to prepare Bulk MG by the copper mold casting technique.

The mold used in copper mold casting technique can be made into different forms, among which the most common and simplest form is the rod shaped cavity with a preset length. Researchers often use molds with cavities of different internal diameters to determine the maximum size of the alloy that could be produced in a fully glassy state, i.e. to examine the glass forming ability (GFA) of the alloy.

1.3 Structure of Metallic Glasses

The structure of metallic glasses has been a long-standing puzzle, as the amorphous structure lacks a long-range translational symmetry, however, topological and chemical short to medium range order are expected to exist locally in these alloys, due to the high atomic packing density and varying chemical affinity among the constituent elements in MGs.

Extensive studies have been carried out to characterize the amorphous structure using experimental techniques and computer simulations. In the meantime, great efforts have been devoted to utilizing the structural features to explain the thermodynamic phenomenon and mechanical behaviors of MGs.

1.3.1 Structure Characterization

The structure of MGs cannot be characterized by lattice parameters as usually in crystalline materials, and instead the following terminologies are often used to describe the amorphous structure.

Pair Distribution Function

Traditionally, the structure of liquids and glasses is described in terms of the pair distribution function (PDF), which represents the probability of finding an atom as function of distance from a center atom. From PDF, short range order, shell structure, and distribution of interatomic distances, can be clearly seen [22]. For binary alloy, the partial PDF can be expressed as

$$g_{\alpha\beta}(r) = \frac{N}{4\pi r^2 \rho N_\alpha N_\beta} \sum_{i=1}^{N_\alpha} \sum_{j=1}^{N_\beta} \delta(r - |\vec{r}_{ij}|) \tag{1.1}$$

where r is the distance from the center atom, ρ is the number density of atoms in the system with N atoms, N_α and N_β is the atom number of type α and type β atoms, respectively, $|\vec{r}_{ij}|$ is the interatomic distance between two atom i (of α type) and atom j (of β type). For the mono-element alloy, there only has one type of atoms in the system, and Equation 1.1 can be written as:

$$g(r) = \frac{1}{4\pi r^2 \rho N} \sum_{i=1}^{N} \sum_{j=1, j\neq i}^{N} \delta(r - |\vec{r}_{ij}|) \tag{1.2}$$

A typical PDF for liquid Cu is shown in Figure 1.5(a). Through analyzing the position, width and intensity of the peaks at small distance, the structure information of the amorphous alloy can be extracted. Conventionally, the atomic make-up and configuration

of the nearest neighbor shell, which constitute the short range order (SRO), contribute to the first peak in the PDF curve. The structural features in PDF beyond the first peak to a distance up to 1-2 nm represent medium range order (MRO). At larger *r*, the PDF gradually converges to unity, which means that no long-range order exists.

Structure Factor

Another term, that widely employed to describe the structure of MGs, is the structure factor, *S(q)*. Essentially, *S(q)-1* is the Fourier transformation of the pair distribution function [23], can be written as:

$$S(q)-1=\frac{4\pi\rho}{q}\int_0^\infty r[g(r)-1)]\sin(qr)dr \qquad (1.3)$$

where $q=4\pi\sin\theta/\lambda$, θ is half of the scattering angle and λ is the neutron wavelength. The structure factor of the Cu liquid is shown in Figure 1.5(b), corresponding to the PDF in Figure 1.5(a). With the structure factor measured in X-ray or neutron experiment, one can perform Fourier transformation to obtain the PDF of the testing sample.

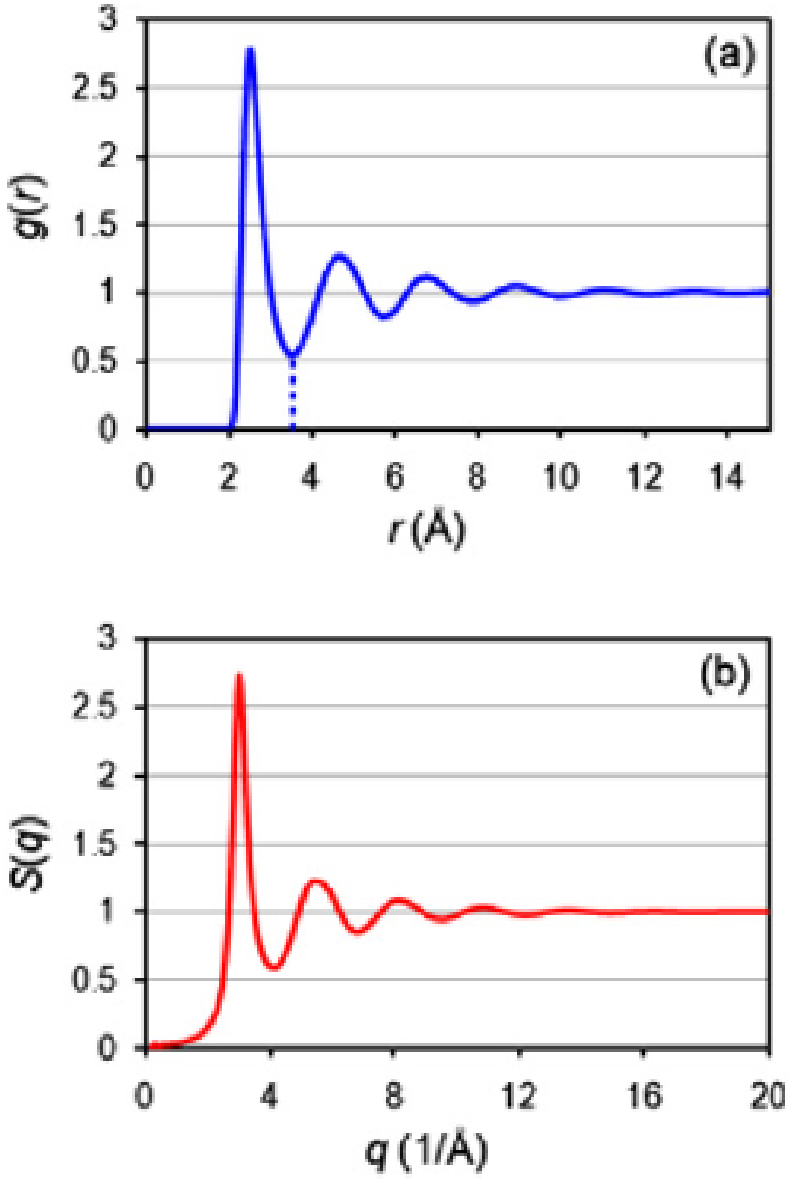

Figure 1.5. (a) PDF and (b) structure factor of liquid Cu at 1500 K, obtained in computer (molecular dynamics) simulation [23].

However, because PDF and structure factor are one dimensional function that describe only average two atom correlation, they do not help much in discussing other properties,

such as the atomic transport. It is necessary to represent and characterize the real three dimensional structure to interpret the deformation and relaxation mechanism of MGs. For this reason, we often resort to phenomenological concepts. There are three structural models most frequently used in describing the atomic transport and deformation in MGs, which are free volume model, dense random packing model and short range order (SRO) model, respectively. Following section is a briefly introduction of these models.

1.3.2 Structural Models

Free volume Model

The term of free volume originated from liquid for the interpretation of its viscosity nearly a century ago. The success made by Cohen and Turnbull [24] in quantifying the concept made this concept widely accepted in the field of metallic glass. Cohen and Turnbull started with recognizing the difference between liquid and gas. In the gaseous state atoms are free to move, but since liquid is a condensed matter, an atom is trapped in the 'cage' of neighboring atoms, and an moving atom gets 'backscattered' most of the time by the neighboring atoms and essentially it cannot move. Only when enough space, larger than v^*, which is the minimum required volume of the void, happens to evolve next to an atom, the atom can move into this space (illustrated in Figure 1.6). The diffusivity can be expressed by the equation:

$$D = D(v^*)\int_{v^*}^{\infty} p(v)dv = D(v^*)\exp\left(-\frac{\gamma v^*}{v_f}\right) \tag{1.4}$$

where v^* is the minimum excess volume needed for an atom or molecule to jump in, v_f is average free volume defined by $v_f = \bar{v} - v_0$ ($\bar{v}$ is the average volume per atom/molecule and v_0 is the actual atomic or molecular volume), γ is a constant of the order of unity, $p(v)$ is the probability distribution of space between atoms, given by

$$p(v) = \frac{\gamma}{v_f} \exp\left(-\frac{\gamma v^*}{v_f}\right) \tag{1.5}$$

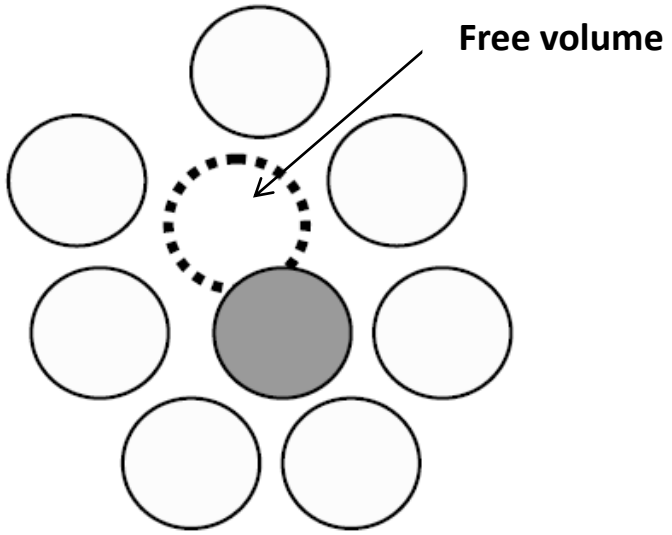

Figure 1.6. Schematic drawing of free volume for an atom to move into.

However, it should be mentioned that the free volume model has some imperfections. First, the model is based on the hard sphere packing, while the nature of metallic bond rejects this assumption. Second, it assumes that the atomic transport in MGs occurs through jumping into a free space next to it, similar to the vacancy-like atomic diffusion

in crystals. However, it is known that larger vacancies are highly unstable in glass. Although some assumptions of the free volume model are questionable, this simple concept is useful and intuitive, and is widely adopted to interpret the deformation and relaxation behaviors of MGs [25].

Dense Random Packing Model

As one of the fundamental models to describe the atomic structure of amorphous alloys, dense random packing of hard spheres (DRPHS) was built by Bernal to represent the structure of the mono-atomic liquid [9]. The essential features of this model include: the liquid is treated as homogeneous system without any order, in which the atoms are considered as hard spheres, and the local structure is determined by the restrictions on space filling and consequently on the inability of two atoms to approach more closely than one diameter. In the dense random packing model, there exist five different types of interstitials space referred to as the 'Bernal holes'. They are named as tetrahedron (a), octahedron (b), dodecadeltahedron (c), trigonal prism (d) and Archimedean anti-prism (e), which are shown in Figure 1.7. Although being very simple, the structure model contains the essential physics of simple liquid, and provides an illuminating structural framework to describe the structures of other simple amorphous systems. However, this dense packing model is too simplistic to describe the actual structure of MGs, as MGs are usually multi-component systems with large mismatch in atomic sizes, which is not accounted by this hard sphere model.

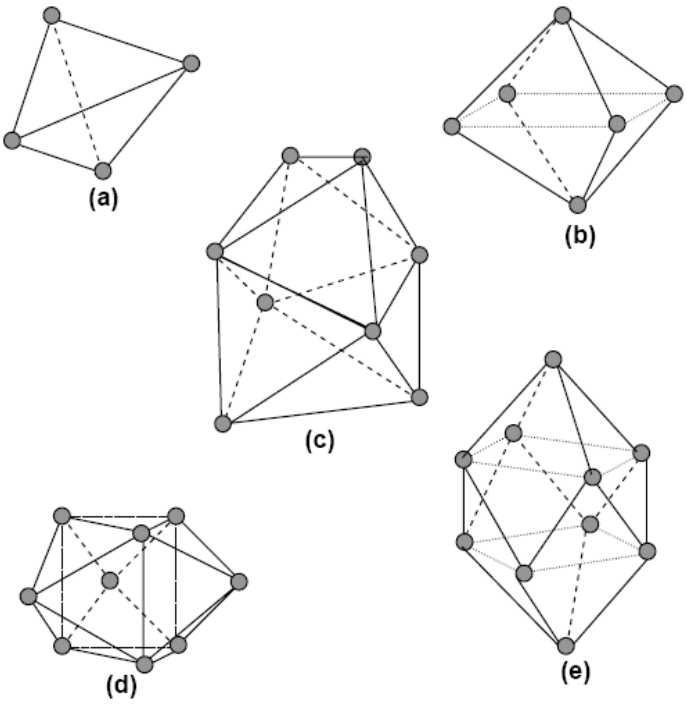

Figure 1.7. Five canonical holes found in a random close packed structure. They are tetrahedron (a), octahedron (b), dodecahedron (c), trigonal-prism (d) and Archimedean anti-prism (e).

Short Range Order Model

Even though MGs are identified as amorphous materials with intrinsic structural randomness at the microscopic scale, closer investigation has revealed that the atomic arrangement of MGs is not completely random and contains a considerable and continuous variation at atomic scale, which can be described by the atomic short range order (SRO). There are two types of SRO known as chemical short range order (CSRO) and topological short range order (TSRO) [26]. Since all MGs stable at ambient temperature are multicomponent alloys, their chemical composition around the atoms of

each alloying component is different from the average. This chemical deviation from the average is called CSRO, and it can be defined as

$$\alpha = 1 - \frac{Z_{AB}}{\langle Z \rangle C_B} = 1 - \frac{Z_{BA}}{\langle Z \rangle C_A} \tag{1.6}$$

where Z_{AB} is the number of β coordination of an α atom, C_A and C_B is the concentration of α and β atom respectively, $\langle Z \rangle$ is the total coordination number. Note that the effect of CSRO is limited within the first nearest neighbor shell in MGs. Compared with CSRO, the topological short range order is more subtle. Consider a single elementary glass in order to get rid of the influence of the CSRO, the topological distortions which characterize the local structure of an elementary glass may be called topological short range order (TSRO). One of the parameters to describing the TSRO is the atomic level stress, defined by [27]:

$$\sigma_i^{\alpha\beta} = \frac{1}{2\Omega_i} \sum_j f_{ij}^{\alpha} r_{ij}^{\beta} \tag{1.7}$$

where α and β denote the Cartesian component, Ω_i is the local volume of the ith atom, and f_{ij} is the two body force between the ith and jth atoms.

Recently, Liu et al. revealed that the global packing of SRO in MGs can be interpreted as the combination of the spherical periodic order and local translational symmetry [28]. They claimed that the electronic influences on the interatomic potential give rise to the spherical periodic order of atomic arrangement at the short- and medium- range distances of disordered metallic system, and the chemical interaction among constituent elements

contributes to the local translational symmetry. It was thought that the SRO is the key structural feature that determines the glass formability and even the physical/mechanical properties of a MG alloy[29].

1.4 Mechanical Properties of Metallic Glasses

The mechanical properties of MGs have proven to be both scientifically unique and of great potential in practical application, thus stimulated considerable researchers to investigate mechanical properties of MGs. However, the underlying deformation mechanism of these materials remains not firmly established compared with that in crystalline alloys. Traditionally, metallic materials are in crystalline state, and their mechanical behaviors are determined essentially by the nature and density of dislocations. Since MGs are non-crystalline in nature absent of translational periodic symmetry, and they do not contain any dislocations, new theoretical model are needed to interpret the deformation behavior of MGs. Specifically, MGs are very strong with the yield strength exceeding 4 GPa in some metal–metalloid systems [30], however, they exhibit very limited plastic strain (often less than about 0.5%) particularly in tension at ambient temperature, and the inhomogeneous deformation occurred through the formation of localized shear bands tends to cause the catastrophic failure of MGs.

1.4.1 Deformation Behavior

Metallic glasses have high strength. However, their Achille's heel is the low ductility at room temperature, that is, the metallic glasses get failure soon after yielding without showing any signs of appreciable amount of plastic deformation. When a MG sample is subjected to tension, the sample deforms elastically until reaching a maximum elastic strain of about 2%, and then localized shear bands emerge and propagate throughout the entire sample, finally the catastrophic failure occurs. Note that shear bands appear approximately on the planes of maximum resolved shear stress [15], and the deformation is mostly concentrated in these shear bands. This localized deformation is referred to as the 'inhomogeneous' deformation. It is the inhomogeneous deformation in the MGs that renders it mechanically unstable at high stress and hinders their application in the engineering field. The detailed deformation behavior of MGs will be discussed in the following sections.

Elastic and anelastic deformation

When applying force with low strain rate on MGs at temperature below the glass transition temperature, MGs deform linearly with the increase of the applied force before yielding. This apparent elastic behavior can be characterized with an elastic modulus, which is a reflection of atomic binding energy density and varies with the cooling history and chemical compositions of MGs [31-34]. The usual assertion made in discussing the elastic behavior of metallic glasses is that these amorphous materials behave isotropically, by virtue of a random disordered atomic structure. However amorphous materials are not necessarily structurally isotropic at the atomic scale, though macroscopically they behave in an isotropic manner. At the atomic level, the disordered structure of a MG is associated

with different local atomic configurations for different atoms. Consequently, not all atoms experience the same displacement when elastically stressed, which causes the shear modulus and young's modulus of the amorphous alloy being 13-36% lower than those of the corresponding crystalline materials with a same composition [35]. The inhomogeneous elastic response of MGs has been revealed by state-of-the-art techniques, which directly reflects their intrinsic structural heterogeneity [26, 27].

Anelasticity is a phenomenon of solid materials in which elastic deformation depends on both stress rate and stress. In MGs, it originates from the inhomogeneous atomic configuration, which gives rise to extra nonaffine atomic displacements of the atoms in the free volume regions, as sketched in Figure 1.8. The free volume regions are such atomic environments in a glass where the local structural topology is unstable. In these regions, the response to shear stress may include not only elastic atomic displacements but also an inelastic reshuffling of the atomic near-neighbors (i.e. an inelastic STZ operation). Even though the fraction of atoms involved in these events may be small, the local strains are large enough that their cumulative effect makes a significant contribution to the macroscopic strain, lowers the modulus of MGs.

The nonlinear displacement of an atom is dependent on the stress rate it undergoes. This has been experimentally observed by applying stress and then relaxing at higher temperature in the early days [36]. In addition, when the stress rate is high enough, hysteresis loop as a reflection of anelasticity will show up [37]. This anelastic property has been attracting more attentions recently, due to the scientific significance for

understanding the detailed glassy structures and potential engineering applications [37, 38].

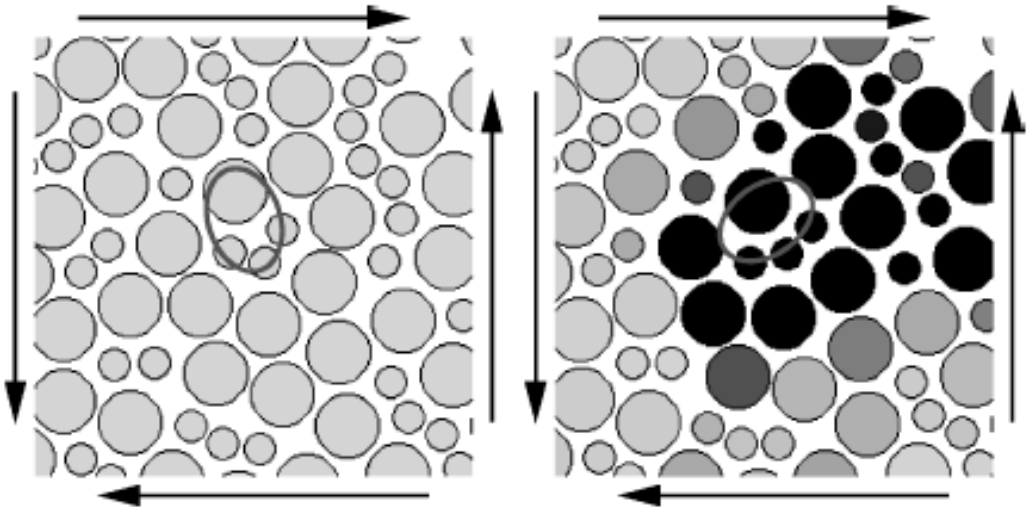

Figure 1.8. Close-up pictures of a nonlinear displacement and after undergoing transformation, ovals are included solely as guides for the eye [39].

Yielding

Without defects such as dislocations that act as weakness in crystalline materials, MGs exhibit a remarkable high strength compared with other materials (see Figure 1.9). After a universal elastic limit of ~2% [40, 41], yielding occurs through the localized shear banding, which is characterized by the deviation from the elastic part and the subsequent serrated load-displacement response, as presented in Figure 1.9. For the yielding criterion of MGs, different from the pressure-independent criterion of polycrystalline solids, the

yielding strength of MGs depends on the pressure they subject, and obeys the Mohr-Coulomb law [42]. The shear strength τ_y of a MG alloy can be taken as:

$$\tau_y = \tau_0 + \alpha\sigma_n \tag{1.8}$$

where τ_0 is the applied shear stress, α is a pressure sensitive parameter and σ_n is the normal stress. Based on the equation, higher yield strength under compression test compared with tension test of MGs can be explained.

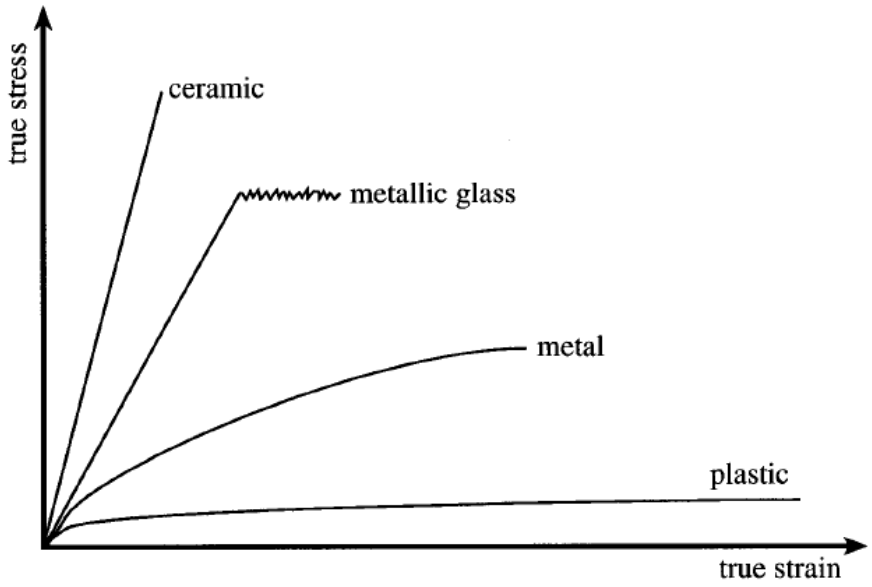

Figure 1.9. A schematic diagram of the uniaxial true stress strain curve of various engineering materials compared with the one typical metallic glass. Metallic glass exhibits elastic-perfectly plastic mechanical behavior during compressive deformation, and serrated flow is observed in the plastic region.

Fractographic studies reveal that the fracture surface of compressive loading has relatively high density of shear bands propagating parallel to the fracture plane. For tensile loading, the fracture plane has predominantly a single shear band propagating across the whole sample as there is no geometrical confinement to stop the shear band. However, both the surfaces show vein patterns indicating shear flow, as shown in Figure 1.10. Stress-strain curves indicate that the plastic strain, in case of compressive loading, is ~1-6%, whereas in case of tensile loading there is almost no macroscopic plastic strain.

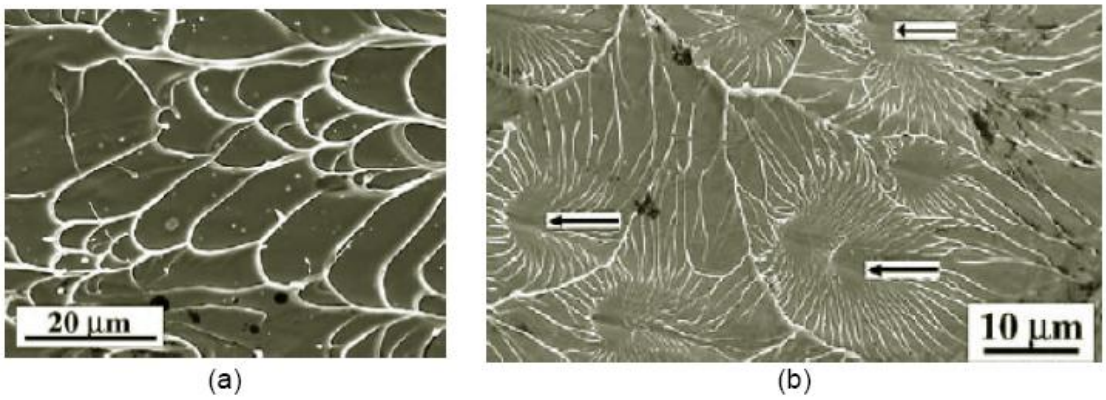

Figure 1.10. SEM micrograph of the fracture surface for the compressive (a) and tensile (b) loadings. The vein pattern suggests shear failure in both cases [15].

Under inhomogeneous deformation metallic glasses form shear bands where the flow is localized. This implies that there must be some structural change in the bands that facilitates faster deformation than the rest of the specimen. Various flow models have been developed and will be described in the following sections.

1.4.2 Deformation Mechanism

Free volume model

Solidified rapidly from the liquid state, MGs have the disordered atomic configuration, among which, the free volume is defined as the excess volume between an atom volume in glassy state and the average atomic volume of ideal dense packed hard sphere structure. The initial content of free volume in MG is fixed at the glass transition temperature when the atomic configuration is frozen as the liquid solidifies. Spaepen described the deformation process of MGs as a competition between the stress-driven creation and diffusional annihilation of free volume [18], and flow occurs in the form of a series of atomic jumps, that is, an atom moves by jumping into an adjacent space sufficient to accommodate it. The activation energy of atomic jump ΔG_m is supplied by force or temperature. In the absence of an applied force, the number of forward and backward jumps caused by the thermal fluctuations is equal at room temperature. When a shear stress is applied to the system, the free energy barrier in the direction of the applied stress is reduced so that the number of forward jumps exceeds the number of backward, enable the macroscopic flow (the basic concept is illustrated in Figure 1.11). Free volume is created when an atom with hard sphere volume v^* is squeezed into a neighboring hole with a smaller volume v.

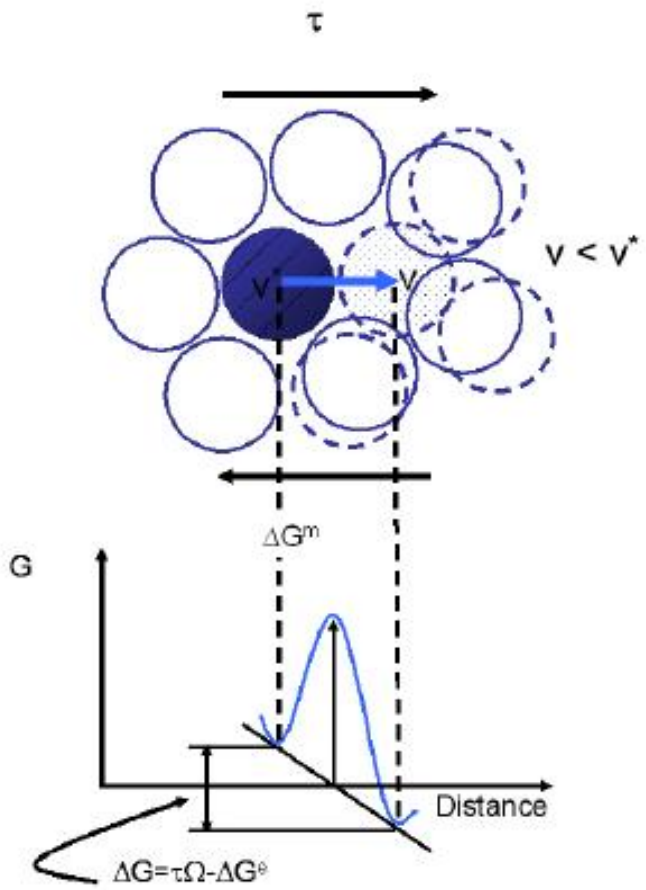

Figure 1.11. Illustration of the creation of free volume, by squeezing an atom of volume v^* into a neighboring hole of smaller volume v [18].

As free volume is created due to the applied shear stress, at low stresses and high temperature, a series of diffusional jumps is sufficient to relax the structural changes, and the uniform deformation occurs; at high stresses and low temperature, however, diffusion cannot compensate for the stress driven creation of free volume, free volume accumulates in shear bands and inhomogeneous flow occurs. Spaepen quantified this flow process, and the constitutive equation is given by:

$$\dot{\gamma} = 2\nu\Delta f \exp\left(-\frac{\gamma v^*}{v_f}\right)\exp\left(-\frac{\Delta G^m}{kT}\right)\sinh\left(\frac{\tau\Omega}{2kT}\right) \tag{1.9}$$

where γ is the shear strain, υ is the frequency of atomic vibration (~Debye frequency), γ is a numerical factor between 0.5 and 1 that takes care of the overlap of free volumes, v^* is the minimum excess volume needed for an atom or molecule to jump in, v_f is average free volume defined by $v_f = \bar{v} - v_0$ ($\bar{v}$ is the average volume per atom/molecule and v_0 is the actual atomic or molecular volume), T is the absolute temperature, ΔG_m is the activation energy for an atomic jump, k is the Boltzmann constant, Ω is the atomic volume, Δf is the fraction of volume undergoing flow (=1 for homogeneous flow and <1 for inhomogeneous flow).

Shear transformation zone model

Extended from the free volume model, Argon proposed the concept of shear transformation zone (STZ), which describe the glass deformation as a collective operation of many small atomic scale shear events, that is, a group of atoms cooperatively shuffle in a shear mode under the action of external stress or temperature [19]. Generally, thermally activated STZs initiate around free volume sites under an applied shear stress because high elastic strain at free volume sites energetically promotes STZ formation. Argon suggested that the shape of a STZ is a thin disk with diameters of approximately eight atoms, and the shear transformation process closely resembles the nucleation of a dislocation loop. Analogous to the single-atom squeezing in free volume model, the local shear transformations around the free volume sites can lead to the pushing apart of

surrounding atoms along the activation paths, resulting in an activation dilatation and thereby a local strain softening during the room temperature deformation. The process is sketched in Figure 1.12. For a MG subjected to a shear stress τ, the strain rate resulting from the superposition of many individual STZ operations can be expressed as

$$\dot{\gamma} = \alpha_0 \nu_0 \gamma_0 \cdot \exp\left(-\frac{\Delta F}{kT}\right) \sinh\left(\frac{\tau \gamma_0 \Omega_0}{kT}\right) \tag{1.10}$$

in which α_0 is a constant incorporating the fraction of material that is capable of undergoing shear transformation and ν_0 is the natural frequency of the STZs; ΔF is the Helmholtz free energy required to sustain a local shear strain γ_0 for a STZ of volume Ω_0, and it can be calculated based on the elastic properties of the glass, which is expressed as following equation:

$$\Delta F = \left[\frac{7-5\nu}{30(1-\nu)} + \frac{2(1+\nu)}{9(1-\nu)}\beta^2 + \frac{\tau_0}{2\gamma_0 \mu(T)}\right] \cdot \mu(T)\gamma_0^2 \Omega_0 \tag{1.11}$$

where $\mu(T)$ and ν is shear modulus and Poisson's ration of the glass, respectively; β is a numerical constant that describes the volumetric dilation of the STZ relative to its shear distortion, and is approximately equal to unity for MG; τ_0 is the applied shear stress. It is assumed shear elastic strain energy is short lived and is dissipated soon after the shear transformation.

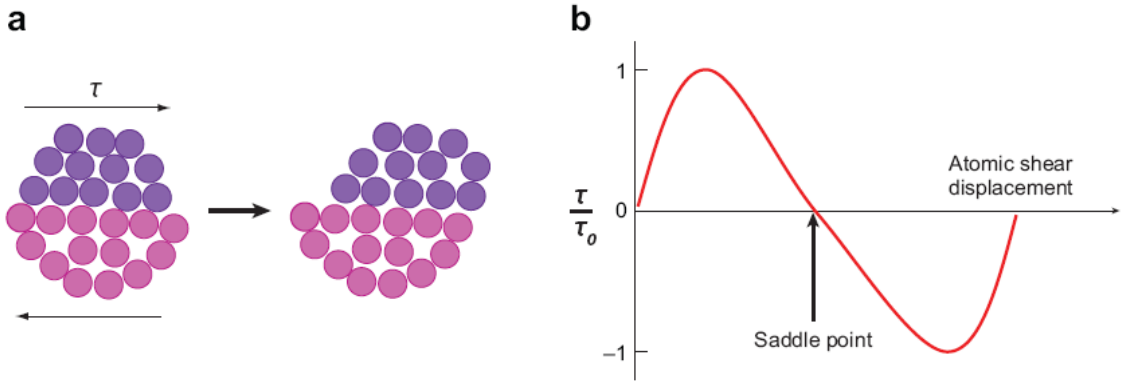

Figure 1.12. (a) A two-dimensional schematic of a shear transformation zone in a MG. A shear displacement occurs to accommodate an applied shear stress τ, with the darker upper atoms moving with respect to the lower atoms. (b) The applied shear stress τ necessary to maintain a given atomic shear displacement, normalized by the maximum value of τ_0 [20].

At temperature well below T_g, when the applied stress is small, only a few and isolated STZs with the smallest energy barriers can be activated, while much of the background structure acts substantially as an elastic medium. Under higher stress, larger fraction of STZs with higher threshold energy barriers can be transformed into sheared states until at a certain well defined stress the activated STZs give continuously sheared regions throughout the volume, the elastic background is invalid, and the plastic deformation occurs.

Cooperative shear model

Based on the basic idea of STZ cooperative movements, the concept of cooperative shear model (CSM) was proposed by Johnson et al. to depict the plastic yielding of metallic

glass. In CSM, a periodic potential energy landscape was introduced to describe the atomic configuration energy state in MGs [43]. The energetic landscape of the system comprises a population of inherent states (basins) associated with local minima, which are the relative stable configurational states of the glass. These basins are separated by saddle points that constitute the barriers for configurational hopping between local minimum configurations. By assuming the average potential energy versus shear strain in the vicinity of a basin to be a sinusoid, one can relate the average potential energy density to the canonical shear strain coordinate via:

$$\phi / \phi_o = \sin^2\left(\pi\gamma / 4\gamma_c\right) \tag{1.12}$$

where ϕ is the barrier energy density, $4\gamma_c$ is the average configurational spacing, and γ_c is the shear strain limit of the materials, which was found to be universal for known metallic glass systems [44]. A plot of this function in the vicinity of two inherent states is presented in Figure 1.12. The energy barrier for shear flow can be expressed as

$$W = (8/\pi^2)\gamma_c^2 G\Omega \tag{1.13}$$

in which G is shear modulus, Ω is STZ volume. This equation predicts that barrier height of shear flow for a given glass configuration is proportional to G, and yielding occurs when the applied stress causes a critical density of 'minimum' barrier STZs become unstable, i.e. cooperative shear transformation become activated.

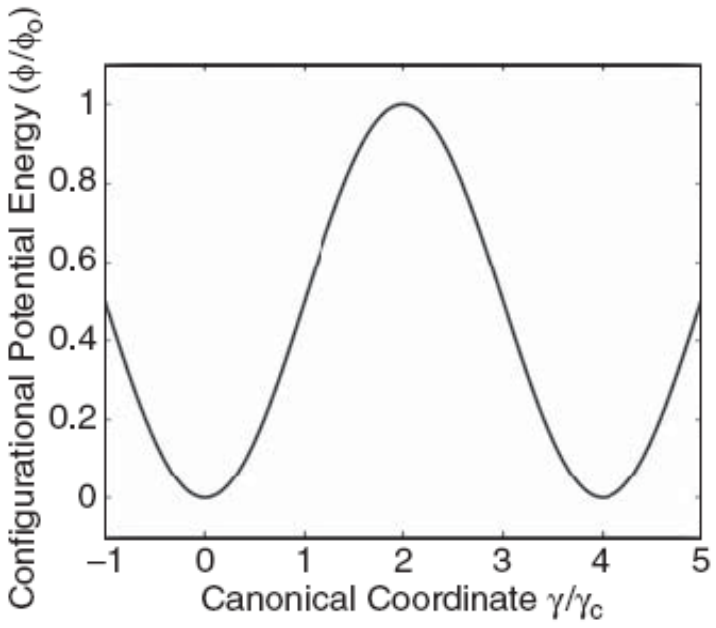

Figure 1.13. A plot of the potential energy density function in the vicinity of two inherent states.

1.5 Cooling Rate Effects

1.5.1 Effect on Structure of Metallic Glasses

In the literature [45], positron annihilation lifetime spectroscopy was used to probe the free volume quenched in the typical Zr-based bulk metallic glasses prepared with different cooling rate (variation more than three orders of magnitude), it was found out that the average positron annihilation lifetime increased from around 177 to 179 ps with an increase of cooling rate, indicating a higher amount of free volume quenched in the metallic glass with higher cooling rates.

In addition, Gupta and Jayaraj studied the effect of the cooling rate from liquid and the subsequent heat treatment on the structure and stability of Co-based amorphous alloys using Mössbauer spectroscopy and differential scanning calorimetry [46]. They detected topological short range order changes with quenching rate variation, and found a faster quenching rate resulted in an increased stability of the amorphous phase. The increased stability could be attributed to a decrease in the number of quenched-in nuclei or crystallites in the amorphous alloy with higher cooling rate. However, Kane et al. [47] found that there is no significant difference in the degree of topological disorder in the two Fe-based amorphous ribbons with different thickness (hence different cooling rate) using X-ray diffraction and Mössbauer spectroscopy. They claimed that the variation in quenching rates influences mainly the quenched-in free volume and the internal stresses. These different conclusions might arise from the difference of experimental conditions, such as the melting method and melting temperature.

To make up for the limitation of the experimental methods, molecular dynamics simulations were carried out to provide intuitive insight into the microstructure and properties at atomic level. Wang et al. reproduced the process of preparing metallic glasses in laboratory including the melting, equilibrating and quenching procedure with molecular dynamics simulations [48]. At the melting point, significant structural change occurs via the rearrangement of short-range order. The amorphous structure in the liquid state was frozen during the quenching at rapid cooling rate. Different cooling rates have no apparent effects on the short-range order of final amorphous state as seen from their MD simulations. However, lower cooling rates lead to denser packing and better

equilibrated final state as well as lower volume and potential energy, while higher cooling rates may give rise to more free volume frozen in the amorphous structures.

1.5.2 Effect on Properties of Metallic Glasses

Thermodynamic properties

Louzguine-Luzgin et al. have studied the influence of the cooling rate on the formation of glassy phase and thermal stability of Cu-based glassy alloys [49]. No significant difference is found in the glass-transition temperature of melt-spun ribbons and bulk glassy rods for the alloys. This agrees well with previous finding that the dependence of T_g on the cooling rate is weak [50].

Structural relaxation behavior of a rapidly quenched and a slowly quenched $Pd_{40}Cu_{30}Ni_{10}P_{20}$ metallic glass was investigated and compared by Ragahavan et al. [51]. Differential scanning calorimetry was employed to monitor the relaxation enthalpies at the glass transition temperature, and the Kolrausch-Williams-Watts stretched exponential function was used to describe its variation with the annealing time. It was found that the rate of enthalpy recovery was higher in the ribbon sample, implying that the bulk is more resistant to relaxation at low temperatures of annealing. This was attributed to the possibility of cooling rate affecting the locations where the glasses get trapped within the potential energy landscape. The rapidly quenched process traps a larger amount of free volume, resulting in higher fragility, and in turn relaxes at the slightest thermal excitation.

The slowly quenched BMG, on the other hand, entraps lower free volume and has more short range ordering, hence requires a large amount of perturbation to access lower energy basins.

Xu et al. investigated the influence of the quenching rate on the crystallization behaviors of melt-spun $Mg_{63}Ni_{22}Pr_{15}$ metallic glass [52]. He found that the crystallization behaviors of the $Mg_{63}Ni_{22}Pr_{15}$ alloy strongly depend on the quenching rates, and argued that quenched-in nuclei play more important role in the crystallization process of the MG with lower quenching rate. The existence of the quenched-in nuclei reduces the energy barrier for nucleation, and makes the crystallization easier, thus causing the decrease of the transition temperatures. Besides, the effect of cooling rate on the crystallization of metallic glass $Zr_{70}Cu_{20}Ni_{10}$ has been investigated by Wang et al. [53]. In their study, it was found out that the cooling rate does not change the crystallization kinetics of metallic glass, but changes the weight of three-dimensional nucleation and growth in the whole crystallization process. Some other researchers claimed that decreasing the cooling rate would favor the formation of a greater degree of MRO and shorten the diffusion path, leading to lower activation energies for the bulk sample compared with ribbon sample [54].

Mechanical Properties

Contrary to the cooling-rate induced hardening observed in crystalline metals, Liu et al. found a 500 μm thick soft layer with lower hardness and elastic modulus near the surface of a ZrCu-based BMG rod (diameter 2 mm) [55]. They concluded that this was caused by

freezing-in excess defects induced by a faster cooling rate near the surface compared to the interior. Higher defect concentrations enhance the probability of atom jumping, which in turn is expected to increase the flux of atoms and decrease the flow stress (hardness). Chen et al. also found that the cooling rate employed in $Pd_{81}Si_{19}$ glassy alloy sample preparation significantly influenced the hardness of the as-prepared glassy alloys [56]. Decreasing the cooling rate would increase the hardness of the as-prepared glassy samples. The difference in microstructures of glassy alloys, which was revealed by the XRD spectrum, was believed to lead to the difference of the hardness of the glassy samples. Moreover, they found that decreasing cooling rate would promote the formation of denser atomic configuration and local ordering clusters (MRO) due to more structural relaxation.

However, by comparing mechanical properties and microstructural changes of suction cast Ti-based BMGs rods with diameter 2 and 3 mm, Kim et al. [57] found that the strength and plasticity of the 2 mm sample with higher cooling rate is larger than that of the 3mm sample, in which the yielding strength data is contrary to the foregoing hardness data. Through TEM observation, they noticed that the local chemistry, structure and length scale of heterogeneous regions in the BMGs changes with the dimensions of the rods prepared at different cooling rates. They argued that these variations in microstructural heterogeneity cause the transition of the stress state affecting the overall mechanical behavior of the BMG rods. Besides, Park et al. also found that the cooling rate can affect the structural heterogeneity and the deformability of Mg-based BMGs [58, 59]. They reported that the compressive fracture strain increased from 2.97% for MG

sample with diameter 1 mm up to 3.74% for sample with diameter 2 mm, then decreased sharply when further increasing the diameter for the sample. They claimed that the degree of local heterogeneity in the amorphous matrix can be varied depending on the cooling rate during solidification, which results in the changing the plastic strain. However, in their analysis, size effect was neglected, which also might contribute to the variation of the yield strength and plasticity.

Shen et al. [60] found that the plastic deformation capacity of a Ti-based BMG is strongly dependent on cooling rates of the alloy. It was found that the ductility of the BMG increases with increasing of the cooling rate in solidification, and they attributed this to the large concentration of free volume trapped in the amorphous alloy with a high cooling rate. In addition, it was shown that the strength of the metallic glass slightly decrease with the increase of the cooling rate. Zhang et al. [61] also found that the compressive plastic strain increases with the increasing cooling rate for another Zr-based BMG, and thought that the free volume content during the rapid solidification plays an important role in the plastic deformation process of the BMGs. It is worth mentioning that during BMG preparation voids are likely formed in the bulk samples caused by the high cooling rate employed, these voids could reduce the yielding strength, and bring negative effects to the plasticity of BMGs, but this factor has not been addressed in those works.

Apart from the traditional compression test, nanoindentation method was also employed to investigate the cooling rate effect on the mechanical properties of metallic glasses, which explore the local response of the MGs and get rid of the voids effect in

macroscopic compression test. Using this technique, Huang et al. investigated the cooling rate effect on a Ti-based metallic glass [62, 63]. It was found that the ribbon sample exhibits lower hardness, higher pile-up ratio and lower incipient plasticity than bulk samples with smaller cooling rate. They declared that more free volumes quenched in the ribbon sample serves as the preferential shear band nucleation sites, resulting in a lower resistance to deformation. In addition, the as-cast bulk and as-spun ribbon $Cu_{60}Zr_{30}Ti_{10}$ metallic glasses were investigated utilizing nanoindentation by Jiang et al. [64]. They also found that the bulk alloy has a higher hardness and elastic modulus than the ribbon alloy. And they concluded that the difference in hardness was related to the different amount of free volume in the amorphous matrix. However, similar serrated plastic flow and pile-ups were noted for the bulk and ribbon alloys during the nanoindentation test.

After reviewing previous researches, we find that the conclusions about cooling rate effect on yielding strength of MGs are controversial, and the mechanism is not clear at present. In addition, researches about cooling rate effects on Young's modulus of MGs are limited.

Physical properties

Hu et al. [65] reported an increase of density from 9.270 to 9.285 g/cm^3 with decreasing cooling rate from 500 to 1.98 K/s for the $Pd_{40}Ni_{10}Cu_{30}P_{20}$ BMG during solidification, and considered this to be the result of more free volume quenched in the metallic glass with higher cooling rate. In addition, a low cooling rate can induce precipitation of

nanocrystals, quasicrystals [66] , and contributes to the magnetic properties variation [67-70].

In addition, tensile creep tests of bulk and ribbon Zr-based MG samples have been performed [71]. It was found that a change of the quenching rate by about three orders of magnitude exerted little influence on the shear viscosity of the MG below the glass transition temperature. This fact was explained within the framework of the directional structural relaxation model, which treats plastic flow below glass transition temperature as a serious of irreversible structural relaxation with distributed activation energies. The variation of quenching rate by three to four orders of magnitude has no influence on the low energy part of the activation energy spectrum (AES), this result in unchanged shear viscosity of the bulk and ribbon MG samples.

1.6 Research Objectives and Scope

As a new class of materials, MGs possess impressive mechanical properties [1, 2, 72] , such as high yielding strength, large elastic limit and high fracture toughness, due to their random atomic arrangement and lack of microstructural defects. Extensive efforts have been dedicated to revealing the underlying deformation mechanism of MGs [13, 20, 43], however limited by the spatial and temporal resolution of the current characterization equipment, the mechanism of deformation is far from fully understood. Besides, the BMG community is confused by scattered mechanical results of metallic glasses obtained from macroscopic mechanical tests due to a number of factors introduced during the MGs

preparation and testing [55, 73-75]. Moreover, low resolution of the macroscopic testing equipment obscures the real mechanical response of MGs. By contrast, micromechanical tests, such as nanoindentation and microcompression, exclude the effects of manufacturing defects with the additional advantage of ultrahigh sensitivity. These make us approach the delicate deformation realm of MGs when entering the micro-scale. Therefore, this research will investigate the micromechanical behavior of MGs, and attempt to disclose the delicate deformation mechanism of MGs.

After this Introduction chapter and the following chapter on Research Methodologies, the cooling rate effect was first studied to explore the thermal history effect on the micromechanical response of MGs. It is known that the cooling rate can affect the atomic structure and thus may possibly affect the mechanical properties of metallic glasses. However, its effect on structural and mechanical properties of MGs is not well understood. In Chapters 3 and 4, the cooling rate effect on micromechanical behaviors of a $Zr_{55}Pd_{10}Cu_{20}Ni_5Al_{10}$ (atomic %) MG was investigated using nanoindentation and microcompression methods. With respect to quasi-static response, classical Oliver-Pharr method was employed. Young's modulus and hardness of the MGs with different cooling rate were extracted and analyzed. In addition, microcompression and computer simulation were used to examine disturbance coming from the sample thickness effect and to better reflect the cooling rate effect on the static mechanical properties of MGs. For the dynamic response, cyclic dynamic testing method was used [37], and effective modulus and viscosity were obtained. To interpret these dynamic results, an anelasticity model of MGs was proposed. Through the analysis of results obtained, structure

information of the elastic shell and free volume zones of the metallic glasses were uncovered.

Speed of shear bands (SBs) was investigated utilizing multiple ‘loading-holding-unloading’ cyclic microcompression tests in Chapter 5. SBs generally exhibit a ‘size effect’ when propagating in BMGs of different sizes [76-80]. In large samples, SBs tend to propagate catastrophically, causing brittle-like fracture; in contrast, they display the character of ‘stick-slip’ propagation in small samples, leading to serrated plastic flows [81]. It is already known that the magnitude of a shear offset is size dependent in BMGs, and very likely such size dependence will be reflected in the SB speed. However, in the prior work, the measurements of a SB speed were performed for a particular size of shear offset [82-84], and there still lacks a systematic investigation of the size dependence of SB speed in BMGs. In Chapter 5, the size affected shear band speed will be addressed, and energy balance principle is introduced to interpret the shear band speed for the nano-sized shear offsets in microcompression.

In the final appendix, micro-mechanical characterization of casting induced inhomogeneity in a high entropy alloy was performed. As another multi-component alloy, high entropy alloy also possess structural and mechanical inhomogeneity, akin to metallic glass, but in the micrometer scale. This micro-scale inhomogeneity provides additional chance for micromechanical investigation.

CHAPTER 2 Research Methodologies

The research of this study was carried out from four aspects: sample preparation, structure inspection, thermal factor measurement, mechanical properties determination. In the process, various methodologies were involved, and will be briefly introduced in this chapter.

2.1 Sample Preparation

The basic requirements to obtain metallic glass are high purity of the raw materials to reduce the number of heterogeneous nucleation sites and sufficient cooling rate to bypass the crystallization. So in the sample preparation process, constituent elements with purity better than 99.9% were melted in Ti-gettered high purified argon atmosphere by arc-melting to prepare the master alloy ingots. It has been noted that the solidification rate *R* in the process is inversely proportional to the square of the thickness of the solidified molten layer [85]. For a layer of thickness *t* that has solidified at a heat transfer coefficient of ∞, the cooling rate can be expressed as

$$\mathrm{R} = \frac{A}{t^2} \tag{2.1}$$

where *t* is the characteristic dimension in cooling process, such as thickness of ribbon and diameter of the rod; *A* is a constant, which related to materials properties and independent to *t*, here *A* can be taken as 10. To obtain sufficient difference in cooling rate, and facilitate the subsequent research, through the dimension selection, bulk metallic glasses (BMGs) and ribbon metallic glasses (RMGs) were prepared utilizing the following methods.

2.1.1 Suction Casting

Suction casting method is most popular method of synthesizing BMGs. The suction casting system consists of two chambers: an upper chamber in which the alloy is melted and a lower chamber in which the casting is done in a copper mold (as shown in Figure 2.1). Two chambers are connected through an orifice. The principle involved in suction casting is to suck the molten alloy into a mold cavity by using a pressure difference between the melting chamber and the casting chamber. As shown in Figure 2.1, the base of the mold is connected to a vacuum source though a valve, when released, causes a pressure difference, which pushes the melt into the mold cavity.

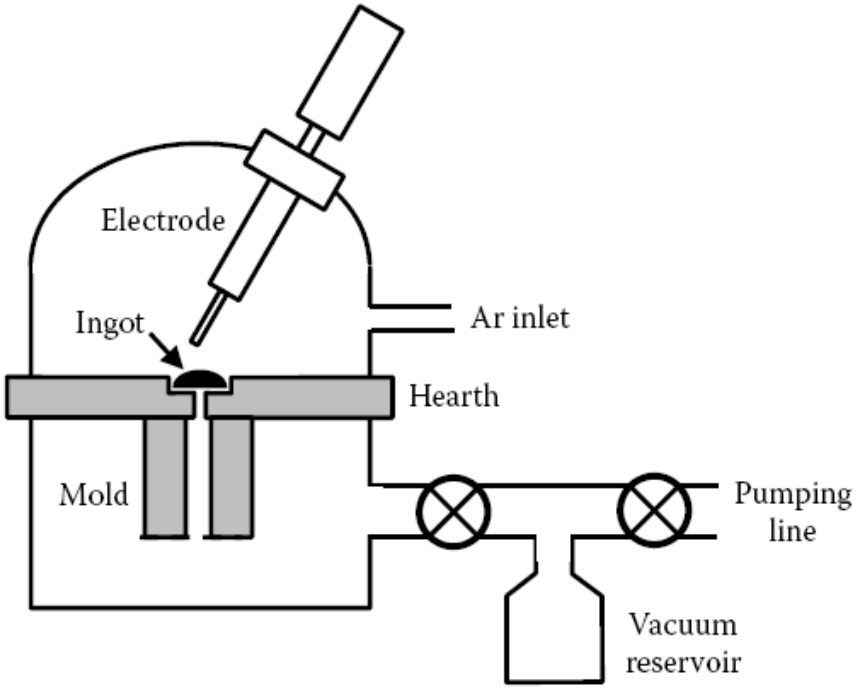

Figure 2.1. Schematic diagram of the arc melting/suction casting apparatus[86].

2.1.2 Melt Spinning

Melt spinning technique is the most commonly used method to produce long and continuous rapidly solidified RMGs. The technique derives its name from the fact that it involves the extrusion of molten metal to produce fine fibers in a way that akin to that used for the manufacturing of synthetic textile fibers. In the melt spinning process, the molten metal is ejected through an orifice and the melt stream is allowed to solidify either in flight or against a chill, which is referred to as free-flight melt spinning (FFMS) and chill-block melt spinning (CBMS), respectively. CBMS process is most commonly used by researchers of MGs field. Figure 2.2 presents a schematic illustration of the melt spinning process.

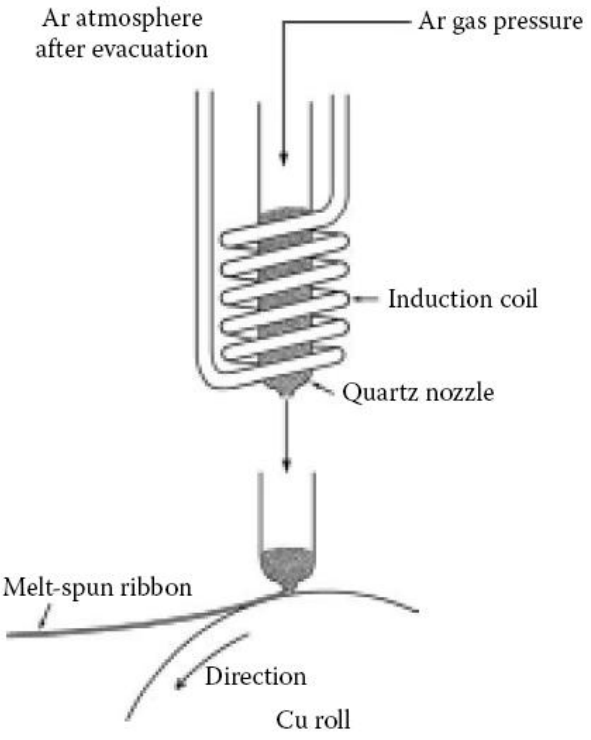

Figure 2.2. Schematic illustration of the melt spinning process.

2.2 Structure Inspection

X-ray diffraction (XRD) is a common and non-destructive method for characterization of crystal structure and for determination of atom location of various materials in bulk solids, powders, or thin films form. The fundamental principle of XRD is described below. The X-ray ejected from the X-ray source interacts with the atoms of the testing materials and makes their atoms polarized, that is, an atom's negatively charged electrons and positively charged nucleus experience forces in opposite directions. This charge

distribution is equivalent to the electronic dipoles, and the polarization oscillates in the alternating electric field arising from the exerting electromagnetic wave. The oscillating dipoles in turn radiate electromagnetic waves of same frequency, and the waves propagate in all direction. The radiation emitted from one atom interacts destructively with radiation from other atoms except in certain directions. In these directions, the scattered radiation is reinforced rather than annihilated. The process follows the Bragg's Law:

$$2d \sin\theta = n\lambda \tag{2.2}$$

where n is the order of the intensity maximum, λ is the wavelength of X-ray, d is the interplanar spacing, and θ is the angle of incident of X-ray beam.

The occurrence of an amorphous phase is generally inferred by the observing of one or two broad and diffuse peaks in the XRD patterns. The XRD technique only can reflect the statistic distribution of the atomic arrangement in the metallic glass systems.

2.3 Thermal Factor Measurement

Differential scanning calorimetry (DSC) is a thermal analytical technique in which the difference between the amount of heat required to increase the temperature of the testing sample and the reference sample are measured as a function of temperature. Both the testing sample and reference sample are maintained at nearly the same temperature throughout the experiment. Generally, the temperature program for a DSC analysis is

designed to increase linearly as a function of time. The reference sample should have a well-defined heat capacity over the range of temperatures to be scanned. The basic principle underlying this technique is that, when the testing sample undergoes a physical transformation such as phase transitions, more or less heat will be needed to flow to the sample than the reference sample for maintaining both of them at the same temperature. The amount of heat flow to the testing sample depends on nature the process is exothermic or endothermic. For instance, when a solid sample melts to a liquid, it will require more heat flowing to the testing sample to increase its temperature compared with the reference sample. This is due to the endothermic nature of the melting process. Likewise, as the testing sample undergoes exothermic processes (such as crystallization) less heat is required to raise the sample temperature. By measuring the difference in heat flow between the testing sample and reference sample, DSC can detect the temperature range corresponding to the physical transformation, and measure the amount of relative heat absorbed or released during such transition.

A typical DSC plot of a BMG sample is shown in Figure 2.3. In this plot, one can notice three important transformations: glass transition, crystallization and melting. Correspondingly T_g is the glass transition temperature, T_x is the crystallization temperature, and T_m is the melting temperature. The BMG sample continues to be in the glassy state until T_g, the presence of which is identified by a change in the slope of the base line. An increase in the heat capacity is noted at T_g. Even though crystallization does not occur below T_g, the as-quenched glass undergoes structural relaxation. Above T_g, the BMG sample enters to the supercooled liquid region. Further heating to crystallization

temperature, crystallization begins to occur in the BMG sample, corresponding several exothermic peaks. At melting temperature, the BMG sample begins to melt.

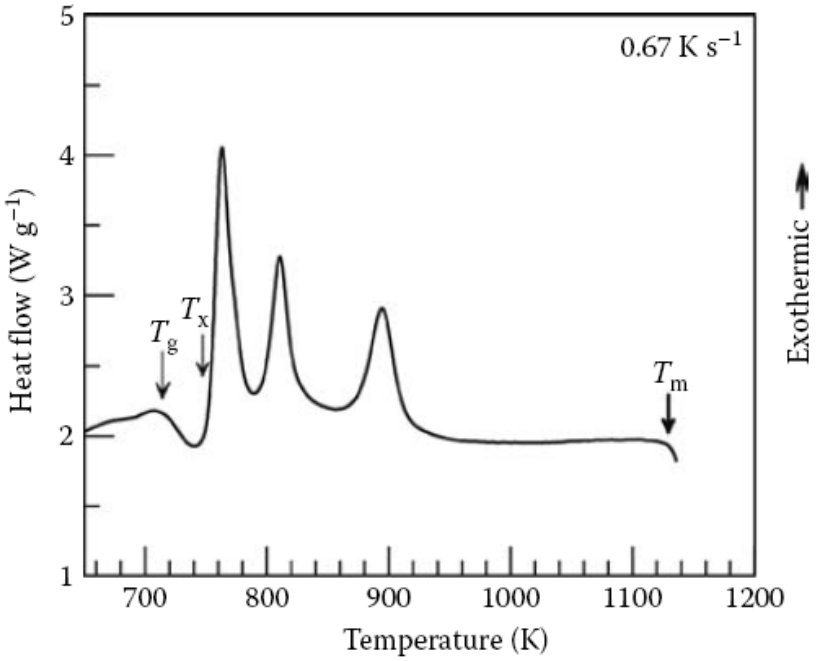

Figure 2.3. Typical DSC curve obtained on heating a BMG alloy from room temperature to high temperatures at a constant heating rate of 40 K min^{-1}.

2.4 Mechanical Performance Determination

2.4.1 Nanoindentation

Indention testing is a simple method that consists essentially of touching the materials of interest whose mechanical properties such as elastic modulus and hardness are unknown

with another material whose properties are given. Nanoindentation is a variety of indentation hardness tests applied to small volumes (nano- to micro- scale), a schematic diagram of the nanoindentation instrument is presented in Figure 2.4.

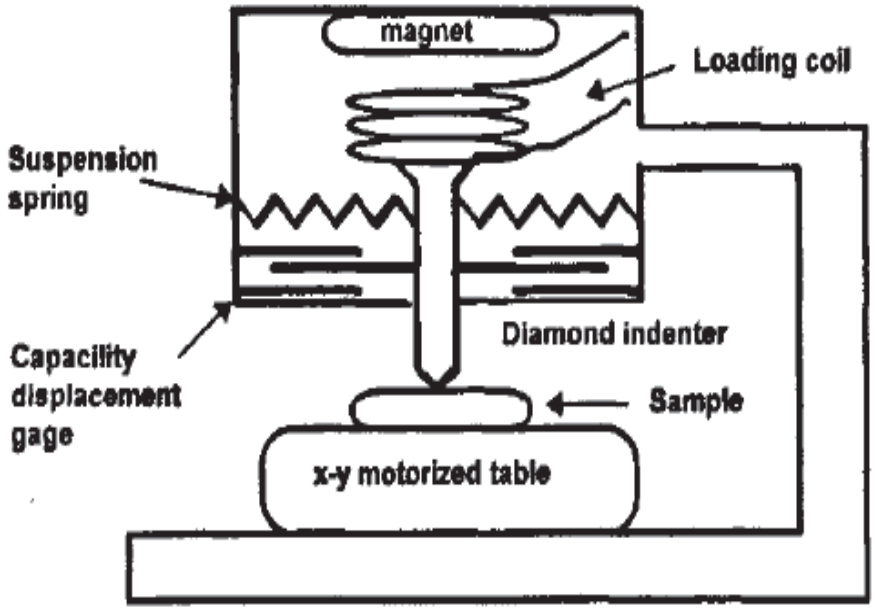

Figure 2.4. Systematic structure map of the nanoindentation.

In this study, classical Oliver & Pharr method was adopted [87]. The method has been widely used in the characterization of mechanical behavior of materials at small scales. Its attractiveness stems largely from the fact that mechanical properties can be determined directly from indentation load and displacement measurements without the need to image the hardness impression. In addition, high-resolution of the nanoindentation equipment facilitates the measurement of mechanical properties at the

micrometer and nanometer scales. Typical load depth curve and schematic illustration of the unloading process are depicted in Figure 2.5.

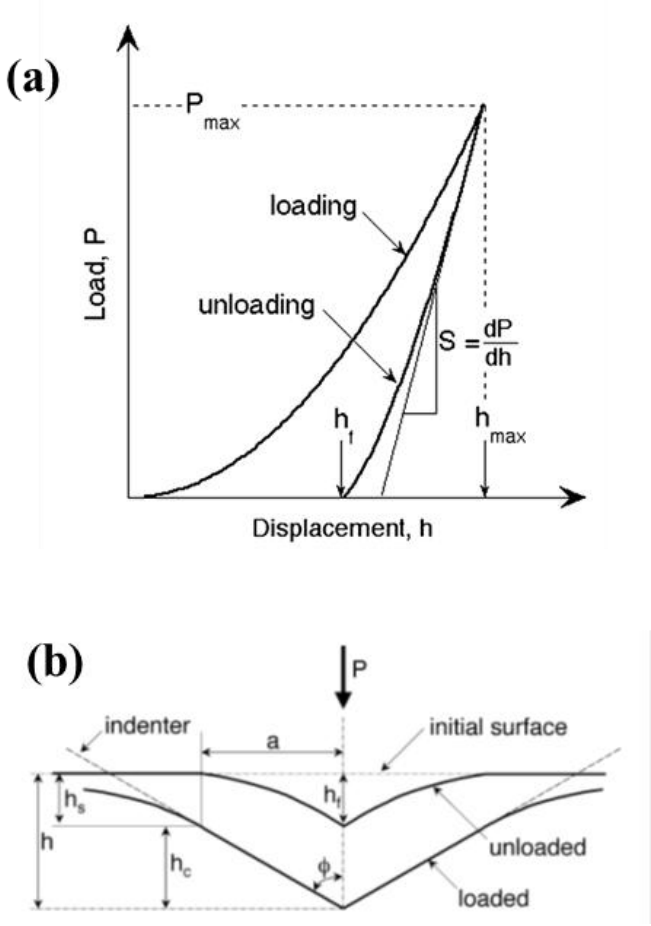

Figure 2.5. (a) Schematic illustration of indentation load–displacement data showing important measured parameters; (b) Schematic illustration of the unloading process showing parameters characterizing the contact geometry.

The exact procedure used to measure *H* and *E* is based on the unloading processes shown schematically in Figure 2.5(a), in which it is assumed that the behavior of the Berkovich

indenter can be modeled by a conical indenter with a half-included angle $\Phi = 70.3°$, that gives the same depth to area relationship. The basic assumption is that the contact periphery sinks in a manner that can be described by models for indentation of a flat elastic half space by rigid punches of simple geometry. This assumption limits the applicability of the method because it does not account for the pile-up of material at the contact periphery that occurs in some elastic–plastic materials. However, assuming that pile-up is negligible (in many cases, this assumption is suitable), the elastic models show that the amount of sink-in, h_s, is given by:

$$h_s = \varepsilon \frac{P_{\max}}{S} \tag{2.3}$$

where ε is a constant that depends on the geometry of the indenter. For Berkovich indenter $\varepsilon = 0.75$.

Using Equation (2.3) to approximate the vertical displacement of the contact periphery, it follows from the geometry of Figure 2.5(b) that he depth along which contact is made between the indenter and the specimen, $h_c = h_{max} - h_s$, that is:

$$h_c = h_{\max} - \varepsilon \cdot \frac{P_{\max}}{S} \tag{2.4}$$

Letting *F(d)* be an "area function" that describes the projected area of the indenter at a distance *d* back from its tip, then the contact area *A* is

$$A = F(h_c) \tag{2.5}$$

Using the contact area determined above, the hardness can be estimated using equation as:

$$H = \frac{P_{\max}}{A} \tag{2.6}$$

While, the measurement of the elastic modulus follows from its relationship to contact area and the measured unloading stiffness through the relation:

$$S = \beta \frac{2}{\sqrt{\pi}} E_{eff} \sqrt{A} \tag{2.7}$$

where E_{eff} is the effective elastic modulus defined by

$$\frac{1}{E_{eff}} = \frac{1-\nu_s^2}{E_s} + \frac{1-\nu_i^2}{E_i} \tag{2.8}$$

The effective elastic modulus takes into account the fact that elastic displacements occur in both the specimen, with Young's modulus E_s and Poisson's ratio ν_s, and the indenter, with elastic modulus E_i and Poisson's ratioν_i.

Low-load system TriboIndenter® and high-load system TriboScratch® nanoindentation instruments developed by Hysitron Inc. were utilized to explore the micromechanical behaviors of MGs. In the nanoindentation systems, force and displacement signals are detected by electrical capacitive sensors, which provide very high resolution. Table 2.1 lists the specifications of the transducers in low-load and high-load systems, respectively.

Table 2.1. Specifications of the transducer in nanoindentation system

	Low-Load System	High-Load System
Maximum force	10 mN	7 N
Load resolution	1 nN	100 nN
Load Noise floor	100 nN	50 μN
Maximum displacement	5 μm	80 μm
Displacement resolution	0.04 nm	0.1 nm
Displacement noise floor	0.2 nm	1 nm
Thermal drift	Less than 0.05 nm/sec	Less than 1 nm/sec
Data acquisition rate	More than 10^4 Points/sec	60 Points/sec

2.4.2 Microcompression

Microcompression test mimics the conventional macroscopic compression testing, with some modifications to facilitate both the fabrication of the microscale samples and their subsequent manipulation into the testing system [88, 89]. The most significant difference is that the microcompression samples are not freestanding; rather, they remain integrally attached to the bulk substrate to eliminate the need for micromanipulation (as shown in Figure 2.6). As a result, the substrate acts as the lower compression platen during the test.

The influence of the substrate on the microcompression results is proven to be negligible [90]. Commercial nanoindentation systems are commonly used as the mechanical test frame, in which the sharp indentation tip is replaced with a flat-punch tip. The load and displacement resolutions of most nanoindentation systems are well suited for microcompression testing because they typically produce stress-strain curves with microstrain and sub-megapascal resolution for micrometer-scale samples

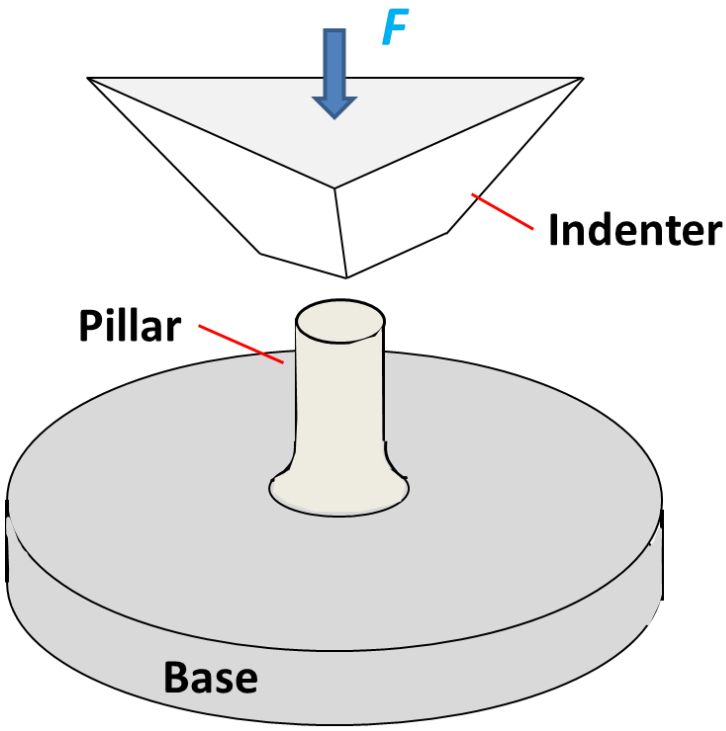

Figure 2.6. Schematic drawing of microcompression of a pillar on its base.

The micropillars used in microcompression were fabricated via focused ion beam (FIB) micromilling, which allows one to serially manufacture micro-scale samples. The FIB milling employs highly localized sputtering of energetic ions to micro-machine small compression samples into the surface of the bulk specimen. FIB systems are uniquely suited to fabricate 3D structures while maintaining sub-micron precision in a variety of metallic and non-metallic systems [91].

Quanta 200 3D Dual Beam (FIB / SEM) FEI instrument was used for this study, and the FIB column on the instrument supplies 30 kV Ga+ ions with beam currents ranging from 0.001 to 20 nA. The micro-sample fabrication process begins with the preparation of the bulk material of interest. A small section of a bulk material is polished using standard metallographic methods to a mirror finish surface. The process for fabricating the micropillar was optimized to minimize taper and rounding at the top edges while still allowing fairly rapid fabrication. This method involves sequential milling of concentric rings with decreasing diameters as normal ion beam incidence to the sample surface. In the meantime, lower ion current was applied to refine the specimen geometry and reduce the ion beam damage in the side surface layer of the micropillars. The 20 μm outer diameter of the trench around the pillar leaves space for the punch during microcompression testing. Pillars with diameters around 1 μm and heights around 2 μm were milled. This aspect ratio (ratio between height and diameter) is large enough to avoid inhibition of shear band propagation by the constraint of the underlying material and small enough to avoid possible complications from plastic buckling. A constant

aspect ratio also keeps the relative contributions from friction and constraint at the ends of the columns constant.

CHAPTER 3 Cooling Rate Effect on Quasi-Static Mechanical Properties of Metallic Glass

3.1 Introduction

Metallic glasses (MGs), as a relatively new class of metallic materials, have received considerable attention due to their unique physical and mechanical properties [1, 13, 20, 92, 93]. Lacking long-range periodicity, MGs can be considered as solids with frozen-in liquid structures, which are composed of tightly bonded atomic clusters and free-volume zones [94]. Being in a metastable state, the glassy structure of MGs is most likely to be affected by different variables arising in the process of materials preparation, for example, cooling rate, overheated temperature, and impurities [73, 95, 96], among which the cooling rate was thought to play an important role in the vitrification of MGs [97-99]. In that case, it was argued that the mechanical properties of MGs could also be affected by the cooling rate [98, 100]. The increase of the cooling rate may result in configurationally looser atomic packing and thus, more free-volume zones [45, 101], which therefore contributes to larger plasticity [60, 102, 103]. However, the cooling-rate effect on the yield strength of MGs is yet to be conclusive [61, 102, 104]; meanwhile, the studies

concerning the cooling rate effect on the elastic behavior of MGs are limited. In view of these, further research effort is thus necessary for clarifying the aforementioned cooling rate effect.

Through a nanoindentation study, Jiang et al. recently reported that the as-cast bulk $Cu_{60}Zr_{30}Ti_{10}$ metallic glasses had higher Young's moduli and hardness than the ribbons of the same composition [64]. They attributed this to the less amount of free-volume zones in the bulk samples than in the ribbon samples, therefore reaching the conclusion that a faster cooling rate favors more free-volume zones. However, it should be pointed out here that, in the original indentation method developed by Oliver and Pharr, the testing sample was assumed to have a semi-infinite geometry [71]. The neglecting of such an implicit assumption when testing samples of finite dimensions, such as thin ribbons, could result in a sample thickness effect in nanoindentation, which tends to underestimate the true material's Young's modulus [64]. Unfortunately, the sample-thickness effect was somehow ignored by Jiang and co-workers, which means that it is necessary to carry out additional experiments as to clarify the cooling rate effect. In this chapter, the research work involved was organized as follows. Firstly, nanoindentation tests based on the Oliver & Pharr's approach were carried out to investigate the cooling rate effect on the Young's modulus and hardness of bulk and ribbon MGs; secondly, the same testing method was extended to the MG samples with the same thickness but obtained at different cooling rates; thirdly, finite element analyses (FEA) was performed to mimic the nanoindentation tests and assess the thickness effect on the extracted

mechanical properties; finally, microcompression was utilized to verify the cooling rate effect on the Young's modulus and yield strength of the MGs.

3.2 Experimental Procedure and Numerical Simulation

A quinary alloy of nominal composition $Zr_{55}Pd_{10}Cu_{20}Ni_5Al_{10}$ (atomic percentage) was chosen for the investigation due to its excellent glass-forming ability [105]. The master alloy ingots were prepared by arc-melting a mixture of the constituent elements with purity better than 99.9% in a Ti-gettered high purified argon atmosphere. Each ingot was re-melted several times to ensure the homogeneity of chemical composition. The bulk samples with diameter of 5 mm (Bulk I) and 1.5 mm (Bulk II) were produced by arc-melting and suction casting the ingots into a copper mold. The ribbon samples were prepared by remelting the ingots in a quartz tube and ejecting through a nozzle onto a copper wheel rotating at velocities of 2000 r/min (Ribbon I) and 4000 r/min (Ribbon II). The resulting ribbons had the dimensions of 44 μm (thickness) × 1.1 mm (width) and 20 μm (thickness) × 1.3 mm (width) respectively. After that, the amorphous structures of these as-cast bulk and as-spun ribbon samples were confirmed by X-ray diffraction and Differential Scanning Calorimetry (DSC).

To measure the mechanical properties of the MG samples, standard nanoindentation method based on the Oliver and Pharr's approach was used to measure the Young's modulus and hardness of the MGs [106]. Prior to the nanoindentation tests, the surfaces of the MG specimens were mechanically polished to a mirror finish using 0.3-μm diamond paste. The standard Berkovich nanoindentation tests were then carried out at a constant loading rate of 10 mN/s with a peak load of 50 mN on the Hysitron TriboScratch® Nano Indenter. To clarify the sample thickness effect, slice samples with different thicknesses, ranging from 20 to 1550 μm, were sectioned employing wire cutting from the center of a bulk MG sample with diameter of 5 mm and subsequently tested using the same nanoindentation approach. For each sample, at least seven nanoindentation tests were carried out to obtain reliable data.

Supplementary to the experiments, numerical simulations of the nanoindentation tests were performed using the commercial package Abaqus™. A conical rigid indenter with a semi included angle of 70.3^{o} was used in the FE model. For brevity, some details of building the FE model, such as meshing and checking of the influence of boundary conditions, which are not relevant to this particular problem, are omitted here. Interested readers may be referred to Ref. [107]. For simplicity, a rod-shaped MG specimen instead of a ribbon MG specimen was constructed in the FE model. In doing so, the three-dimensional FE problem is simplified to an axisymmetric one. To mimic the real indentation experiments, the MG sample and the substrate epoxy resin were assumed as elastic-perfect-plastic solids, and the MG-epoxy interface was taken as cohesive throughout the whole simulation.

Apart from nanoindentation, microcompression tests were also performed on both bulk and ribbon MG samples. To evaluate the cooling rate effect, micropillars were fabricated on the surfaces of one bulk (diameter 5 mm) and one ribbon (thickness 20 μm) sample using a dual-beam scanning electron microscopy (SEM)/focused ion beam (FIB) system (Quanta 200 3D, FEI). Following the sequential ion-milling approach [19], a series of micropillars having respective top diameters and aspect ratios ranging from ~1 to ~ 4 μm and 2:1 to 5:1, were carved out on the surfaces of the bulk and ribbon samples and later tested using a 10-μm flat-end conical diamond indenter with load control.

3.3 Results and Discussions

According to Lin and Johnson [85], the cooling rate, *R*, of MGs can be estimated as $R=10/t^2$, where *t* is the cooling thickness of a MG sample. Based on this equation, the cooling rates of Bulk I, Bulk II, Ribbon I, Ribbon II were estimated as 1.60×10^2, 1.78×10^3, 6.25×10^5 and 3.09×10^6 K/s, respectively. Thus, the difference in cooling rates is over four orders of magnitude.

The XRD patterns of the prepared samples are shown in Figure 3.1, where only diffuse humps without any indication of crystalline Bragg peaks can be detected, this indicates that full amorphous structure are obtained in all of the samples.

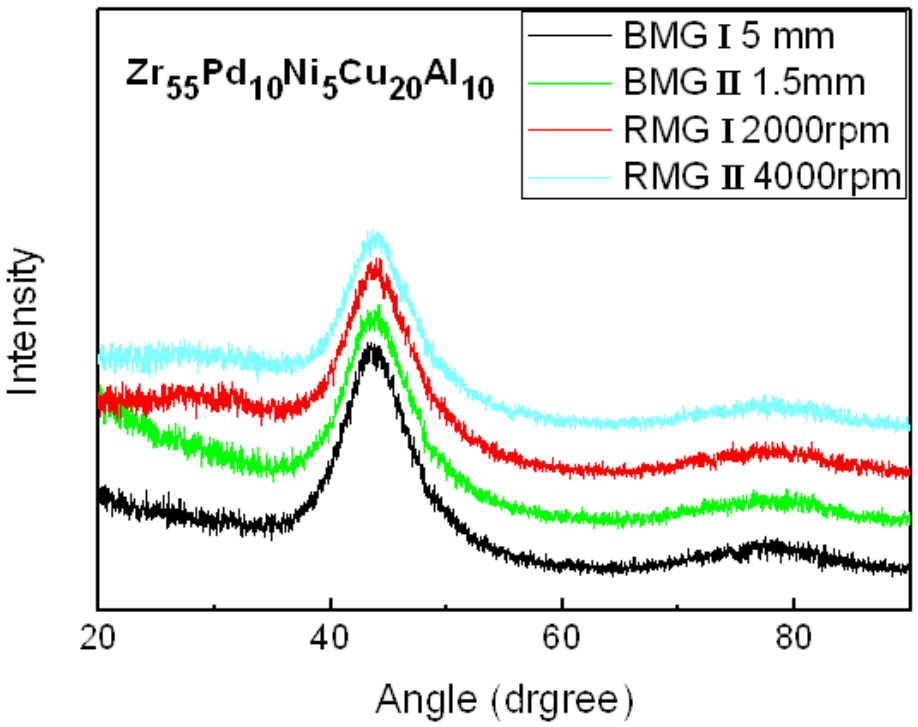

Figure 3.1. XRD patterns of the Zr-based MGs with different cooling rate.

Figure 3.2 gives the continuous heating DSC curves of the bulk and ribbon $Zr_{55}Pd10Cu_{20}Ni_5Al_{10}$ MGs, the thermal analysis was carried out with heating rate of 20K/min. It can be clearly seen that there exists one pronounced exothermic peak, indicating that the crystallization process of both the bulk and ribbon samples. The thermodynamic properties of the MGs associated with glass transition temperature, T_g, and crystallization temperature, T_x, were measured, the results are listed in Table 3.1. It can be seen that T_g for the ribbon sample is larger than that for the bulk one. Increasing the cooling rate from 10^2 to10^6 K/s caused T_g increase from 693 to 712K, a 2.7% increment, this increase is negligible, as the relation between the glass transition

temperature and strength of metallic glass have not been accurately quantified [108]; while, the crystallization temperature T_x are relatively stable for the MGs prepared with different cooling rate, which is around 776 K. In addition, we find that increasing cooling rate from 10^2 to10^6 K/s caused glass transition temperature increase

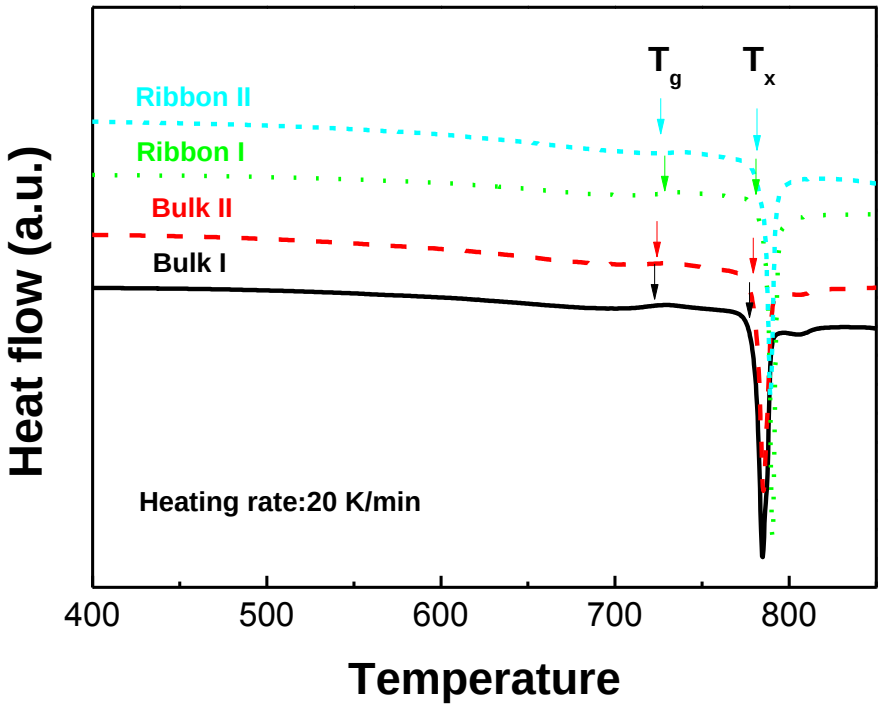

Figure 3.2. DSC curves of the Zr-based MGs rod and ribbon samples.

Table 3.1. Young's moduli and hardness of the metallic glass samples with different cooling rate

Samples	Thickness(μm)	Tg (K)	Tx (K)	E (GPa)	H (GPa)
Bulk I	5000	693	776	96.8±0.8	5.3±0.1
Bulk II	1500	696	775	94.0±1.2	5.3±0.1
Ribbon I	44	709	777	77.8±1.5	5.5±0.1
Ribbon II	20	712	776	63.7±1.3	5.4±0.2

Typical indentation load-depth curves of the $Zr_{55}Pd_{10}Cu_{20}Ni_5Al_{10}$ bulk and ribbon MG samples are presented in Figure 3.3. It is apparent that the maximum indentation depth is dependent on the cooling thickness and, thus, the cooling rate used during sample preparation. With the increasing cooling rate, the maximum indentation depth increases, as consistent with the previously finding [64]. However, it is worth mentioning that, for the ribbon samples corresponding to different cooling rates, the difference in the maximum indentation depths is small. To minimize the effect from the epoxy resin (as shown in the set of Figure 3.3), all the indents were made in the middle of the ribbon samples' cross sections. Note that the indent has a size of ~3 μm and the distance between two indents is at least 30 μm apart.

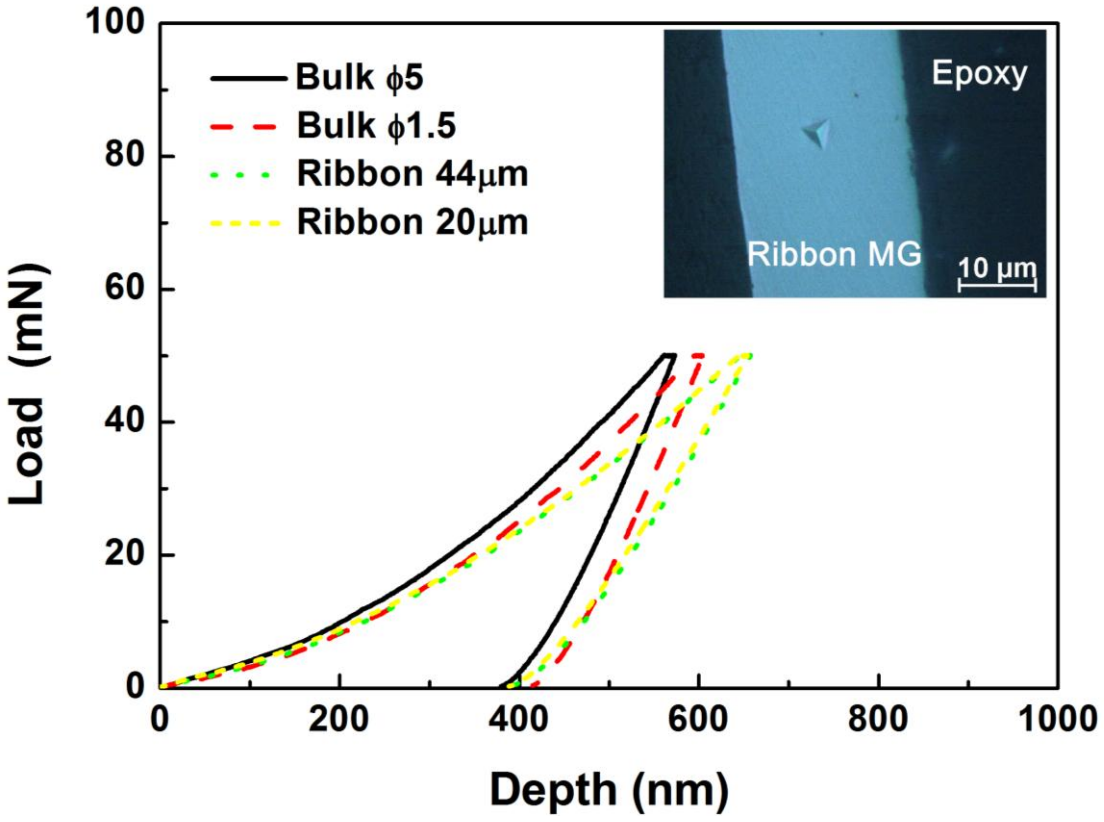

Figure 3.3. Typical load-depth curves of the MG samples with different cooling rate. The inset is the position of indent in the ribbon sample.

Following Oliver and Pharr [106], the Young's Moduli and hardness values were extracted from the nanoindentation load-depth curves and the results are listed in Table 3.1. Interestingly, the measured hardness values for all MG samples are about 5.3-5.5 GPa, essentially independent of the cooling rates. If the empirical relation between hardness and yield strength, $H \approx 3\sigma_y$ [109], was used, the estimated yield strength of the $Zr_{55}Pd_{10}Cu_{20}Ni_5Al_{10}$ MGs would be around ~1.8 GPa, which agrees quite well with the previous experimental results obtained from uniaxial compression tests [105]. The

invariance of the hardness implies that the cooling rates, spanning four orders of magnitudes though, do not cause any apparent changes in the yield strengths of the MGs. In sharp contrast, the measured Young's moduli drop substantially from ~ 97 to ~ 64 GPa when the testing sample thickness reduces from 5000 μm to 20 μm, or the corresponding cooling rate increases from about ~10^2 to ~10^6 K/s. Note that this trend is consistent with the finding reported in Ref. [64]. In addition, through the thermodynamic parameters in Table 3.1 obtained from the DSC curves, it can be noted that the glass transition temperature (T_g) increases slightly with cooling rate, rising from 693 to 712 K when the cooling rate increases form about ~10^2 to ~10^6 K/s, while the crystallization temperature is relatively stable around 776 K. The small change of the glass transition temperature indicates that the internal atomic structure has changed in certain degree, but this change is not sufficient enough to be revealed in the hardness data.

Since a material's Young's modulus, E, can be related to the material's inter-atomic potential and inter-atomic distance, we can have [110]:

$$E = V\left(\frac{d^2U}{dV^2}\right) = kr\frac{\partial}{\partial r}\left(\frac{1}{r^2}\frac{\partial U}{\partial r}\right) \tag{3.1}$$

where V is the atomic volume, U is the inter-atomic potential, r is inter-atomic distance and k is a material constant. Normally, decreasing inter-atomic potential will lead to a lower elastic modulus given an unchanged inter-atomic distance. Since the tested MGs are of the same chemical composition, a similar shape in the inter-atomic potential is expected. Therefore, it is unlikely that the difference of four orders of magnitudes in the

cooling rate, which only causes a density difference of less than 2% during materials preparation [101], can result in such a significant reduction in the Young's modulus.

To clarify whether other factors are responsible for the observed decrease in the Young's Modulus, three slices were cut from the center of a 5-mm bulk MG rod, which had the respective thickness of 20 μm (S1), 88 μm (S2) and 1550 μm (S3), and subsequently tested using the same nanoindentation approach. The measured Young's moduli and hardness of the slice samples are listed in Table 3.2. Interestingly, the measured Young's moduli from Sample S1 and S2 are ~63 and ~80 GPa, respectively, much lower than that of the bulk sample from which the slices were cut. In contrast, the measured Young's modulus of Sample S3 slice is ~94GPa, almost the same as that of the bulk sample. The experimental finding clearly demonstrates that varying sample thickness can greatly affect the material's Young's modulus measured from the nanoindentation. In comparison, the hardness measured from S1 to S3 shows no remarkable change with the varying sample thickness, which is consistent with the previous nanoindentation results obtained from the MG samples of different dimensions.

Table 3.2. Young's moduli and hardness of the slice and bulk metallic glass samples with the same cooling rate

	Slices cut from Bulk Φ5			**Bulk Φ5**
	S1	S2	S3	Zr5
Size (μm)	20	88	1550	5000
E (GPa)	63.42 ±2.34	79.87 ±2.90	94.30 ±1.09	96.80 ±0.81
H (GPa)	5.18 ±0.05	5.51 ±0.10	5.51 ±0.11	5.26 ±0.13

Figure 3.4(a) presents the measured Young's moduli of the bulk, ribbon and slice MG samples. It is evident that the Young's moduli of the ribbon and slice samples are very close, exhibiting the same trend with the varying sample thickness. This experimental finding unambiguously proves that the seeming difference between the measured Young's moduli of the ribbon and bulk MG samples is mainly caused by the sample thickness instead of any physical change in the underlying atomic structures. In contrast, Figure 3.4(b) shows the extracted hardness data of the bulk, ribbon and slice MG samples, which consistently display the trend of a constant value within the range of sample thickness from 20 μm to 5000 μm. This behavior can be understood as follows. From the mechanistic viewpoint, the Young's modulus reflects the rigidity of an elastically deformed volume and depends on the imposed boundary conditions, which becomes the 'source' of the sample thickness effect. However, hardness reflects the material's resistance to local plastic flows and is therefore less sensitive to the boundary conditions.

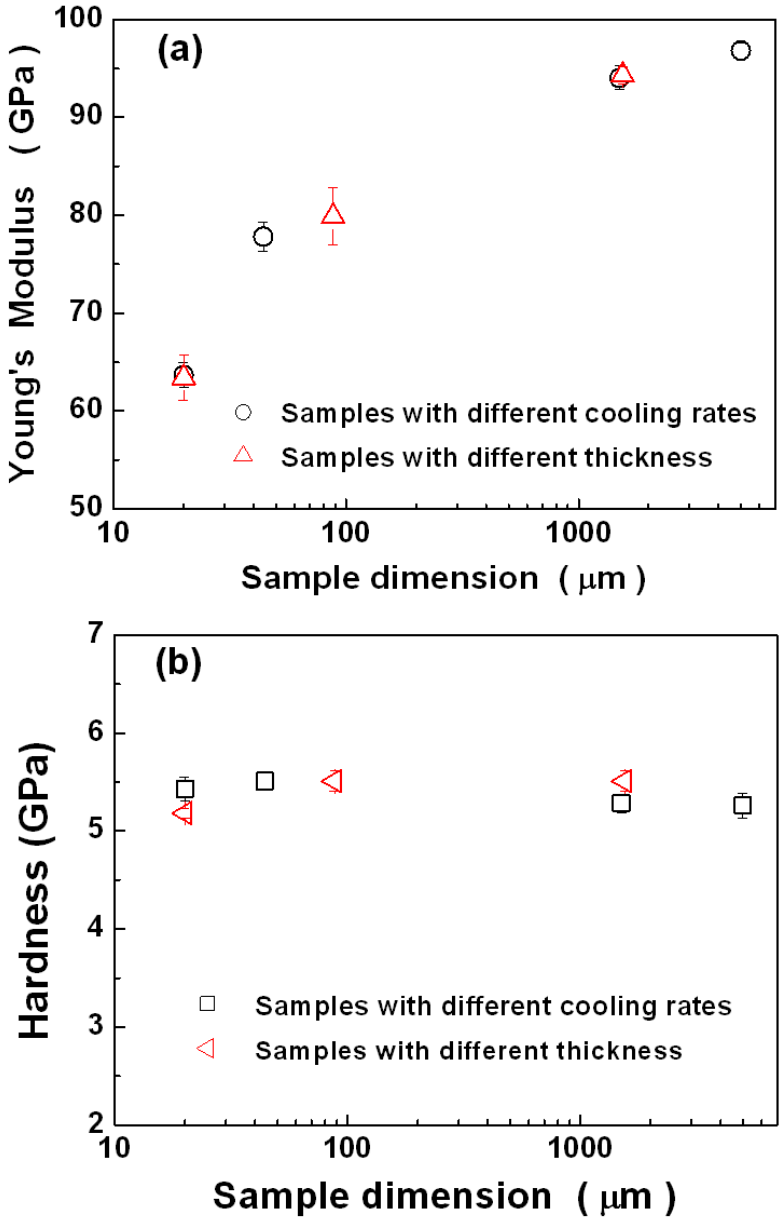

Figure 3.4. (a) Young's modulus of bulk vs. ribbon (different cooling rate) and bulk vs. slice (different thickness) glassy samples. (b) Hardness of bulk vs. ribbon (different cooling rate) and bulk vs. slice (different thickness) glassy samples.

To verify the above arguments, FE simulations were carried out and the results are presented in Figure 3.5 in comparison with the experimental data. Considering the difference of the sample geometry between the real and simulated MG samples and the uncertainties around the MG-epoxy interface, the simulation was motivated here only to check if the general trend of the experimental data could be captured. The procedure for 'calculating' the material's Young's modulus and hardness from simulation is as follows. First, the elastic-perfectly-plastic MG FE model was assigned with a Young's modulus of 95 GPa and a yield strength of 2.2 GPa, and the epoxy in the vicinity of the MG model with the Young's modulus of 2 GPa and a yield strength of 0.04 GPa. Second, indentation was simulated by pushing the rigid conic indenter into the center of the MG model and, then, retracting the indenter backwards for unloading. After that, the Young's modulus and hardness were computed from the simulated load-displacement curves following the method proposed by Oliver and Pharr [106]. As shown in Figure 3.5, the simulation results generally follow the trend of the experimental data in spite of the aforementioned model simplification, which, again, corroborate our previous conclusion that there should be no significant difference between the hardness and modulus of the MG bulk and ribbon samples.

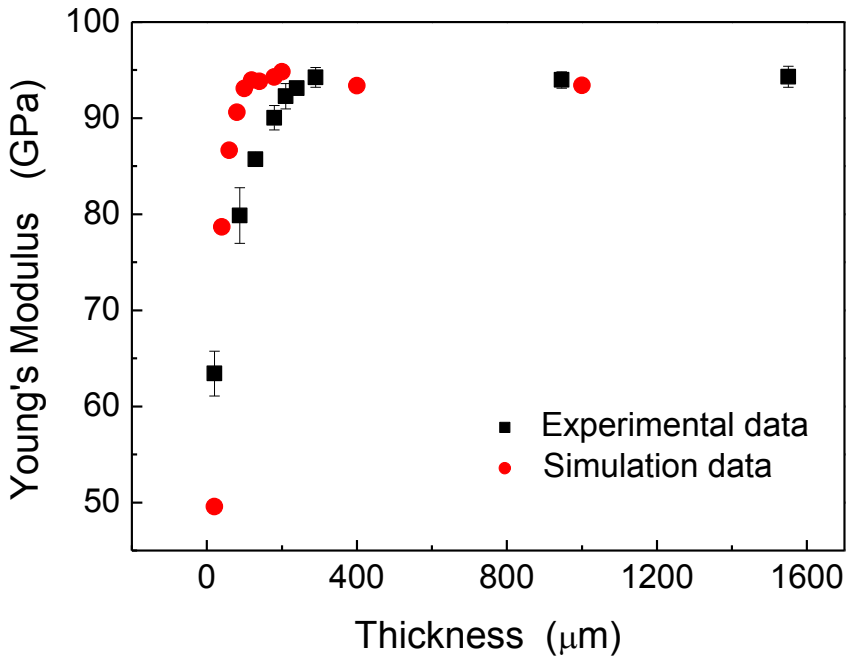

Figure 3.5. Young's modulus dependence on sample thickness from experimental and simulation results.

To exclude the confounding effect of sample thickness, microcompression tests were used to extract the mechanical properties of the bulk and ribbon MG samples. As shown in Figure 3.6, a few micropillars were carved out on the surface of the 20-μm thick MG ribbon sample. Due to the ion-beam divergence, the micropillars were slightly tapered with an average taper angle of ~2 degrees.

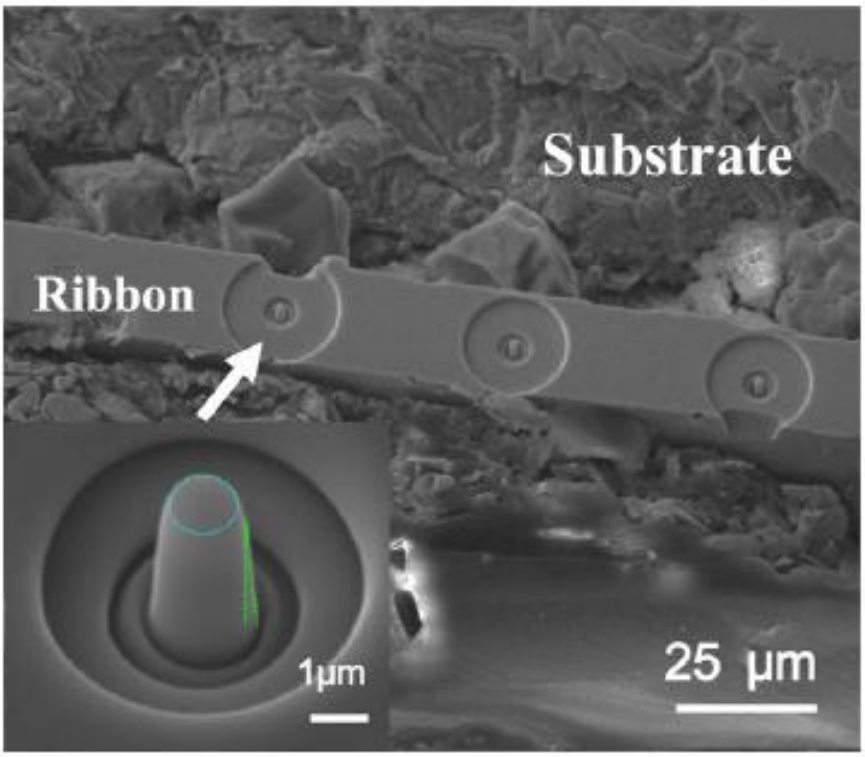

Figure 3.6. Position of the fabricated micropillars in ribbon sample. Inset is the representative geometries of one micropillar.

The microcompression experiments were subsequently conducted at a loading rate of 0.2 mN/s and the typical load-displacement curves are shown in Figure 3.7, from which the Young's modulus and yield strength of a MG micropillar can be extracted. For micropillars with slight tapering, the Young's modulus, E, and yield strength, σ_y, can be obtained using the methods proposed by Yang et al. [111, 112]. As listed in Table 3.3, it can be seen that the Young's moduli and yield strengths of the micropillars cut from the bulk and ribbon samples are almost the same, with the average value being ~88 GPa and 2.2 GPa, respectively. This further confirms that the cooling rate has a negligible effect

on the Young's modulus of MG samples. Before proceeding, it is worth mentioning that the Young's modulus obtained from microcompression is about 5% lower than the values extracted from nanoindentation tests. This is because of the material's pile-up effect, which was not taken into account in the original Oliver and Pharr's method [106]. For MGs, the neglecting of such a pile-up effect will lead to an overestimation of the material's Young's modulus [113]. In addition, the yield strengths obtained from the microcompression tests appear to be higher than those from the conventional uniaxial compression tests [105], which is usually attributed to the Weibull statistics as already discussed in the literature [114].

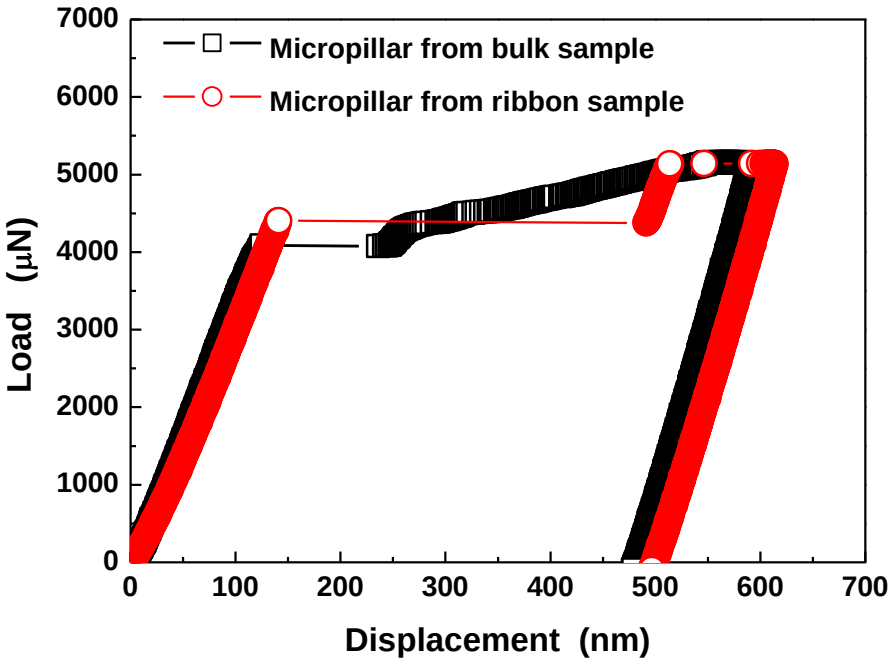

Figure 3.7. Typical microcompression load-displacement curves of the micropillars.

Table 3.3. Young's moduli and yield strengths of the micropillars carved from bulk and ribbon samples with different cooling rate

Micropillars	E (GPa)	σ_y (GPa)
From bulk sample	88±5.7	2.2±0.1
From ribbon sample	88±2.6	2.3±0.2

3.4 Implications

Based on the above analyses and discussions, we have demonstrated that the cooling rate used in our study, ranging from ~10^2 to ~10^6 K/s, does not cause any remarkable change in the Young's modulus and hardness of the Zr-based MG samples, though small changes in the glass transition temperature have been detected. This is implicative of a similar atomic structure in the MGs in spite of the large cooling-rate difference. The reason might lie in two folds: (1) the cooling rates employed in this study were still below a critical value, only above which a sufficient structural change can be detected from the hardness and Young's modulus of MGs [101]; and (2) the overheat temperature, from which the molten metals were quenched, was not high enough for the atomic clusters and free-volume zones to rearrange [115]; in other words, the atomic structure of the metallic glass

was mainly determined by the overheat temperature rather than the cooling rate imposed during quenching process.

3.5 Conclusions

Based on the current work, we find that the cooling rate has a negligible influence on the Young's modulus and hardness of the $Zr_{55}Pd_{10}Cu_{20}Ni_5Al_{10}$ metallic glass, which is contrary to the previous findings [64]. The apparent reduction in the Young's moduli of the ribbon samples relative to those of the bulk samples, as measured using nanoindentation, has been proved simply caused by the effect of sample thickness. After eliminating such a sample geometry effect, the cooling-rate independent mechanical properties were attained. Such an insignificant influence of the cooling rate on the Young's modulus and hardness of the Zr-based MG implies that a faster cooling rate is needed for further research or the overheat temperature is not high enough to introduce any significant physical change in the glassy structure of the Zr-based MGs.

CHAPTER 4 Cooling Rate Effect on Dynamic Mechanical Properties of Metallic Glasses

4.1 Introduction

In the literature of glassy materials, their dynamical behavior in the supercooled liquid region has been attracting great research interest over the past decades [116-122]. Aside from the most prominent α-relaxation in the vicinity of the material's glass transition point T_g, which involves collective atomic/molecular movements across a large number of structural units, it has also been demonstrated that secondary relaxations could also occur below T_g [120, 123, 124], which entails the thermally activated jumps of structural units at local sites. Understanding the localized deformation mechanism related to these secondary relaxations is an important step towards the revelation of the inelastic and plastic deformation mechanisms intrinsic to these glassy materials.

For metallic glasses (MGs), which are amorphous metals lacking the long-range order in their atomic structure, it has already been shown that they could exhibit the anelastic deformation through the secondary β-relaxation in their supercooled liquid state [125]; furthermore, recent experiments showed that they can even undergo anelastic

deformation at ambient temperature [126-128], both of which could be attributed to the reversible motion of their flow defects at low stress levels. In the MG literatures, it has been widely accepted that their inelastic deformation is accommodated at the atomic scale by free-volume zones (FVZs) [129, 130], which are simply clusters of atoms loosely bounded in MGs. These experimental findings of anelasticity in MGs indicate that the individual FVZs should be encaged by an elastic shell, which offers the back stress to restore the material's original configuration upon the removal of external loadings [127]. Such an experimental finding is consistent with the spirit of the longstanding shear transformation zone (STZ) theory [131], which was proposed years ago based on the findings from the bubble shaft experiments, and also agrees with the results of the recent molecular dynamics (MD) simulations that the inelastic deformation induced at low mechanical stresses is reversible in MGs [132].

From the perspective of energy barrier concept, the energy state of a glassy structure can be depicted on a 'ragged' configurational energy, which consists of both deep and shallow energy wells that form a nest structure of different metastable states, as shown in Figure 4.1. The deep energy wells (megabasin) correspond to the energy barriers against irreversible structural relaxations (α-relaxation) while the shallow ones (subbasin), which are nested inside the megabasins, are the energy barriers against reversible structural relaxations (β-relaxation) [125]. For amorphous polymers, both relaxation processes can be characterized using the classic dynamic mechanical analysis (DMA) method and the results are usually related to the motions of their molecular structures [133]. However, the revelation of the reversible structural transition in MGs appears not that straightforward

as in glassy polymers. If the conventional DMA method was used to study the dynamic behavior of MGs, it was found that no significant β-peak could be recognized on the corresponding DMA spectra [134]. The lack of β-peak in MGs is implicative of low internal friction induced at the stress/strain rates which can be afforded in the conventional method. On the other hand, micro- and nano-scale dynamic tests recently emerged as an alternative enabling the application of extremely high stress/strain rates to study the dynamic behavior of MGs [128, 135, 136]. The experimental results clearly show that, like glassy polymers, MGs also deform in an anelastic manner before yielding occurs, which can be attributed to the reversible structural transition taking place at the atomic scale. Although these experimental findings provide us the important evidence to understand the relation between the atomic structure and deformation in MGs, however, there still lacks a rigorous analytic framework that links these observed micro-/nano-scale anelastic deformation phenomena to the atomic-scale deformation process and thus, the intrinsic properties of MGs. In this chapter, we intend to first provide a mean-field model based on the energy barrier concept to bridge the gap between the atomic-scale structural transition events and the resultant microscopic anelastic deformation processes in MGs, and then present and analyze the experimental dynamic tests results of MGs with different cooling rate.

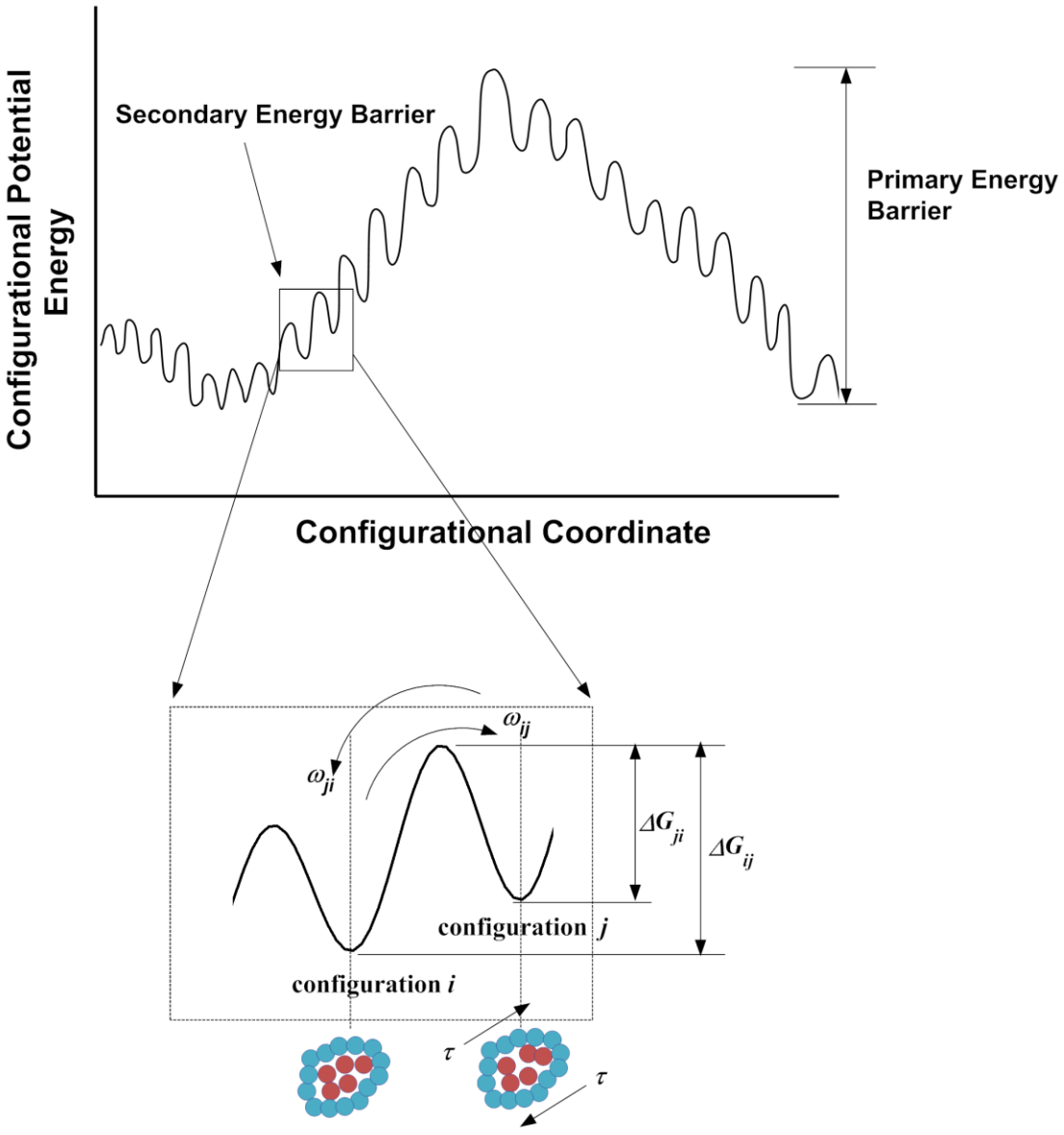

Figure 4.1. The schematic illustration of the configurational potential energy of a core-shell deformation unit, the inset: the barrier-crossing event leading to the constrained configurational change of the free-volume zone (red atoms) encaged by its elastic 'shell' (blue atoms).

4.2 Theoretical Modeling

Different from the original STZ model [131], which was developed mainly for rationalizing elastoplastic transition in MGs, we here consider two additional modeling efforts that could physically lead to anelasticity from a STZ perspective: (1) instead of assuming a smooth energy-barrier profile for a STZ [131], we assume a rather 'ragged' energy-barrier profile for the core-shell unit. As shown in Figure 4.1, whereas the primary saddle point corresponds to the energy barrier against a local plastic event, being physically associated with the break-down of the elastic shell, the numerous secondary saddle points below the primary one are associated with the local metastable state of the FVZs, across which is a constrained structural transition triggered with an intact elastic shell; and (2) by adopting a similar reasoning of Falk et al. [137], we formulate the local inelastic deformation explicitly as a result of unbalanced constrained structural transitions occurring to a multitude of core-shell units rather than of the unconstrained transition to one 'representative' unit resulting in local plasticity as in the original STZ model [131].

Following the transition state theory, the transition rates ω_{ij}^0 and ω_{ji}^0 between two adjacent metastable states *i* and *j* of a un-stressed FVZs (the inset in Figure 4.1) can be expressed respectively as $\omega_{ij}^0 = \nu\, exp\left(-\Delta G_{ij}/kT\right)$ and $\omega_{ji}^0 = \nu\, exp\left(-\Delta G_{ji}/kT\right)$, where ν is the attempt frequency, k is the Boltzmann constant; T is the ambient temperature; ΔG_{ij} and ΔG_{ji} denote respectively the two energy barriers as illustrated by the inset of Figure 4.1. When in thermal equilibrium, we should have $\omega_{ij}^0 \approx \omega_{ji}^0$ or $\Delta G_{ij} \approx \Delta G_{ji}$ to the first order

approximation such that any spontaneous inelastic flows can be neglected within a short term. Suppose that the energy potential is biased towards the metastable state *j* upon mechanical perturbation, we should have the new transition rates approximated as $\omega_{ij} \approx \omega_{ij}^0\left(1+\Omega\tau/kT\right)$ and $\omega_{ji} \approx \omega_{ji}^0\left(1-\Omega\tau/kT\right)$, where τ and Ω denote respectively the applied shear stress and the activation volume of the FVZ for the constrained structural transition, satisfying $\Omega\tau/kT << 1$. Assuming that there are N_i and N_j constrained structural transitions occurring and transforming a multitude of the core-shell unit from the metastable state *i* to *j* and in the reverse direction respectively, we have:

$$\frac{dN_i}{dt} = -\omega_{ij}N_i + \omega_{ji}N_j \tag{4.1a}$$

$$\frac{dN_j}{dt} = -\omega_{ji}N_j + \omega_{ij}N_i \tag{4.1b}$$

Combining Equations 4.1a and 4.1b leads to the following kinetic equation governing the 'flow' of the net transitions directed in the loading direction:

$$\frac{d\chi}{dt} + \left(\omega_{ij} + \omega_{ji}\right)\chi = \omega_{ij} - \omega_{ji} \tag{4.2}$$

Note that $\chi = \left(M - N_i\right)/M = \left(N_j - M\right)/M$ is the fraction of the net transitions and can be viewed as an internal variable linked to inelastic deformation, and $M = \left(N_i + N_j\right)/2$ remains a constant ($dM/dt = 0$) throughout the whole process. Substitution of the expressions for ω_{ij} and ω_{ji} into Equation 4.2 then yields:

$$\frac{d\chi}{dt} + 2\nu\chi e^{-\frac{\Delta G}{kT}} = 2\nu e^{-\frac{\Delta G}{kT}} \frac{\tau\Omega}{kT} \tag{4.3}$$

where $\Delta G=\Delta G_{ij}\approx\Delta G_{ji}$, and $\omega_{ij}^{0} \approx \omega_{ji}^{0}$ is used in deriving Equation 4.3. It is worth mentioning that Equations 4.1 to 4.3 are not specific to MGs, they are derived essentially for a stress-assisted thermally driven process and similar equations can be also derived for a similar process in polymers [133].

Now, the question is how we can relate the fraction of the net transitions, χ, to the overall mechanical strain in MGs. The answer to this question requires appropriately modeling the glassy structure of a MG alloy. In the literature, the widely accepted models are the free-volume and shear-transformation-zone (STZ) model [131, 138], both of which were centered on the accommodation of inelastic deformation by the 'soft' regions in MGs. However, such a theoretical treatment of neglecting the synergy between the 'soft' and 'hard' regions may not be sufficient to understand the atomic-scale deformation process in MGs, as recently pointed out by Egami [139], because the atomic-scale deformation in MGs entails the collaborative motions of the FVZs and their opposite entities, i.e. the elastic atomic-clusters, which are also the other import type of building blocks for the amorphous structure of MGs [140]. In such a sense, here we view the FVZ and its surrounding elastic medium or elastic shell (solid-like atomic cluster) as a couple to form the basic core-shell structural unit of a MG alloy as shown in Figure 4.2(a). As such, the total mechanical strain, γ, corresponding to the applied stress, τ, presumably depends on not only the elastic strain, γ_e, in the elastic shell but also the inelastic strain, γ_i, in the FVZs (Figure 4.2b). Thus, the total strain can be written as $\gamma = \gamma(\gamma_e, \gamma_i) = \gamma\left(\gamma_e, \int d\chi\right)$.

Here, the inelastic strain γ_i is a function of $\int d\chi$ embodying the 'memory' effect typical of the rheological behavior of materials. Before yielding, we should have $|\gamma_i| << 1$. Therefore, expanding γ into the first-order Taylor series yields:

$$\gamma \approx \gamma_e + \beta\chi = \tau/\mu + \beta\chi \tag{4.4}$$

where μ is the shear modulus of the elastic shell in Figure 4.2(a) and $\beta = \partial\gamma/\partial\gamma_i$ denotes the strain component purely caused by the structural transitioning of a FVZ at a constant stress, which reflects the influence of local structural irregularity on the atomic-scale strain in MGs and is of a non-affine nature. Based on the above reasoning, we can finally reach the governing equation for the anelastic deformation in MGs by combining Equations 4.3 and 4.4:

$$\frac{d\gamma}{dt} + 2\nu e^{-\frac{\Delta G}{kT}}\gamma = 2\left(\frac{\beta\Omega}{kT} + \frac{1}{\mu}\right)\nu e^{-\frac{\Delta G}{kT}}\tau \tag{4.5}$$

Comparing Equation 4.5 with the governing equation for a classic Kelvin rheological model as presented in Figure 4.2(c):

$$\frac{d\gamma}{dt} + \mu^*\frac{\gamma}{\eta} = \frac{\tau}{\eta} \tag{4.6}$$

where μ^* and η represent respectively the elastic modulus of the spring element and the viscosity of the dashpot element as shown in Figure 4.2(c). From this governing equation, we can establish the one-to-one correspondence between the anelastic deformation of

MGs and that of the Kelvin model by assigning the following properties to its spring and dashpot elements:

$$\mu^{*} = \mu \frac{1}{1+\beta\Omega\mu/kT} \tag{4.7a}$$

$$\eta = \mu^{*} e^{\frac{\Delta G}{kT}} \Big/ 2\nu \tag{4.7b}$$

Here it is worth pointing out that, unlike that in the regular Kelvin model, the spring modulus derived in Equation 4.7a is not identical to the elastic modulus of MGs but also depends on the ratio $\beta\Omega\mu/kT$, which can be viewed as a measure of how the solid-like shell attribute, μ, of MGs weighs relative to the FVZ attribute, $kT/\beta\Omega$, in determining the 'reversibility' of the whole process. Conceptually, the 'reversibility' of our model, as seen throughout the derivations, is defined based on the conservation of configurational potential energy rather than mechanical deformation. In that regard, the morphology of the FVZ is allowed to change as a 'signature' of the inelastic deformation that remains after transition, as long as the same configurational potential energy can be retained.

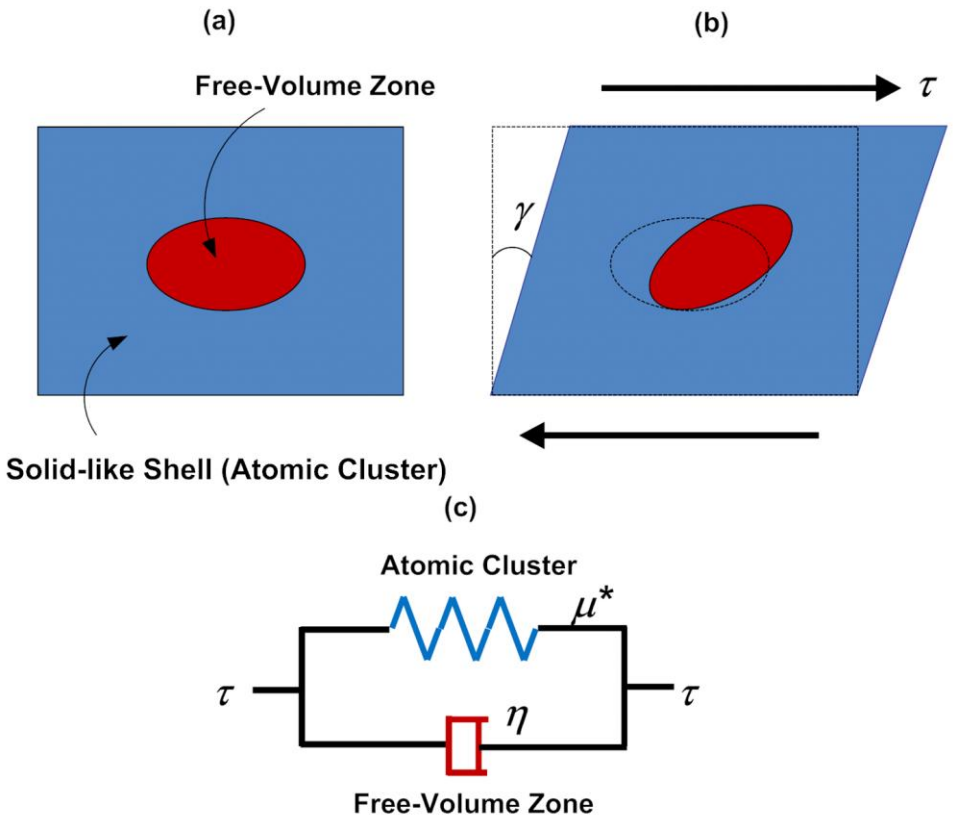

Figure 4.2. The schematics of the (a) undeformed and (b) deformed structural unit of a MG alloy consisting of a free-volume zone (core) and its elastic envelope (atomic cluster); and (c) the equivalent Kelvin rheological structural unit.

4.3 Experimental Procedure

To reveal the anelastic deformation in MGs, one convenient way is to utilize the micropillar compression experiment that was originally designed for probing the size effect in metallic crystals [141]. As compared to the classic DMA method, unusually high stress rates could be applied on small areas via microcompression in a controlled manner

[135]. As a demonstration, metallic glass with the chemical composition of $Zr_{55}Pd_{10}Cu_{20}Ni_5Al_{10}$ (atomic percentage) was chosen. Specifically, one bulk sample with diameter of 5 mm (BMG) and one ribbon sample with thickness of 20μm (RMG) were selected for the dynamic test. Because of adverse effect of casting defects in bulk metallic glass samples, in conventional macroscopic tests it is difficult to reveal the dynamic properties of MGs originate form atomic scale free volume zones, besides, the low precision of the macroscopic testing equipment will conceal the intrinsic reflection of the materials. While, microcompression method based on Hysitron TI 950 TriboIndenter™ has ultrahigh mechanical sensitivity in the dynamic tests, afford us an opportunity to investigate the dynamic response of MGs. The nanoindentation system possess achievable resolution of ~1nm in displacement and ~1μN in load after calibration, high data acquisition rate up to 30 kHz guarantees us to conduct experiments at small timescales which is suitable for microcompression tests. The system enabled the application of load cycles with frequencies up to ~ 300 Hz. It is worth mentioning that the damping factor of the whole system was characterized before microcompression, which was measured around ~0.014 kg s^{-1}. Such machine damping will result in an 'artificial' viscosity of about ~0.05 MPa s when deforming a micropillar of the machined size, which, however, is negligibly small as compared to the experimental results, as can be seen in the later text.

Micrometer-sized pillars with similar geometry, specifically with diameter of ~1 μm, height of ~ 3 μm, and taper angle ~3 °was machined out from the polished surface of the MG samples utilizing the focused ion beam (FIB). The details of micropillars preparation

with the focused-ion-beam (FIB) technique have been described extensively in Chapter 2. Research Methodologies and in other references [135, 141, 142] and are therefore omitted here for brevity. The FEI™ Quanta 3D 200 FIB/SEM dual-beam system was used to fabricate the micropillars, a sequential ion-beam milling approach, with the current density of gallium ion beams decreasing from 5 nA to 100 pA (ensure the lowest ion milling damage and high milling efficiency) and a constant voltage of 30 keV, was utilized to carve out the micropillars.

Prior to the dynamic microcompression tests, basic quasi-static microcompression tests were carried out on the micropillars to obtain static mechanical properties of these samples, as shown in previous chapter. Using methods proposed in ref [143], effects of base compliance and micropillar tapering can be removed, Young's modulus, E, and the yield strength, σ_y, of the micropillar were extracted to be E=88±5.7 GPa, σ_y=2.2±0.1 GPa for the bulk metallic glass, and E=88±2.6 GPa, σ_y=2.3±0.2GPa for the ribbon metallic glass.

The dynamic tests were subsequently conducted using a 10-μm flat-end diamond punch with load control mode. To ensure the response of the micropillar is in the anelastic range, maximum load was selected less than the yielding point; three stress level 0.5GPa, 1Gpa and 1.5GPa were set for the tests. For better data reproducibility, ten load cycles were applied for each run of the dynamic tests. The spectrum of each load cycle was of a triangular shape, consisting of symmetrical loading and unloading portions. It was found

that the number of the load cycles was sufficient to obtain a steady state dynamic response in our micropillar tests.

4.3 Results and Discussions

Amorphous structures of the metallic glass sample, prepared by different cooling rate, were confirmed by X-ray diffraction (Co target), as presented in Figure 4.3, where only diffuse humps without any indication of crystalline peaks can be detected. The XRD patterns cannot reveal any discernable information about the internal structure difference in amorphous structure caused by the different cooling rate in samples preparation.

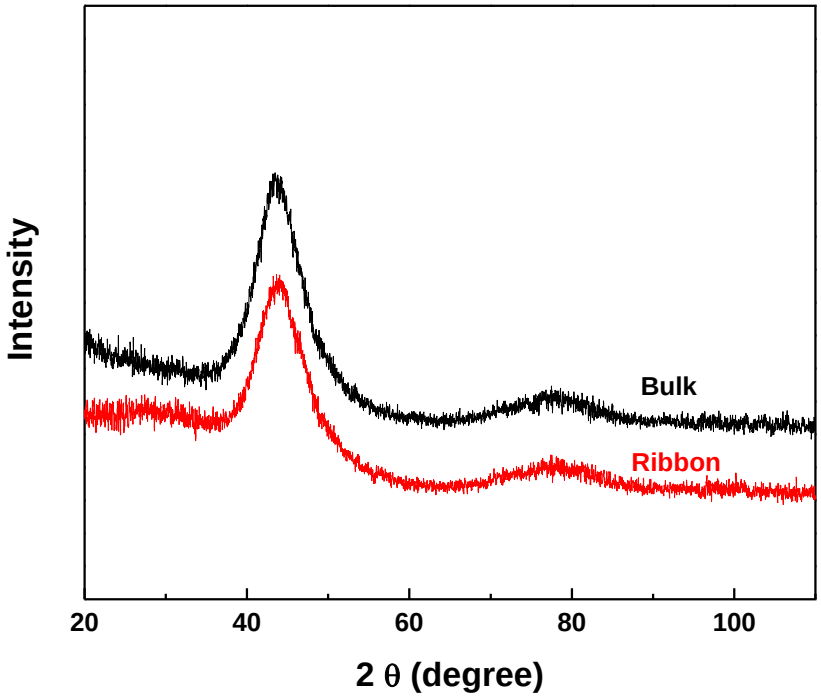

Figure 4.3. The XRD patterns of the as-cast bulk and spun ribbon $Zr_{55}Pd_{10}Cu_{20}Ni_5Al_{10}$ MG sample.

Following the procedure for FIB micromachining [78, 141, 143-145], micropillars of similar dimensions were carved out from the surface of the bulk and ribbon samples. Because of the ion-beam divergence, all the micropillars were slightly tapered with an average taper angle of about ~3°. A typical micropillar is given in Figure 4.4 to demonstrate the geometry of the micropillar.

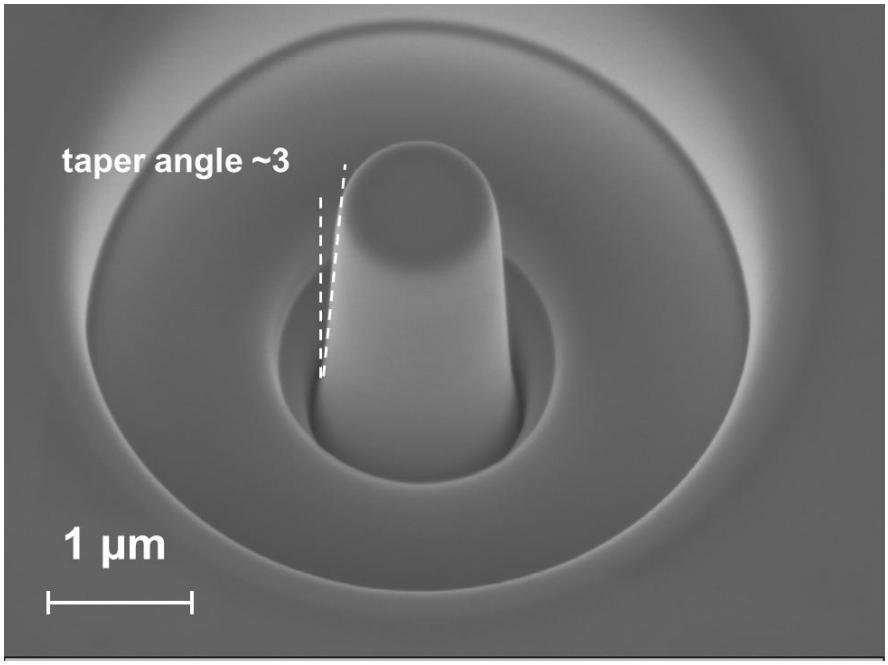

Figure 4.4. High-resolution scanning electron microscopy (HRSEM) image of the FIB-milled micropillar on the surface of the bulk MG sample.

The responses of the micropillars milled out from the BMG under cyclic loading are presented in Figure 4.5. Like revealed in the Ref [37], when loading rate is low at 0.5GPa/s, the micropillar exhibits an apparent elastic behavior as in quasi-static tests we normally observed (Figure 4.5a); when we raise loading rate to 9.8 GPa/s, a mechanical hysteresis loop, which deviates from the pure elastic response, starts to emerge, as shown in Figure 4.5b; further increase the stress rate to 49.3GPa/s and 98.8GPa/s, the hysteresis loop expands remarkably, as presented in Figure 4.5c and d. This surprising response under dynamic test disobey Hooke's law, is the typical anelastic behavior normally possessed by amorphous polymer. Another feature which is worth to mention is that the anelastic deformation, as shown in Figure 4.5b-d, was completely reversible after the

removal of the applied force, and this was confirmed *ex situ* with high-resolution scanning electron microscopy after the dynamic test. The non-zero displacements at the zero loadings, as shown in Figure 4.5b-d, are due to a transient effect caused by the dynamic loading, which vanished with time after the experiments were stopped, as can be seen in Figure 4.6b-d. These anelastic responses of BMG resemble the dynamic response of viscoelastic materials, implying that the underlying atomic structure similarity.

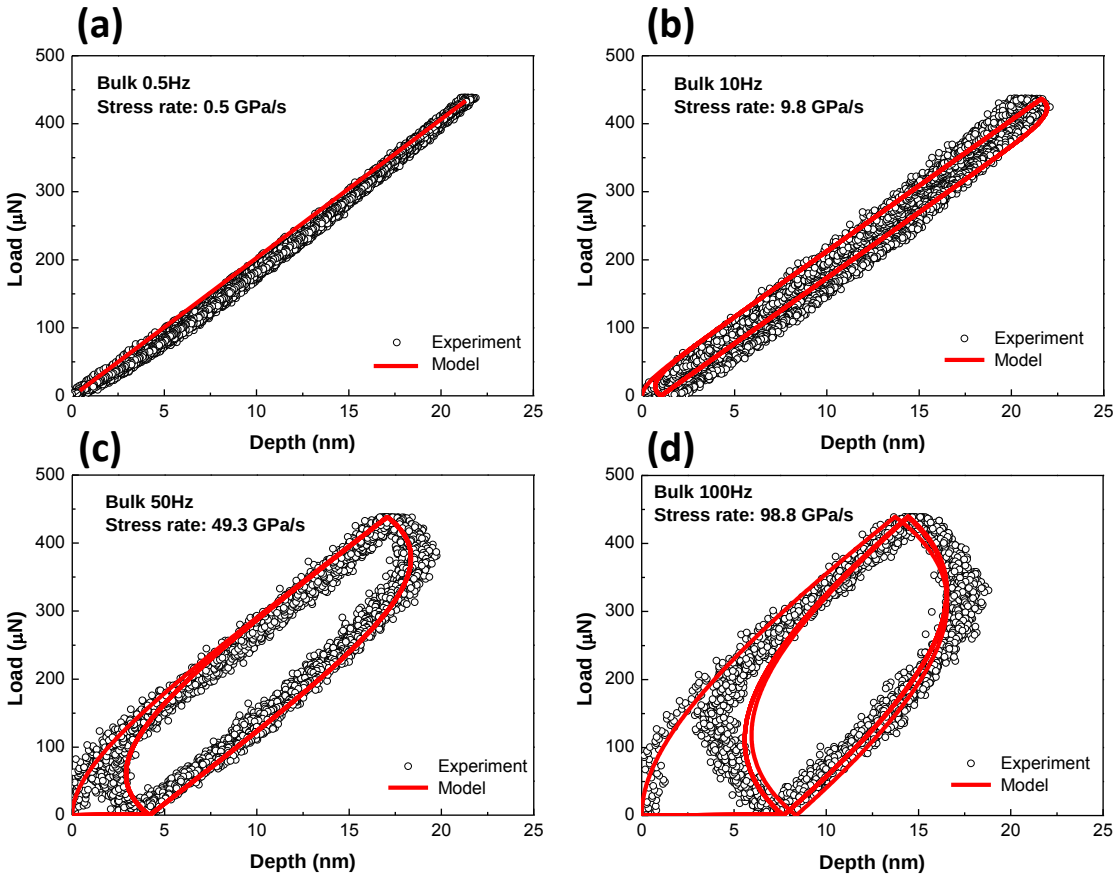

Figure 4.5. (a) to (d): the typical experimental load-displacement curves obtained from the micropillar carved out from BMG at different nominal stress rates in comparison with the results from the phenomenological viscoelastic model, which is equivalent to the proposed 'core-shell' atomistic model (note that the experimental results correspond to a peak stress at 0.5 GPa).

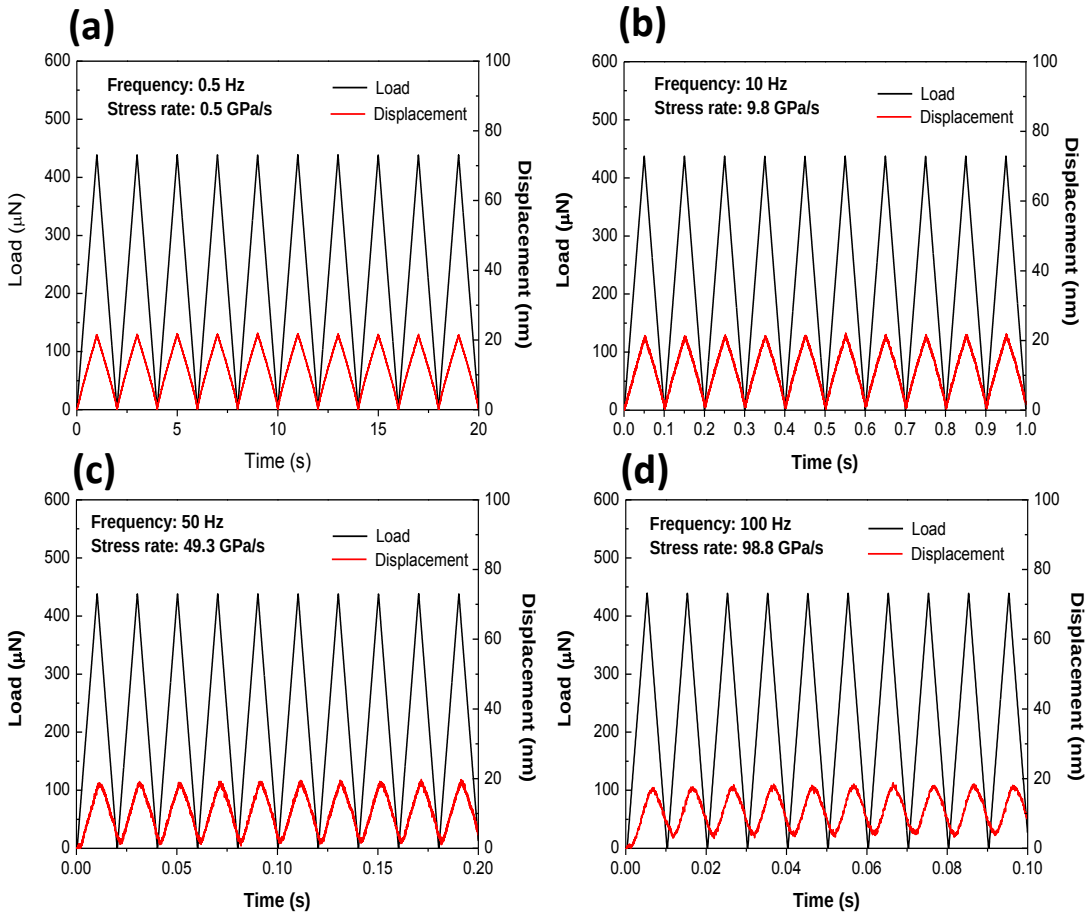

Figure 4.6. (a) to (d): the load and displacement spectra collected at different stress rates corresponding to the load-displacement curves shown in Figure 4.5(a) to (d).

When dynamic tests were performed on the micropillar carved out from the RMG, similar mechanical hysteresis loop can be observed (see Figure 4.7 (b)-(d)), and with the increase of the stress rate, the hysteresis loop becomes more pronounced. Compare the anelastic response curves of the micropillars milled from BMG and RMG samples, no discernable difference can be revealed. In the following part, theoretical model will be used to analyzing the data obtained from dynamic tests.

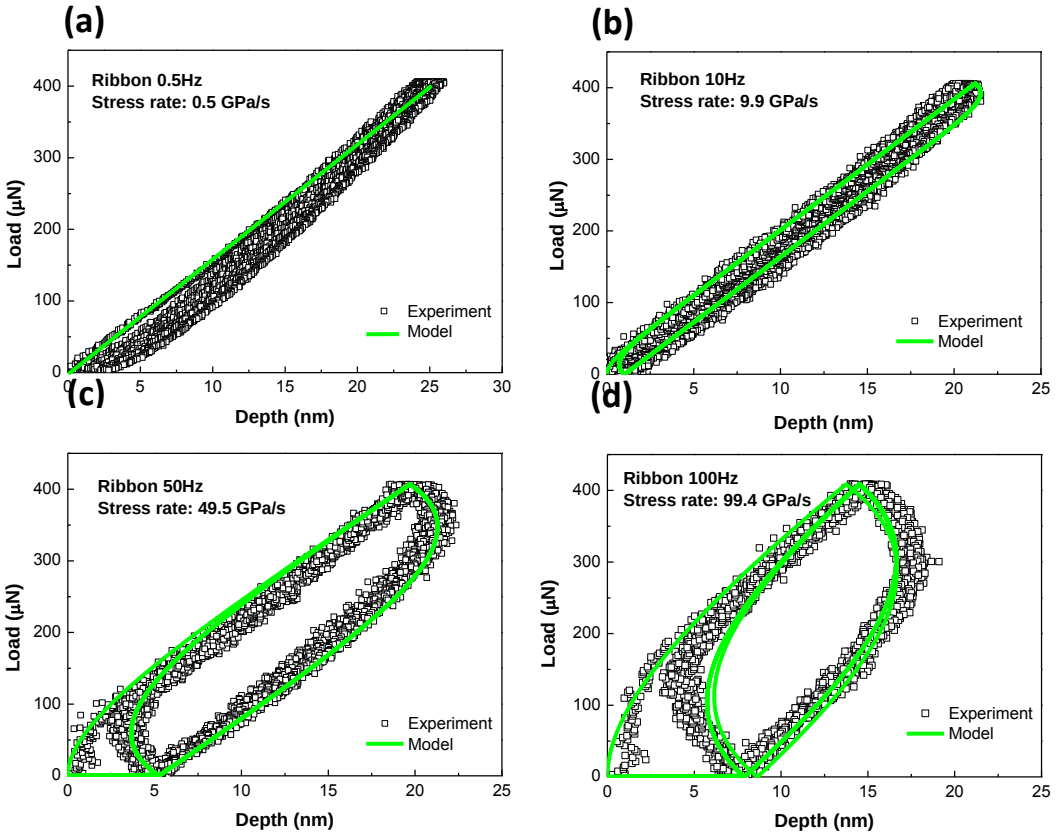

Figure 4.7. (a) to (d): the typical experimental load-displacement curves obtained from the micropillar carved out from RMG at different nominal stress rates in comparison with the results from the phenomenological viscoelastic model, which is equivalent to the proposed 'core-shell' atomistic model (note that the experimental results correspond to a peak stress at 0.5 GPa).

As revealed by Ye et al [37], the anelastic response arise from the soft flow defects FVZs, which become activated at fast loading rate, the activated free volume zone transforms its configuration and dissipates the strain energy during cyclic loading, forms the hysteresis loop. Further speculation leads to the FVZs is enfolded in hard atomic clusters that

behave elastically, such soft FVZ and surrounding hard atomic cluster constitute the basic structural unit (see Figure 4.8).

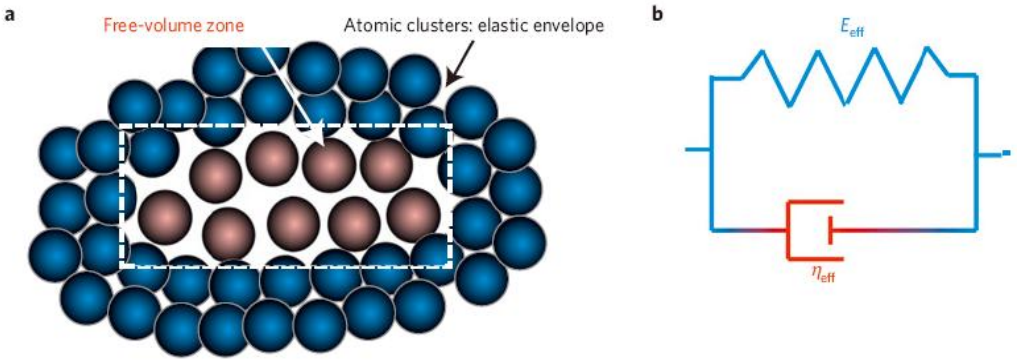

Figure 4.8 The structural origin of the nanoscale inelasticity conceived from the dynamical micropillar tests and the measurements of the mechanical properties of the constituent atomic structures. **a**, Sketch of the core–shell atomistic model in metallic glasses. **b**, The viscoelastic model equivalent to the core–shell atomistic model.

When compressing a micropillar with a height H and diameter D as shown in Figure 4.9(a), the overall anelastic response originates from the cooperative motion of numerous FVZs or an array of Kelvin units, as sketched in Figure 4.8 (b). By converting the stress and strain of shear in Equation (4.6) to those of uniaxial loading, the governing equation that relates the applied load, $P(t)$, to the measured displacement, $h(t)$, of a micropillar can be expressed below using the rule of mixture [135]:

$$\frac{4P(t)}{\pi D^2} = \frac{(1-\chi)E}{H} h(t) + \frac{\chi\eta}{H}\frac{dh(t)}{dt} \tag{4.8}$$

where E is the Young's modulus of the atomic cluster, and χ is the areal fraction of the FVZ. For the sake of discussion, an effective modulus $E_{eff}\left[=(1-\chi)E\right]$ and an effective viscosity $\eta_{eff}(=\chi\eta)$ are defined here. From the experimental viewpoint, these two effective properties are the physical quantities which can be directly extracted from experiments. Under the cyclic microcompression, the response of the micropillar can be represented as an array of f Kelvin rheological units under applied load, as shown in Figure 4.9(c).

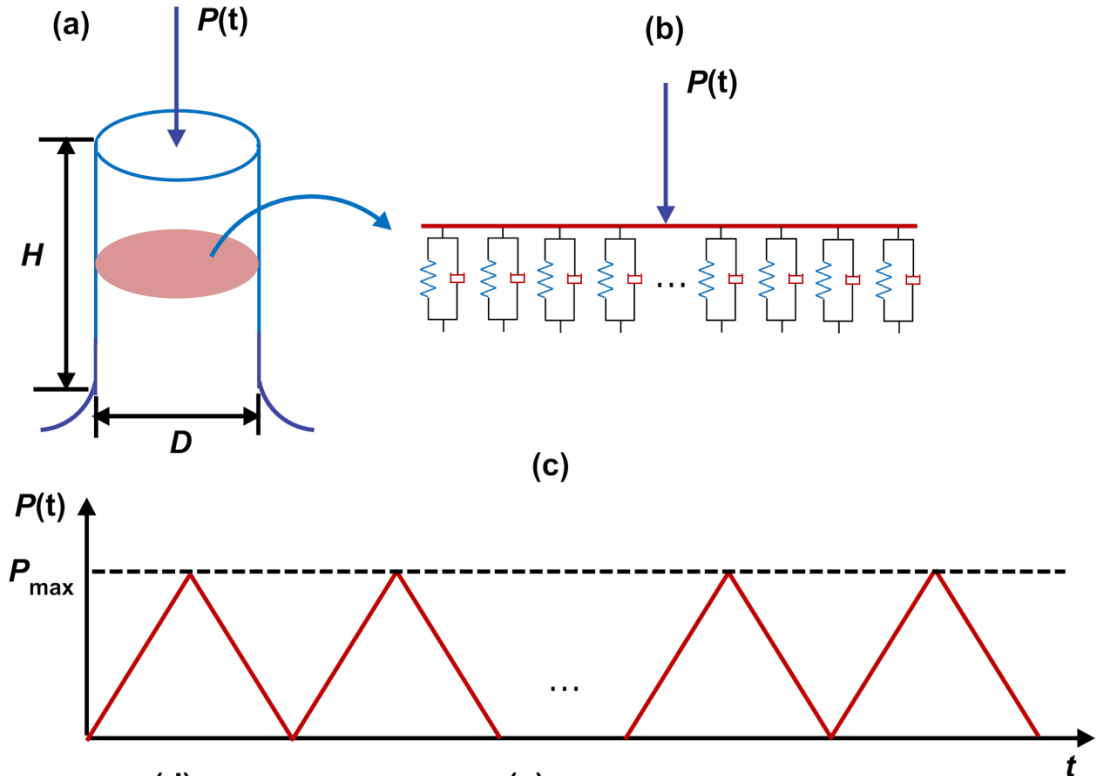

Figure 4.9. The schematic drawing of (a) a compressed MG micropillar, (b) the cross section of the MG micropillar represented by an array of Kelvin rheological units, and (c) the saw-tooth-shaped spectrum of cyclic loading applied in microcompression, and (d) to (f) the micrographs of

the typical micropillars milled out on the mechanically polished surface of Zr- and Fe-based MGs; note that (f) was obtained at a view angle different from that of (d) and (e).

The anelastic hysteresis loop can be well captured by the Kelvin rheological model, as shown in Figure 4.5(b)-(d) and Figure 4.7(b)-(d). It is worth pointing out that when testing frequency is small at 10Hz, the fitted viscosity might be inaccurate, because of the FVZs are not fully activated thus anelastic loop is small, which might incur unnecessary error. So only the data extracted from 50, 100, 150 and 200Hz will be considered for comparison. The extracted effective modulus and viscosity are presented in Figure 4.10, it can be observed that the effective modulus of the bulk and ribbon MGs are almost same at the frequency range from 50Hz to 200Hz, keep constant around 83GPa regardless of the cycle frequency, this indicating that the hard elastic cluster are basically stay in the same configuration despite the cooling rate difference, confirm our previous finding through quasi-static nanoindentation in previous chapter.

For the effective viscosity, though slightly higher viscosity can be observed in ribbon metallic glass, the difference is in the scatter range (about 6%) of the data, as shown in Figure 4.10(b). Therefore, it can be declared that bulk and ribbon samples possess nearly same effective viscosity value at same frequency. It is also noted that there exists a trend, with the increase of the frequency from 50 Hz to 200Hz, viscosity increase from 0.17 to 0.22GPas, an increment of ~ 30%. This indicates a nonlinear viscoelastic behavior and can be attributed to the activation of more FVZs in the high-cycle-frequency regime. Based on the current understanding of the atomic-structure in this Zr-based MG, it can be

conceived that there exist different types FVZs in the sample, which is associated with kinds of atomic clusters and therefore possesses different characteristic activation frequency. In the low-cycle-frequency regime, the FVZs of an extremely short relaxation time remain ‘dormant’ and do not contribute much to the process of energy dissipation; however, they will become activated when the stress rate is elevated. As this takes place, the contribution of these newly activated FVZs will add to the total mechanical energy dissipation, resulting in an apparently elevated effective viscosity as shown in Figure 4.10(b).

Nearly same effective modulus and viscosity were obtained through cyclic dynamic microcompression in the Zr-based MGs with different cooling rate, this agrees with recent studies, which demonstrated that the viscosity behaviors of bulk and ribbon MGs of the same composition are basically same [71, 146]. The nearly equal value of effective viscosity and similar trends in the bulk and ribbon metallic glasses imply that nearly same amount of FVZs which possess similar distribution and configuration exist in the MGs with different cooling rate.

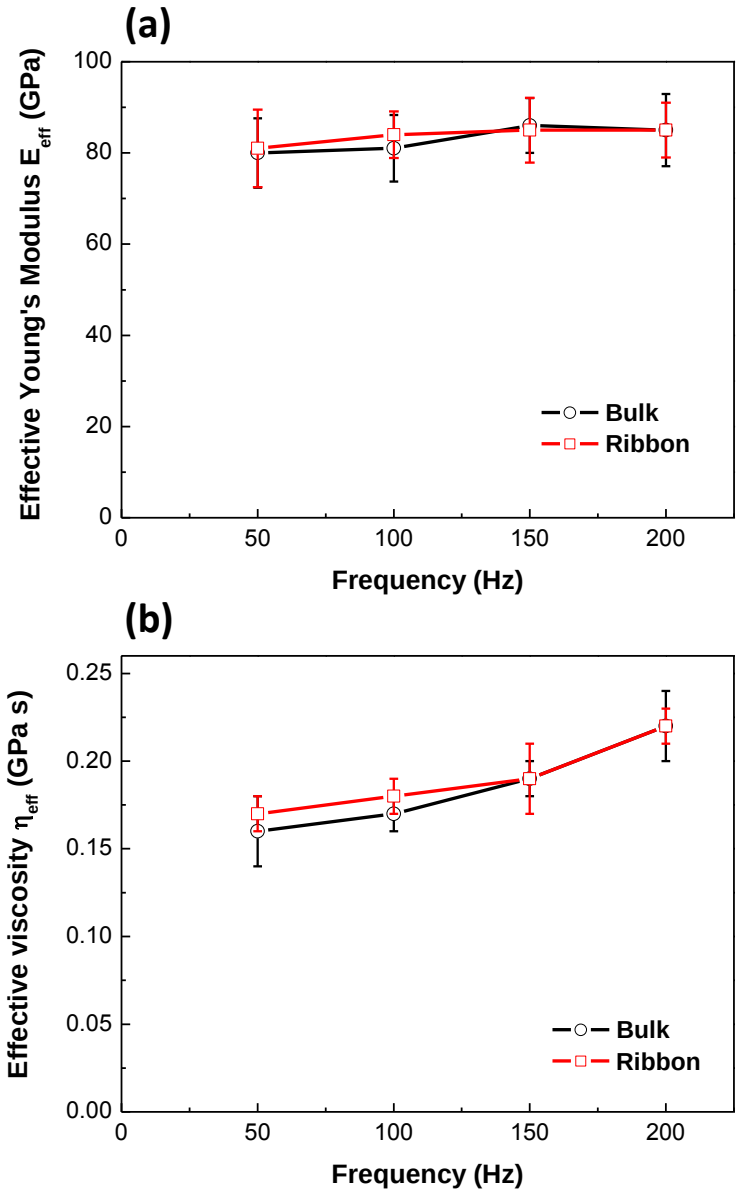

Figure 4.10. Effective modulus and viscosity of the bulk and ribbon metallic glass as a function of frequency.

4.4 Conclusions

Theoretical framework based on the energy barrier concept to understand and analyze the anelastic deformation of MGs was proposed. The theoretical results clearly show that the stress-induced reversible local structural transition in MGs is equivalent to a Kelvin-type anelastic deformation process, and that the viscoelastic properties of MGs obtained from the Kelvin model are closely related to the thermodynamic properties of MGs. Using this theoretical model, dynamic test results of bulk and ribbon MGs micropillars were analyzed, no discernable difference in effective modulus and viscosity can be revealed through our cyclic dynamic test, indicating that similar content of dense packed cluster and FVZs in the bulk and ribbon metallic glass despite the cooling rated difference of about four orders of magnitude.

CHAPTER 5 Size Affected Shear Band Speed in Metallic Glasses

5.1 Introduction

Plasticity in bulk metallic glasses (BMGs) is well known to be shear-band (SB) mediated at room temperature, which manifests as localized plastic flows confined into a banded region with a nano-scale thickness [147]. Owing to the strain localization, SBs accommodate most of the plastic deformation and are responsible for the fracture behavior of BMGs. Unlike dislocations as the plasticity carrier in crystalline materials, SBs generally exhibit a 'size effect' when propagating in BMGs of a different size [76-80]. In large samples, SBs tend to propagate catastrophically if unhindered, causing brittle-like fracture; in contrast, they display the character of 'stick-slip' propagation in small samples, leading to serrated plastic flows in BMGs.

Over the past decades, considerable research efforts have been devoted to understanding different aspects of the shear-banding behavior in BMGs and the accompanying size effects [76-80, 147], among which one topic still remaining not fully understood is what the speed of a mature SB ought to be. In the literature, measurements of such a SB speed have been attempted by different means, such as cinematography [83, 148], strain gauge [84] and acoustic signal detection [81, 149], but seemingly contradictory results, ranging

from ~10 μm s^{-1} to ~1 m s^{-1}, have been reported up to date. Unlike the commonly observed shear slips on the surface of crystals, which is produced by a progressive shearing process mediated by dislocations, shear offsets, the visual manifestation of shear-banding in BMGs, are formed by simultaneous shearing accommodated in SBs, particularly under compressive loading. In such a case, the SB speed, as related to the shear-offset formation, refers to the sliding speed of materials across an already established SB plane. Since it is already known that the magnitude of a shear offset is size dependent in BMGs, it is hence natural to raise the question whether such size dependence still persists in the SB speed. However, in the prior work, the measurement of a SB speed was performed for a particular size of shear offset [82-84], and there still lacks a systematic investigation of the size dependence of SB speed in BMGs. In the present work, we intend to address the above question using the microcompression approach to measure the SB speed at different shear offsets.

5.2 Experimental Procedure

To conduct microcompression experiments, the focused-ion-beam (FIB) sequential milling approach [78, 143] was utilized to fabricate micropillars on the surfaces of a variety of BMGs, including $Zr_{55}Pd_{10}Cu_{20}Ni_5Al_{10,}$ $Cu_{46.25}Zr_{44.25}Al_{7.5}Er_2$, $Ti_{40}Zr_{25}Ni_3Cu_{12}Be_{20}$, $Zr_{55}Cu_{28}Ni_5Al_{10}Nb_2$, $(Fe_{44.3}Cr_5Co_5Mo_{12.8}Mn_{11.2}B_{5.9})_{98.5}Y_{1.5}$, and $Mg_{58}Cu_{31}Nd_5Y_6$.BMGs (Note that the subscript number denotes the atomic percentage of the corresponding element in the alloy). Before the FIB treatment, the BMGs were checked using X-ray diffraction to ensure their amorphous structure and then

mechanically polished to a mirror finish on their surfaces. The details of the FIB milling have been described elsewhere [78, 143] and a total of 31 micropillars was fabricated on the BMG samples with the diameter and aspect ratio ranging from ~ 1 to ~2 μm and 2:1 to 4:1, respectively. Afterwards, microcompression experiments were conducted on the modified Hysitron™ nanoindentation system, which has the resolution of ~1 nm in displacement and ~1 μN in load and was then equipped with a 10-μm flat-end diamond punch.

Unlike the previous microcompression experiments [82], the load function we adopted here is composed of multiple 'loading-holding' cyclic tests, as shown in Figure 5.1(a). The experimental set-up came out of an inspiration gained from the recent findings of anelasticity in BMGs [37, 128, 150], which implies that yielding in BMGs may result from the percolation of local anelasticity events. If that was so, yielding might be triggered by a time-dependent process at an appropriate stress level. To facilitate data collection, the holding load was programmed to start from ~80% of the estimated quasi-static yielding load, and then increased by ~5% per cycle. It should be noted that the loading rate was varied from 5×10^{2} μN/s to 1×10^{5} μN/s in an effort to assess the possible loading-rate effect on pop-in, as discussed in Ref. [151]; while both the holding and unloading time were set at ~2s, which suffice to relax anelastic deformation in the micropillars according to the previous findings [37]. As such, the remaining deformation during the holding time, if there were still any, should result from the local plasticity events in the micropillars.

5.3 Results and Discussions

Figure 5.1(a) shows a whole time-displacement curve corresponding to the load spectrum designed. As seen, the micropillar deforms initially in an apparent elastic manner, which is validated by the full recovery of the micropillar deformation after unloading. However, with the increasing load, yielding finally occurs, causing displacement burst or pop-in. Within our expectation, these pop-in events took place mainly during the holding periods, as clearly seen in Figures 5.1(b)-(d). After the finish of the test, it was found that the number of pop-in was in good agreement with that of the SBs observed on the micropillar (see Figure 5.2). These experimental observations indicate that each pop-in event corresponds to one SB operation in the micropillar. Furthermore, it is worth pointing out that the loading rate was found to play little role in determining the size of the pop-in occurring during holding, which validates our experiments as a size-effect study in which the possible rate effect has been ruled out.

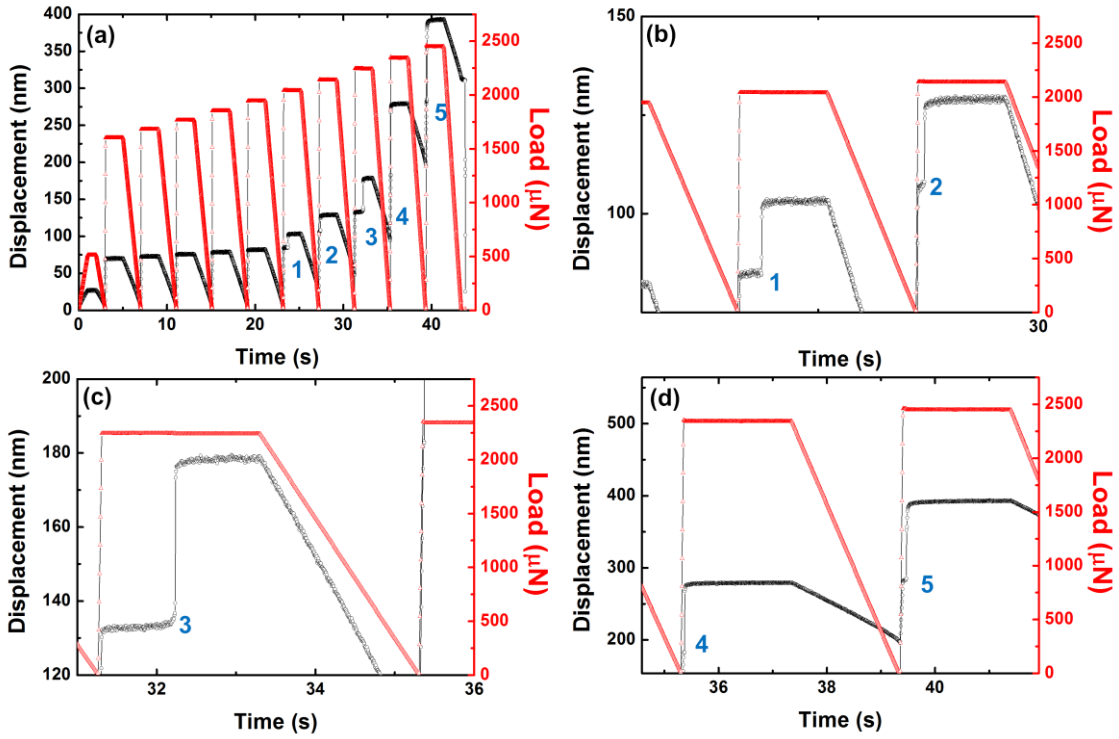

Figure 5.1. (a) The overall time-displacement displacement curve (black) displaying five pop-in events triggered at five consecutive holding periods (as indicated by the numbers) and the corresponding load spectrum programmed for the microcompression experiment; (b) to (d): the enlarged views of the five pop-in events.

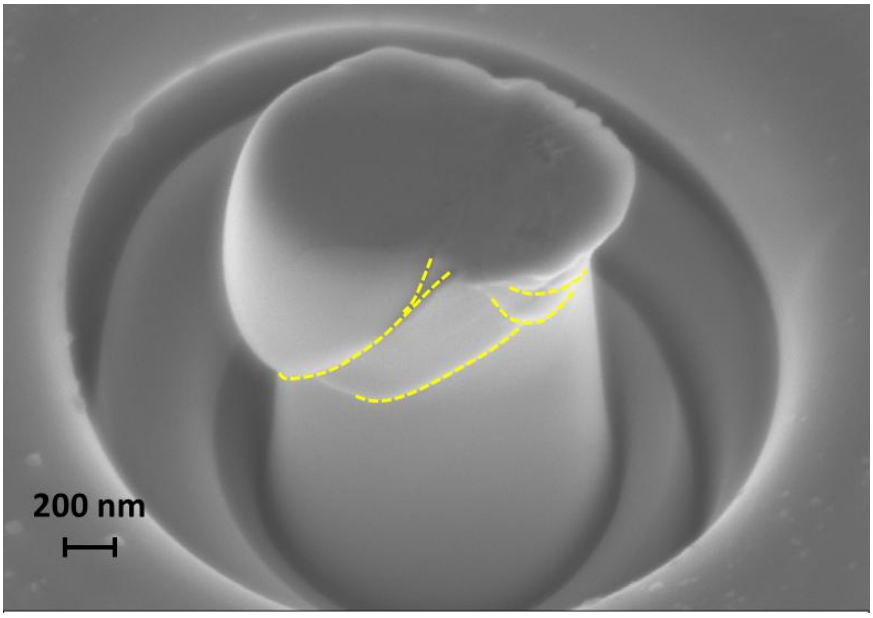

Figure 5.2. Compressed micropillar corresponding to above figure, five shear bands can be observed on the surface of the micropillar.

As a highlight, Figure 5.3(a) presents the details of the load and displacement versus time data, which characterize the pop-in event occurring during holding. Similar to the previous observations [83, 84], the SB seemingly experienced four stages of propagation, i.e. acceleration, sliding, deceleration and final arrest in the deformed micropillar. However, attention should be drawn to the well-maintained load constancy. Even at the instant of pop-in, the applied load only drops by ~5 μN, which is negligibly small and only counts up to ~ 0.2% of the programmed holding load. Following the method of Song et al. [83], the displacement rate, $\dot{h}$, which corresponds to the stage of viscous gliding as shown in Figure 5.3(b), was used to calculate the SB speed, *V*, for a given displacement jump Δh. Assuming the shear angle $\theta \sim 45^0$ (Fig. 2(c)) one can obtain the SB speed and the

corresponding shear offset s as $V = \dot{h} / \cos\theta$ and $s = \Delta h / \cos\theta$, respectively. Figure 5.4 presents the results of the SB speed so obtained as a function of s from different BMGs. Regardless of their chemical compositions, the measured SB speeds clearly exhibit a 'size' effect, i.e., the larger is the shear offset the higher is the SB speed, and seemingly follow a same trend that can be fitted by a power law.

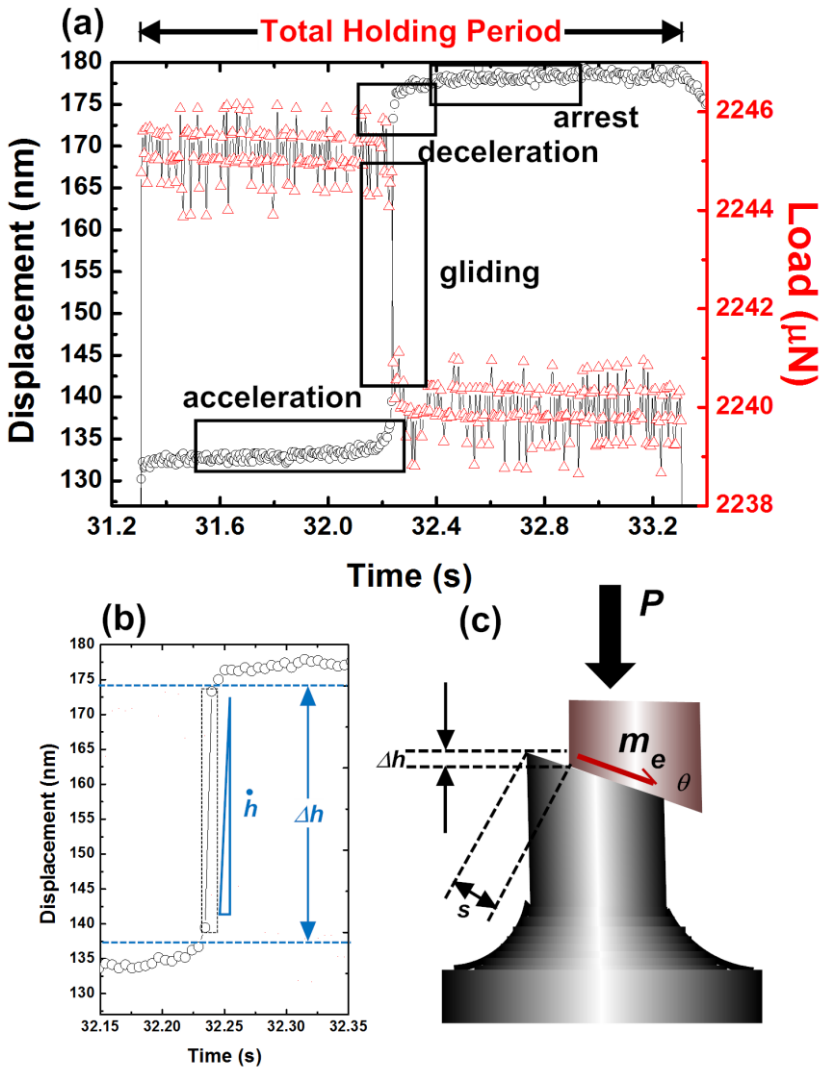

Figure 5.3. (a) The enlarged view of the discontinuities in the collected mechanical signals featuring a delayed pop-in event triggered in the holding period; (b) the portion of the time-displacement curve used to measure the displacement jump *h* and the corresponding characteristic displacement speed, $\dot{h}$, for the pop-in event; and (c) the sketch illustrating that the displacement-jump forms as the upper part of the micropillar glides along the inclined shear plane with the lower part of the micropillar remaining rest.

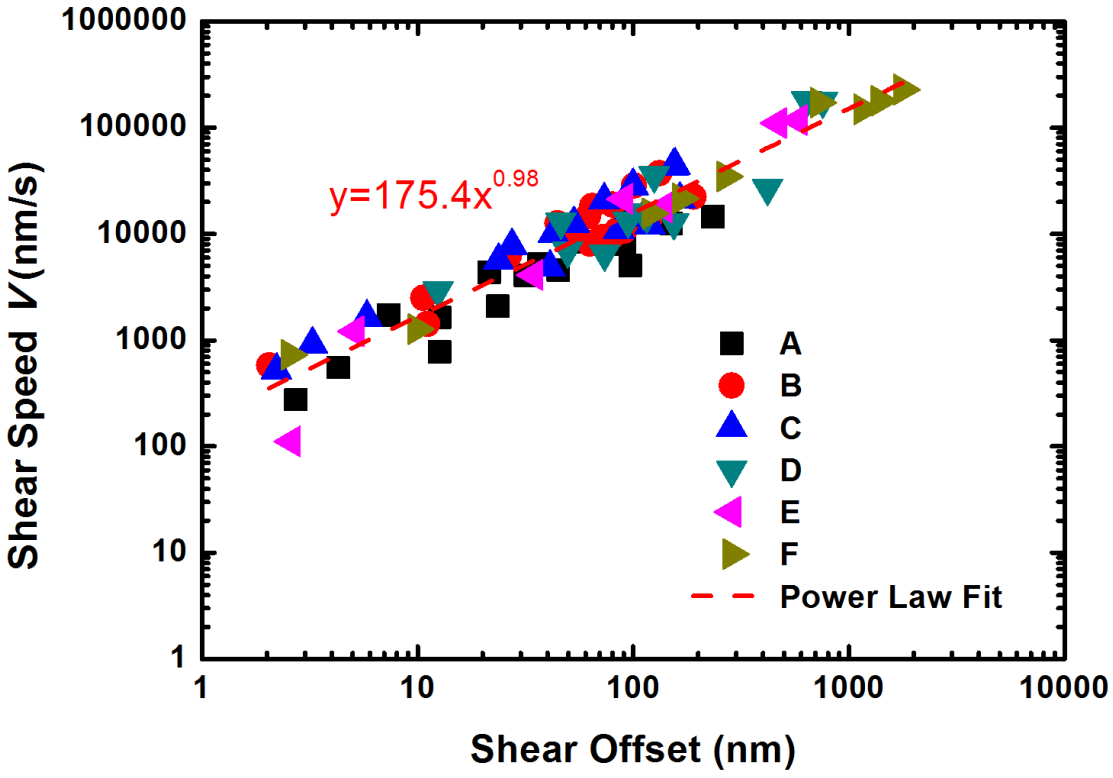

Figure 5.4. The double logarithmic plot of the measured shear speed versus shear offset for six types of BMGs with A= $Zr_{55}Pd_{10}Cu_{20}Ni_5Al_{10}$, B = $Cu_{46.25}Zr_{44.25}Al_{7.5}Er_2$, C=$Ti_{40}Zr_{25}Ni_3Cu_{12}Be_{20}$, D=$Zr_{55}Cu_{28}Ni_5Al_{10}Nb_2$, E = $(Fe_{44.3}Cr_5Co_5Mo_{12.8}Mn_{11.2}B_{5.9})_{98.5}Y_{1.5}$, and F= $Mg_{58}Cu_{31}Nd_5Y_6$.

To rationalize the observed size effect, let us turn to the kinetics of shear-banding in BMGs. At any instant of SB propagation, the energy balance should be maintained irrespective of the BMG's chemical composition, which can be expressed in a rate form as $\dot{W} = \dot{U}_e + \dot{K} + \dot{D}$, where W, U_e, K and D denote the work done by an external agent, the elastic energy storage, the kinetic energy, and the plastic energy dissipation, respectively; and the over-dot represents the time derivative of a physical quantity. For our microcompression experiments, in which the shear band propagates at a holding load,

it can be deduced that $\dot{W} = P\dot{h} = \tau_0 A_s V_s$, where τ_0 is the initial shear stress, V_s the instantaneous shear speed, and A_s the area of the shear plane; $K = \frac{1}{2} m_e V_s^{\,2}$, where m_e is the effective mass of the micropillar moving along with the shear band; and $D = A_s \int \tau(t) V_s dt$, where $\tau(t)$ denotes the instantaneous residual shear strength remaining on the shear plane. Note that, as the majority of the maximum shear offset measured is less than 10% of the corresponding pillar's diameter, the reduction in the area of the shear plane due to the shear-band propagation is neglected here for simplicity. Combining the above equations, one can then derive the following formula for the instantaneous shear speed V_s :

$$V_s(t) = \frac{A_s}{m_e} \left\{ \int_0^t [\tau_0 - \tau(t)] dt - \frac{1}{A_s} \int_0^t \frac{dU_e}{ds} dt \right\} \tag{5.1}$$

As will be seen in the later text, Equation 5.1 provides a theoretic framework that enables an explanation of the size effect on the measured shear speeds.

Based on the prior work [79, 152], it is known that BMGs experience initial shear softening and subsequent recovery (hardening) in a shear-banding event, which could be related to the acceleration, deceleration and ultimate arrest of the corresponding shear band, as demonstrated in Figure 5.3(a). Theoretically, such a physical picture of shear-banding dynamics can be inferred from Equation 5.1. When a shear band is in action, shear softening initially dominates the material behavior. Consequently, the instantaneous shear strength $\tau(t)$ reduces from τ_0, which is accompanied by the release of the elastic

energy stored in the vicinity of the shear band ($dU_e/ds < 0$) and leads to an ever increasing shear speed. However, at the later stage of shear banding when hardening or material recovery overwhelms shear softening, the instantaneous shear strength bounces back with the recovery of the elastic energy storage nearby ($dU_e/ds > 0$). In such a case, the shear band propagates with a diminishing speed until the full stop. To derive the maximum shear speed, one needs to solve $\dot{V}_s(t) = 0$ for the critical time, t_c, at which the shear band attains its full speed $V=V_s(t_c)$. Back to the experiments, the shear speed measured from the stage viscous gliding represents an experimentally accessible value that approximates $V_s(t_c)$, and can be written as:

$$V = V_s(t_c) = \frac{A_s}{m_e}\left\{\int_0^{t_c}[\tau_0 - \tau(t)]dt - \frac{1}{A_s}\int_0^{t_c}\frac{dU_e}{ds}dt\right\} \tag{5.2}$$

Up to the moment, we haven't explicitly elucidated the connection of Equation 5.2 with the size effect yet. To achieve this end, we substitute the shear displacement, s for the time, t, as the integral variable in Equation 5.2. The differential chain rule gives $dt = (dt/ds)ds = ds/V_s$. Making the substitution $t = t(s)$. Equation 5.2 can be cast into the following form:

$$V = \frac{A_s}{m_e}\left\{\int_0^{s_c}\frac{[\tau_0 - \tau(s)]}{V_s}ds - \frac{1}{A_s}\int_0^{s_c}\frac{dU_e}{ds}\frac{ds}{V_s}\right\} \tag{5.3}$$

Applying the mean value theorem:

$$\int_0^{s_c} \frac{[\tau_0 - \tau(s)]}{V_s} ds = \frac{f_2}{V} \int_0^{s_c} [\tau_0 - \tau(s)] ds \tag{5.4}$$

$$\int_0^{s_c} \frac{dU_e}{ds} \frac{ds}{V_s} = \frac{f_2}{V} \int_0^{s_c} \frac{dU_e}{ds} ds = -\frac{f_1}{V} \Delta U_e \tag{5.5}$$

where f_1 and f_2 are two constants depending on the functional form of the shear-banding constitutive law, and $\Delta U_e = U_e(s=0) - U_e(s=s_c)$. Substituting Equation 5.4 and 5.5 into Equation 5.3 gives:

$$V = \sqrt{\frac{A_s f_2}{m_e} \int_0^{s_c} [\tau_0 - \tau(s)] ds + \frac{f_1}{m_e} \Delta U_e} \tag{5.6}$$

Assuming $m_e = \rho\Omega$, where ρ is the density of the BMG and Ω is the effective sample volume, one can then obtain:

$$V = \sqrt{\frac{f_2}{\rho} \left(\int_0^{s_c} [\tau_0 - \tau(s)] ds A_s \Big/ \Omega \right) + \frac{f_1}{\rho} \left(\frac{\Delta U_e}{\Omega} \right)} \tag{5.7}$$

Taking $C_1 = f_1/\rho$, $C_2 = f_2/\rho$, $\Delta\Gamma = \int_0^{s_c} [\tau_0 - \tau(s)] ds A_s \Big/ \Omega$, and $\Delta u_e = \Delta U_e / \Omega$, Equation 5.7 is thus simplified to:

$$V = \sqrt{C_1 \Delta u_e + C_2 \Delta\Gamma} \tag{5.8}$$

In doing so, a simple equation relating the maximum shear speed, V, to the normalized energy variables may be derived, where C_1 and C_2 are two material dependent constants;

Δu_e is the volumetric density of the elastic energy released from the beginning of shear banding up to the time t_c; and $\Delta\Gamma$ is defined as a normalized complementary energy dissipation and proportional to $\int_0^{s_c}[\tau_0 - \tau(s)]ds$ with s_c denoting the shear displacement at t_c. Given the relation of V with the energy variables, it becomes natural of the size effect on the shear speed because of the known size dependence of the elastic energy release, Δu_e, that has been identified for BMGs, i.e. the larger is a shear offset or a sample size the more is the normalized elastic energy released upon shear banding. The cause of the size effect on Δu_e has been discussed thoroughly in the literature [76, 79, 80, 153] and can be generally ascribed to the dimensional misfit between the three-dimensional spring-back elastic energy release and two-dimensional plastic energy dissipation in BMGs. Apart from that, the second term on the right side of Equation 5.8 may also bring about a size effect. At constant external loading, $\Delta\Gamma$ increases with s_c and thus shear offset, leading to a size effect on V. However, in conventional tests with load serrations, the applied load drops with $\tau(t)$, nullifying the effect of $\Delta\Gamma$. As such, the size effect on the shear speed is completely due to the normalized elastic energy release.

In addition, in macroscopic compression test we can also find that strain burst size increases with the decrease of sliding time [81], imply shear band speed increases with the increase of shear offset (burst size) when many shear bands take place, this further illustrates that size-affected shear band speed exists during macroscopic deformation process with multiple shear band operation.

5.5 Conclusions

In summary, the dependence of the SB speed on the shear offset in BMGs is uncovered in this study with a general analytic framework provided for explanation. It is worth pointing out that this emerging size effect conforms to many other size-effect phenomena already found for BMGs, such as the sample size effect on malleability [76, 79], shear offsets [154] and thermal profile around a SB [80]. Furthermore, our current work also shows that yielding in BMGs could be triggered by delayed actions. This interesting phenomenon of delayed yielding could have important implications for deepening our knowledge of micro-scale plasticity in BMGs and hence warrants further investigations.

Chapter 6 Conclusions and Future Research Recommendations

6.1 Conclusions

This thesis investigated the cooling rate effect on quasi-static and dynamic mechanical properties of the $Zr_{55}Pd_{10}Cu_{20}Ni_5Al_{10}$ MGs. The quasi-static and dynamic mechanical properties were reflections of amorphous structure. After the structural study through the static and dynamic mean, yielding and shear banding phenomenon were explored. Based on the experimental results and theoretical analysis, following conclusions were drawn:

(1) Cooling rate has a negligible influence on the quasi-static properties, which including Young's modulus and hardness, of the $Zr_{55}Pd_{10}Cu_{20}Ni_5Al_{10}$ metallic glass. The measured reduction in the Young's moduli of the ribbon samples relative to those of the bulk samples utilizing nanoindentation has been proved simply caused by the sample thickness effect. After eliminating such a sample geometry effect, the cooling-rate independent mechanical properties were revealed.

(2) Theoretical framework based on the energy barrier concept was proposed. The theoretical analysis clearly show that the stress-induced reversible local structural transition in MGs is equivalent to a Kelvin-type anelastic deformation process, and that the viscoelastic properties of MGs obtained from the Kelvin model are closely related to intrinsic features characterizing their basic atomic-scale structural units, composed of FVZs and their surrounding elastic shell. Using this theoretical model, dynamic test results of bulk and ribbon MGs micropillars were analyzed, no discernable difference in effective modulus and viscosity can be revealed, indicating that similar content of dense packed cluster and FVZs in the bulk and ribbon metallic glass despite the cooling rated difference of about four orders of magnitude.

(3) As the reflections of shear band operation in microcompression, pop-ins with different size were detected, calculated speed of the shear band increase with the increase of the resultant shear offset. Utilizing an energy balance model, the speed of shear band as a function of shear offset was qualitatively analyzed. This emerging size effect conforms to many other size-effect phenomena already found for BMGs.

6.2 Future Research Recommendations

Despite the encouraging results obtained from this work, there are some points call for future investigations. Firstly, my thesis only addressed the micro mechanical behaviors of MGs at room temperature due to the instrumental limitations. While at higher temperature, some unique properties can be disclosed, more information of atomic

structural state of the MGs can be revealed. Secondly, shear band arresting mechanism after shear band gliding worth further investigation. It is widely accepted that localized shear band is the intrinsic plastic deformation features of BMGs, since shear banding cannot be avoided at room temperature for most BMGs, the arresting of SBs might be a promising method to enhance the mechanical performance of BMGs. Thirdly, the diameters of micropillars used in my thesis are around 1 μm, reduce this dimension to nanoscale, size effect can be investigated to reveal the inhomogeneous to homogeneous deformation transition in MGs. Apart from the above three points, there still are many fascinating properties and mechanism of MGs need to be addressed in further.

APPENDIX

Micro-mechanical Characterization of Casting Induced Inhomogeneity in an High Entropy Alloy

1 Introduction

High entropy alloys (HEAs) provide a novel alloy concept that significantly expands the scope of the traditional alloy design [155-157]. HEAs typically consist of at least five principle metallic elements in near-equimolar ratios and they often form a single solid solution structure, instead of many intermetallic compounds as expected from general physical metallurgy principles. HEAs show a great potential for engineering applications due to their high hardness, wear resistance, high temperature softening resistance and oxidation resistance [156, 158]. The commonly used alloying elements include FCC (face-centered cubic)-type Cu, Al, Ni, BCC (body-centered cubic)-type Fe, Cr, Mo, V and HCP (hexagonal close packed)-type Ti, Co [159-164]. Over the years substantial efforts have been devoted to the development of new HEA systems with improved mechanical and functional properties. However, few studies were carried out to investigate the mechanical inhomogeneity of these HEAs even though inhomogeneity is a common issue in the cast structure for crystalline materials and the existing experimental observations have clearly revealed the dendritic structure and compositional segregation in various HEA systems [160, 165].

$Al_xCoCrCuFeNi$ (in atomic proportion) system is a widely studied HEA system and the phase constitution in the as-cast material can be well adjusted by controlling the Al addition [160]. When $x \leq 0.5$, only one single FCC solid solution phase is observed [160]; BCC solid solution phase starts to appear at $x=0.8$ and at $x>2.3$ a single BCC phase is obtained although some minor phases (not detectable via conventional X-ray diffraction technique) do exist [160]. The mechanism behind the addition of FCC-type Al causing the transformation between FCC and BCC phases is still unclear, although presumably this can be rationalized as the alloying of the larger Al atoms lowers the atomic packing efficiency [31]. Previous reports suggest that the lattice parameters for both FCC and BCC phases increase with increasing x but significant increase of hardness is seen only at $x>1.0$ [160, 166]. The formation of BCC phase will enhance the strength of the originally purely FCC solid solution, but it also causes the embrittlement issue at ambient temperature [167]. Naturally, it is of interest to study the mechanical behavior of $Al_{0.8}CoCrCuFeNi$ (BCC phase just starts to appear) from the structure-property correlation perspective. In addition, a secondary FCC phase has been detected in the as-cast $Al_{1.0}CoCrCuFeNi$ [165, 168] by X-ray diffraction, but not yet in the $Al_{0.8}CoCrCuFeNi$. In this work we used the neutron diffraction technique to successfully detect the secondary FCC phase. The existence of three phases (two FCC phases and one BCC phase) can be well related to the three distinctive regions observed in the microstructure. We also did careful micro-compression tests to characterize these three regions to obtain their individual mechanical properties. To the best of our knowledge, this is the first time a micro-compression test is used for HEAs.

2 Experimental Procedures

The target alloy used in this work has a nominal composition $Al_{0.8}CoCrCuFeNi$ (in atomic proportion). The alloys were prepared by arc-melting a mixture of the constituent elements with purity better than 99.9% in a Ti-gettered high purified argon atmosphere. Repeated melting was carried out at least five times to improve the chemical homogeneity of the alloy. The molten alloy was drop-cast into the copper mold with diameter of 10 mm. The phase constitution of the alloy was examined by both the X-ray diffraction (XRD) using Co radiation (Bruker AXS D8 Discover) and the neutron diffraction using the VULCAN diffractometer (Spallation Neutron Source, Oak Ridge National Laboratory, USA [169]). Because neutrons are highly penetrating, the neutron diffraction measurements are representative of the bulk, rather than from the surface. As a state-of-the-art engineering diffractometer, VULCAN can be flexibly configured in either high-intensity or high-resolution mode [170, 171]. The present measurements were made in the high-resolution mode, in which a $\Delta d/d \sim 0.2\%$ resolutions is maintained over a wide range of *d*-spacing. This allowed easy identification of the multiple phases in the sample. The microstructure of the alloy was characterized using the Leo 1530 FEG scanning electron microscope (SEM) operated at 5 kV equipped with energy dispersive spectrometer (EDS). For the microstructure observation, the sample surface was sequentially polished down to 0.1 μm grit alumina suspension finish and then etched with the aqua regia solution. To investigate the micro-mechanical behavior, micro-pillars with top diameter of ~0.8 μm and aspect ratios ranging from 2:1 to 5:1 were fabricated using a Quanta 200 3D dual-beam SEM/focused ion beam (FIB) system (FEI Company, Hillsboro, OR, USA).

Following the well established sequential-milling approach [111, 172], the micro-pillars were prepared with great care particularly in the inter-dendritic regions, to ensure that the as-cut micro-pillars exclusively came from the target regions (see section 3.2). The micro-compression tests for the micro-pillars were subsequently carried out using a low-load Triboindenter™ Nanoindentation syetem (Hysitron Inc, Minneapolis, MN, USA) equipped with a 10 μm flat-end diamond punch at the load-controlled mode. To ensure the reproducibility of the micro-compression data, at least three micro-pillars were fabricated and compressed from each characteristic region. Vickers hardness was also measured by applying a load of 1 kg for 10 s using the Future-Tech microhardness tester.

3 Results and Discussions

3.1 Phase Identification

Figure 1 shows the XRD pattern of the as-cast $Al_{0.8}CoCrCuFeNi$. It is seen that the alloy has a simple solid solution structure where one FCC and one BCC phase were identified. Judging from the relative intensity, the main phase of the alloy is FCC. This is in agreement with the previous results reported by Tong et al. [160]. It should be mentioned here that due to the dendritic structure (see below), the X-ray diffraction intensities present texture feature and hence some characteristic peaks are abnormally weak, although the intensity decrease could also be caused by the highly distorted atomic planes in the solid solutions [173]. To ascertain that the BCC phase also exists in the bulk, the alloy was examined using neutron diffraction and the pattern is shown in Fig.2. Interestingly, apart from one FCC and one BCC phase identified using conventional XRD, a secondary FCC phase was also detected. To differentiate these two FCC phases, they

are termed as FCC1 and FCC2 hereinafter. The FCC2 phase is the minor phase judging from its volume fraction. Based on the neutron diffraction results, the lattice parameters for the FCC1, FCC2 and BCC phases are estimated to be 3.603, 3.631 and 2.874 Å, respectively. It is worthy pointing out that FCC1 and FCC2 phases were also identified in the as-cast $Al_{0.5}$CoCrCuFeNi alloy using the neutron diffraction (results not given here), and the lattice parameters for the FCC1 and FCC2 (3.596 and 3.628 Å, respectively) are almost the same as those in $Al_{0.8}$CoCrCuFeNi. In addition, the lattice parameters for the FCC1, FCC2 and BCC phases in $Al_{0.8}$CoCrCuFeNi measured in this work are very close to those of the corresponding phases in $Al_{1.0}$CoCrCuFeNi (3.59, 3.62 and 2.87 Å, respectively) reported by Singh et al. using XRD [174]. It is noted here that our measurement of the lattice parameters together with those from Singh et al. are different to the results reported by Tong et al. [160] for the same alloy compositions, in that our measured lattice parameters are less sensitive to the Al composition. This could most possibly be due to the fact that Tong et al. only identified one FCC phase in their XRD analyses, and the hidden FCC peaks would cause the inaccurate peak fitting from which the lattice parameters were calculated. The lattice parameters reflect the lattice distortion information and our results can account for the hardness variation as a function of Al addition better: from x=0.5 to 0.8, the alloying of Al causes the partial transformation from FCC to BCC phase while the FCC lattice remains nearly invariant; at x=0.8, the main phase is still FCC and the amount of BCC phase is insufficient to cause significant strengthening (the Vickers hardness using 1 kg load for $Al_{0.5}$CoCrCuFeNi and $Al_{0.8}$CoCrCuFeNi are 258 and 280, respectively); however, when x reaches 1.0, the main

phase becomes BCC [165], and the large amount of harder BCC phases causes the hardness to increase to 531.

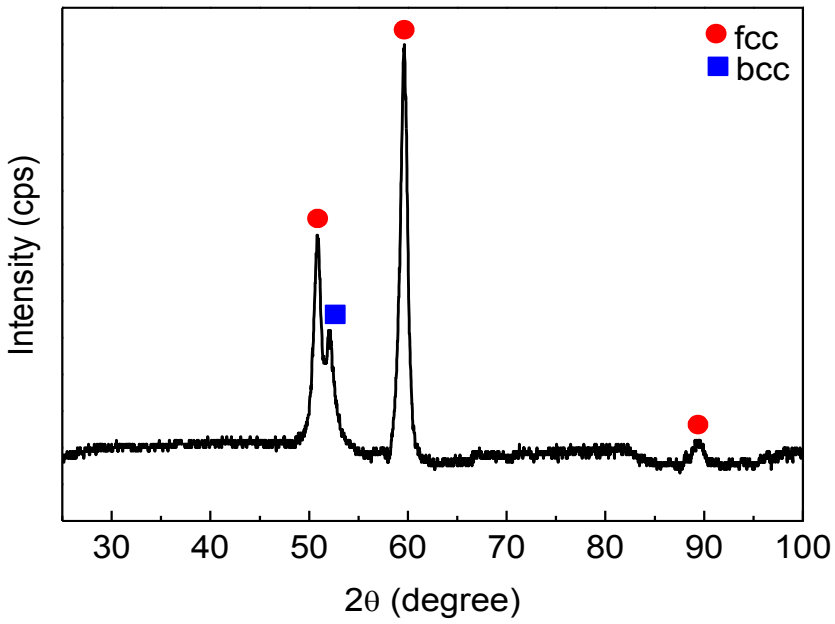

Figure 1 XRD pattern of the as-cast $Al_{0.8}CoCrCuFeNi$ alloy

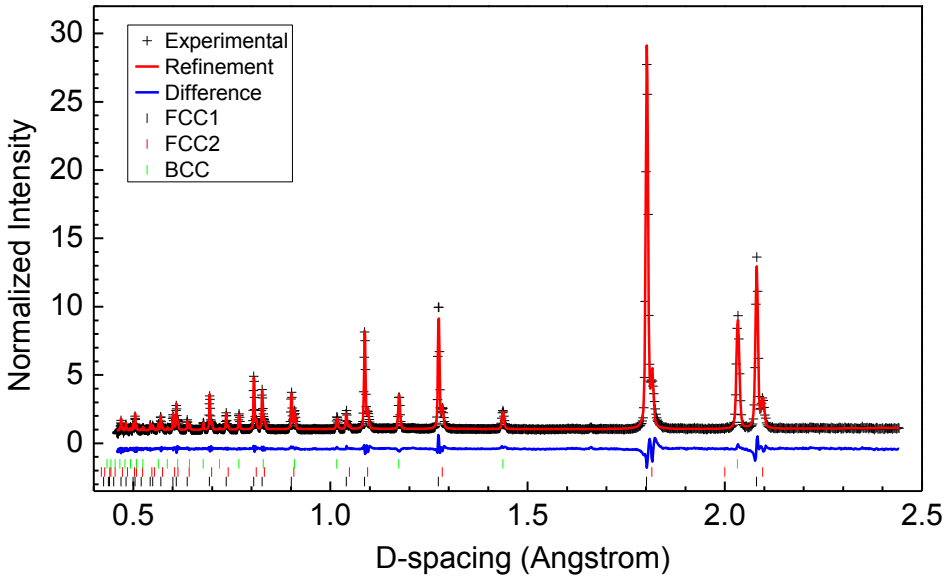

Figure 2 Neutron diffraction pattern of the as-cast $Al_{0.8}$CoCrCuFeNi alloy

3.2 Microstructure Characterization

Figure 3 shows the microstructure of the as-cast alloy. Dendritic and inter-dendritic structures typical to cast HEAs [160] are clearly observed. According to Tong et al. [160], there are *only two* distinctive regions in the microstructure and the dendritic regions have a FCC structure, while the inter-dendritic regions have a mixed FCC+BCC structure. However, our high resolution SEM observation given in Fig.3 apparently shows the existence of *three* distinctive regions: dendritic region (*A*) and two inter-dendritic regions (*B* and *C*). The dendritic region *A* has a relatively homogeneous contrast, which is consistent to that reported by Tong et al. [160], and corresponding to the single FCC structure. In contrast, Regions *B* and *C* appear to contain more than one phase.

Particularly, Region *C* has a spinodally decomposed netlike feature. Recalling the phase identification results we obtained from Fig.2, together with the EDS analysis results give in Table 1 (see below), it is reasonable to infer that Region *C* shall be composed of two spinodally decomposed FCC phases, while Region *B* shall have a mixed FCC+BCC structure. Based on these findings, it can be envisaged that the formation of the BCC phase shall result from the decomposition of the inter-dendritic structure during the cooling process. Since it is generally perceived that the BCC phase is a harder phase compared with the FCC phase, Region *B* would have a higher hardness (or strength) than that Region *A*. This is actually supported by the micro-compression tests discussed below. From the neutron diffraction and composition analyses we already know that the FCC1 is the main phase, we can further infer that Region *A* has the FCC1 structure, Region *B* has the FCC1+BCC structure and Region *C* has the FCC1+FCC2 structure.

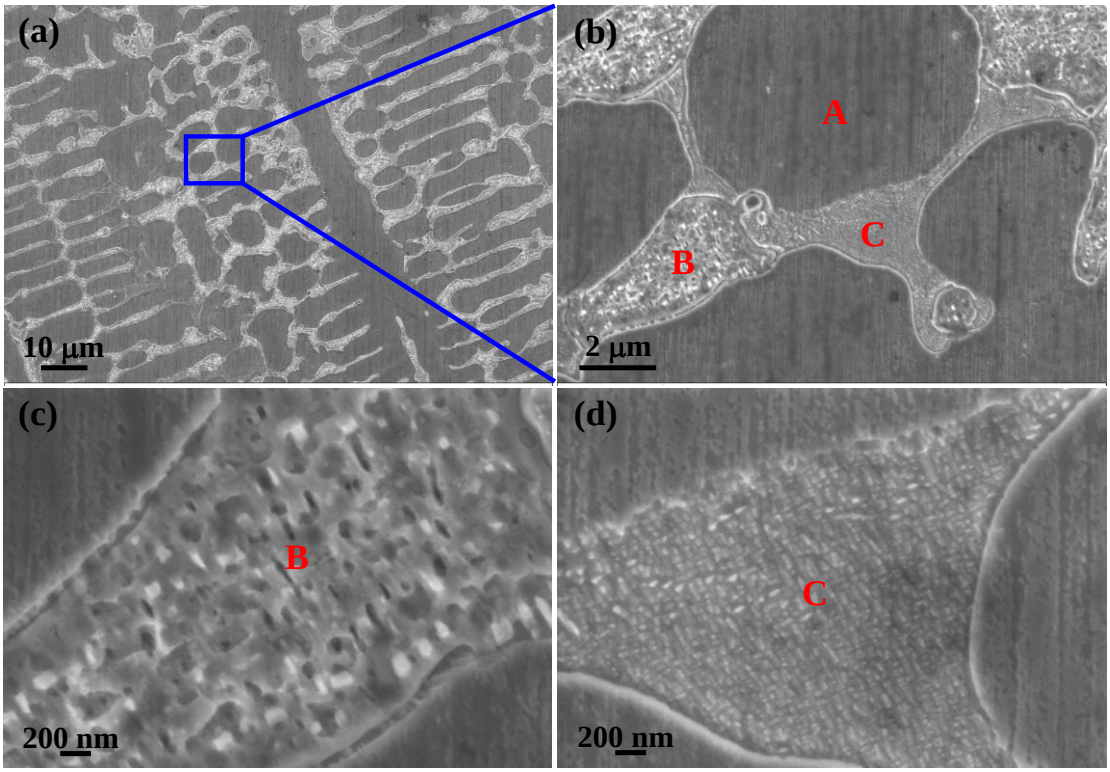

Figure 3 SEM images of the as-cast $Al_{0.8}CoCrCuFeNi$ alloy: (a) low magnification image; (b) magnified image of the indicated zone in (a) showing the three distinctive regions *A*, *B* and *C*. (c) and (d) are magnified images for Regions *B* and *C*, respectively.

The average chemical compositions for the three regions from multiple-point EDS analysis are listed in Table 1. It can be seen that these three regions have clearly different chemical compositions: Region *A* is enriched in Co, Cr and Fe while deficient in Al and Ni and Cu; Region *B* is enriched in Al and Ni while the other elements are deficient; Region *C* is significantly enriched in Cu while deficient in Co, Cr and Fe. Ni tends to accompany with Al in the inter-dendritic regions due to the large negative mixing enthalpy (ΔH_{mix}) between them [175]. This possibly results in the formation of NiAl-type (B2) phase in Region *B* [160, 165]. Cu has the tendency to segregate from other alloying

elements because apart from Al it has positive ΔH_{mix} with other elements [175]. The formation of the Cu-rich zone in Region *C* relative to the Cu-deplete zone in Region *A* also supports the spinodal decomposition occurred in Region *C*.

Table 1 Chemical compositions of the as-cast $Al_{0.8}CoCrCuFeNi$ alloy

Element (at. %)	Structure	Al	Co	Cr	Cu	Fe	Ni
Nominal		13.79	17.24	17.24	17.24	17.24	17.24
Region A	FCC1	10.39	21.26	22.21	8.56	22.12	15.47
Region B	FCC1+BCC	22.82	13.97	13.54	15.76	12.52	21.39
Region C	FCC1+FCC2	14.20	6.62	5.16	53.83	6.11	14.08

3.3 Micro-compression Tests

Now that we have identified the phase constitution for the three distinctive regions, we can go further to characterize their individual mechanical properties using the well-established micro-compression technique [88, 176]. Micro-pillars were machined from the three regions using the FIB technique and then compressed using the flat-end diamond punch under the load-controlled condition. The typical micro-pillars before and after the micro-compression tests are given in Fig. 4, and the representative nominal

stress-strain curves are plotted in Fig. 5. Here the stress is taken as the applied load divided by the initial top area of the pillar, and the strain is taken as the indenter displacement divided by the initial height of the pillar. As shown in Fig. 5, all specimens exhibit a linear response upon loading before the yielding point, i.e. the first observable strain burst appears [177]. The extracted yield strengths for the three regions are listed in Table 2. The micro-pillars cut from the inter-dendritic region *B* has the highest yield strength of ~958 MPa, which is about 20% higher than that of the dendritic region *A* (~764 MPa). The much higher strength of Region *B* shall most probably come from the precipitation of the BCC phase in this region. Region *C* has a slightly higher yield strength (~825 MPa) than that of Region *A*, in agreement with our previous assumption that this region has a mixed two-FCC-phase structure resulting from the spinodal decomposition. It is noted here that the single phase Region *A* has a high yield strength of ~764 MPa, which is much higher than the strength (UTS, ultimate tensile strength) of any constituent metal element (Al: 47, Co: 255, Cr: 483, Cu: 220, Fe:289 and Ni: 407 MPa [178]).

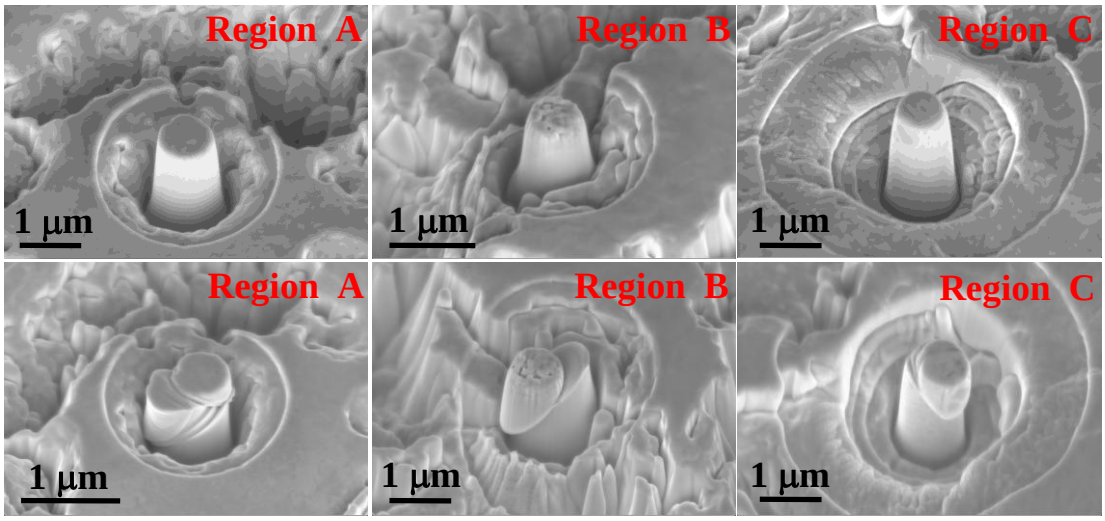

Figure 4 SEM images of the micro-pillars before (a, c, e) and after (b, d, f) the micro-compression tests. (a) and (b), (c) and (d), and (e) and (f) correspond to Regions *A*, *B* and *C*, respectively.

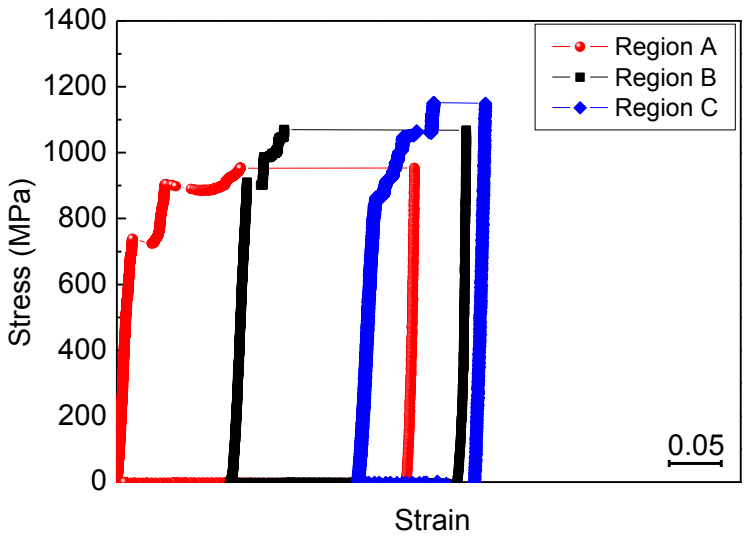

Figure 5 Stress-strain curves for the micro-pillars fabricated in the three different regions as shown in Fig.3.

Table 2 Yield strength of the micro-pillars in the three different regions

Micro-pillars	Yield Strength (MPa)
Region A	763.9 ±46.8
Region B	957.5 ±80.1
Region C	824.6 ±59.8

After yielding, the pillars deform plastically via the emission of sporadic strain burst under the load-controlled condition, separated by elastic like deformation segments. Similar phenomena have also been observed from the micro-compression of a variety of single crystal metals [179, 180]. From the nominal stress-strain curves, it is noticed that smaller strain bursts tend to occur for Regions *B* and *C* compared to those in Region *A*. This could be attributed to the blocking and storage of dislocations by the phase boundaries in the two-phase regions, *B* and *C*, and the interaction between the high density of dislocations and the phase boundaries can account for the much less jumpy deformation behavior [181].

4 Conclusions

Microstructural features and micro-mechanical behavior for individual phase in a cast $Al_{0.8}$CoCrCuFeNi alloy have been determined using high resolution scanning electron

microscopy, together with the delicate FIB assisted micro-compression tests. Both compositional and micro-mechanical analyses revealed the existence of two spinodally decomposed FCC phases plus one BCC phase, in agreement with the phase identification results from the neutron diffraction. The BCC phase has clearly higher yield strength than the other two FCC phases. The understanding of the mechanical behavior of individual phase provides important input for the design of new HEAs with desirable mechanical properties.

REFERENCE

[1] A.L. Greer, E. Ma, Mrs Bulletin, 32 (2007) 611-615.

[2] W.H. Wang, C. Dong, C.H. Shek, Mater. Sci. Eng. R-Rep., 44 (2004) 45-89.

[3] W. Klement, R.H. Willens, P.O.L. Duwez, Nature, 187 (1960) 869-870.

[4] H.S. Chen, Acta Metallurgica, 22 (1974) 1505-1511.

[5] H.S. Chen, J.T. Krause, E. Coleman, J. Non-Cryst. Solids, 18 (1975) 157-171.

[6] A.J. Drehman, A.L. Greer, D. Turnbull, Appl. Phys. Lett., 41 (1982) 716-717.

[7] A. Inoue, T. Zhang, T. Masumoto, Mater. Trans. JIM, 30 (1989) 965-972.

[8] A. Inoue, T. Zhang, T. Masumoto, Mater. Trans. JIM, 31 (1990) 177-183.

[9] J.D. Bernal, Nature, 185 (1960) 68-70.

[10] P.H. Gaskell, Nature, 276 (1978) 484-485.

[11] D.B. Miracle, Nat Mater, 3 (2004) 697-702.

[12] H.W. Sheng, W.K. Luo, F.M. Alamgir, J.M. Bai, E. Ma, Nature, 439 (2006) 419-425.

[13] C.A. Schuh, T.C. Hufnagel, U. Ramamurty, Acta Mater., 55 (2007) 4067-4109.

[14] T.G. Nieh, C. Schuh, J. Wadsworth, Y. Li, Intermetallics, 10 (2002) 1177-1182.

[15] Z.F. Zhang, J. Eckert, L. Schultz, Acta Mater., 51 (2003) 1167-1179.

[16] M. Kusy, U. Kühn, A. Concustell, A. Gebert, J. Das, J. Eckert, L. Schultz, M.D. Baro, Intermetallics, 14 (2006) 982-986.

[17] D.E. Polk, D. Turnbull, Acta Metallurgica, 20 (1972) 493-&.

[18] F. Spaepen, Acta Metallurgica, 25 (1977) 407-415.

[19] A.S. Argon, Acta Metallurgica, 27 (1979) 47-58.

[20] M.W. Chen, Annual Review of Materials Research, 38 (2008) 445-469.

[21] A. Inoue, Y. Shinohara, Y. Yokoyama, T. Masumoto, Mater. Trans. JIM, 36 (1995) 1276-1281.

[22] B.S. Egami T, Underneath the Bragg Peaks, Structural Analysis of Complex Materials Elsevier; 2003, Oxford, 2003.

[23] Y.Q. Cheng, E. Ma, Prog. Mater. Sci., 56 (2011) 379-473.

[24] M.H. Cohen, D. Turnbull, Journal of Chemical Physics, 31 (1959) 1164-1169

[25] C.H. Bennett, P. Chaudhari, V. Moruzzi, P. Steinhardt, Philos. Mag. A-Phys. Condens. Matter Struct. Defect Mech. Prop., 40 (1979) 485-495.

[26] F.E. Luborsky, Amorphous metallic alloys Butterworths, London 1983.

[27] T. Egami, D. Srolovitz, Journal of Physics F-Metal Physics, 12 (1982) 2141-2163.

[28] X.J. Liu, Y. Xu, X. Hui, Z.P. Lu, F. Li, G.L. Chen, J. Lu, C.T. Liu, Phys. Rev. Lett., 105 (2010) 155501.

[29] H.W. Sheng, W.K. Luo, F.M. Alamgir, J.M. Bai, E. Ma, Atomic packing and short-to-medium-range order in metallic glasses, in: Nature, 2006, pp. 419-425.

[30] A. Inoue, B.L. Shen, C.T. Chang, Acta Mater., 52 (2004) 4093-4099.

[31] J.Q. Wang, W.H. Wang, H.B. Yu, H.Y. Bai, Appl. Phys. Lett., 94 (2009) 3.

[32] M. Vaillant, V. Keryvin, T. Rouxel, Y. Kawamura, Scripta Mater, 47 (2002) 19-23.

[33] Y. Cheng, E. Ma, Physical Review B, 80 (2009) 064104.

[34] V. Keryvin, T. Rouxel, M. Huger, L. Charleux, J Ceram Soc Jpn, 116 (2008) 851-854.

[35] D.J. Safarik, R.B. Schwarz, Acta Mater., 55 (2007) 5736-5746.

[36] A. Argon, Mechanisms of inelastic deformation in metallic glasses, in: J Phys Chem Solids, 1982, pp. 945-961.

[37] J.C. Ye, J. Lu, C.T. Liu, Q. Wang, Y. Yang, Nat. Mater., 9 (2010) 619-623.

[38] W. Dmowski, T. Iwashita, C.-P. Chuang, J. Almer, T. Egami, Phys. Rev. Lett., 105 (2010) 205502.

[39] M.L. Falk, J.S. Langer, Phys. Rev. E, 57 (1998) 7192-7205.

[40] A. Inoue, X.M. Wang, W. Zhang, Developments and applications of bulk metallic glasses, in: Reviews on Advanced Materials Science, 2008, pp. 1-9.

[41] W. Johnson, K. Samwer, Phys. Rev. Lett., 95 (2005) 195501.

[42] C.A. Schuh, A.C. Lund, Nature Mater., 2 (2003) 449-452.

[43] M.D. Demetriou, J.S. Harmon, M. Tao, G. Duan, K. Samwer, W.L. Johnson, Phys. Rev. Lett., 97 (2006) 4.

[44] W.L. Johnson, K. Samwer, Phys. Rev. Lett., 95 (2005) 4.

[45] A. Rehmet, K. Gunther-Schade, K. Ratzke, U. Geyer, F. Faupel, Physica Status Solidi a-Applications and Materials Science, 201 (2004) 467-470.

[46] A. Gupta, M.E. Jayaraj, J. Non-Cryst. Solids, 149 (1992) 275-281.

[47] S.N. Kane, N. Bhagat, A. Gupta, L.K. Varga, Journal of Magnetism and Magnetic Materials, 167 (1997) 241-244.

[48] J. Wang, P.D. Hodgson, J. Zhang, W. Yan, C. Yang, Journal of Materials Processing Technology, 209 (2009) 4601-4606.

[49] D.V. Louzguine-Luzgin, G. Xie, Q. Zhang, C. Suryanarayana, A. Inoue, Metall. Mater. Trans. A-Phys. Metall. Mater. Sci., 41A (2010) 1664-1669.

[50] M.D. Ediger, C.A. Angell, S.R. Nagel, J. Phys. Chem., 100 (1996) 13200-13212.

[51] R. Raghavan, P. Murali, U. Ramamurty, Metall. Mater. Trans. A-Phys. Metall. Mater. Sci., 39A (2008) 1573-1577.

[52] F. Xu, Y.L. Du, P. Gao, Z.D. Han, G. Chen, Mater. Lett., 61 (2007) 4875-4878.

[53] H.R. Wang, Y.L. Gao, X.D. Hui, Y. Chen, G.H. Min, Y.F. Ye, J. Alloy. Compd., 350 (2003) 178-183.

[54] Y.J. Huang, J. Shen, J.J.J. Chen, J.F. Sun, J. Alloy. Compd., 477 (2009) 920-924.

[55] Y. Liu, H. Bei, C.T. Liu, E.P. George, Appl. Phys. Lett., 90 (2007) 3.

[56] N. Chen, K.F. Yao, F. Ruan, Y.Q. Yang, Mater. Sci. Eng. A-Struct. Mater. Prop. Microstruct. Process., 473 (2008) 274-278.

[57] K.B. Kim, X.F. Zhang, S. Yi, M.H. Lee, J. Das, J. Eckert, Philos. Mag. Lett., 88 (2008) 75-81.

[58] E.S. Park, J.Y. Lee, D.H. Kim, A. Gebert, L. Schultz, J. Appl. Phys., 104 (2008) 10.

[59] E.S. Park, D.H. Kim, Intermetallics, 18 (2010) 1867-1871.

[60] J. Shen, Y.J. Huang, J.F. Sun, Journal of Materials Research, 22 (2007) 3067-3074.

[61] J. Zhang, S.J. Pang, T. Zhang, Science China-Physics Mechanics & Astronomy, 53 (2010) 415-418.

[62] Y.J. Huang, Y.L. Chiu, J. Shen, J.J.J. Chen, J.F. Sun, J. Alloy. Compd., 479 (2009) 121-128.

[63] Y.J. Huang, Y.L. Chiu, J. Shen, J.J.J. Chen, J.F. Sun, J. Non-Cryst. Solids, 356 (2010) 966-970.

[64] W.H. Jiang, F.X. Liu, Y.D. Wang, H.F. Zhang, H. Choo, P.K. Liaw, Materials Science and Engineering a-Structural Materials Properties Microstructure and Processing, 430 (2006) 350-354.

[65] X. Hu, S.C. Ng, Y.P. Feng, Y. Li, Phys. Rev. B, 64 (2001) 4.

[66] L.Q. Xing, J. Eckert, W. Loser, L. Schultz, Appl. Phys. Lett., 73 (1998) 2110-2112.

[67] B.C. Wei, W.H. Wang, G.S. Yu, W.H. Li, Y.F. Sun, Y.R. Wang, Effect of solidification process on magnetic properties of Nd-based bulk amorphous forming alloy, in: C.S. Kiminami, C. Bolfarini, W.J. BottaF (Eds.) Ismanam 2003: Metastable, Mechanically Alloyed and Nanocrystalline Materials, Trans Tech Publications Ltd, Stafa-Zurich, 2004, pp. 685-689.

[68] R. Kolano, N. Wojcik, W.W. Gawior, M. Kuzminski, IEEE Trans. Magn., 30 (1994) 1033-1035.

[69] Q. Bai, H. Xu, X.H. Tan, H. Man, S.J. Wu, P.P. Cai, J. Alloy. Compd., 473 (2009) 11-14.

[70] X.Z. Wang, Y. Li, J. Ding, L. Si, H.Z. Kong, J. Alloy. Compd., 290 (1999) 209-215.

[71] A.E. Berlev, O.P. Bobrov, V.A. Khonik, K. Csach, A. Jurikova, J. Miskuf, H. Neuhauser, M.Y. Yazvitsky, Phys. Rev. B, 68 (2003) 4.

[72] M.D. Demetriou, M.E. Launey, G. Garrett, J.P. Schramm, D.C. Hofmann, W.L. Johnson, R.O. Ritchie, Nat. Mater., 10 (2011) 123-128.

[73] C.T. Liu, M.F. Chisholm, M.K. Miller, Intermetallics, 10 (2002) 1105-1112.

[74] Z. Han, W.F. Wu, Y. Li, Y.J. Wei, H.J. Gao, Acta Mater., 57 (2009) 1367-1372.

[75] F.F. Wu, W. Zheng, S.D. Wu, Z.F. Zhang, J. Shen, International Journal of Plasticity, 27 (2011) 560-575.

[76] Y. Yang, J.C. Ye, J. Lu, P.K. Liaw, C.T. Liu, Appl. Phys. Lett., 96 (2010) 011905.

[77] H. Guo, P.F. Yan, Y.B. Wang, J. Tan, Z.F. Zhang, M.L. Sui, E. Ma, Nature Mater., 6 (2007) 735-739.

[78] C.A. Volkert, A. Donohue, F. Spaepen, J. Appl. Phys., 103 (2008) 083539.

[79] J.C. Ye, J. Lu, Y. Yang, P.K. Liaw, Acta Mater., 57 (2009) 6037-6046.

[80] Y.Q. Cheng, Z. Han, Y. Li, E. Ma, Phys. Rev. B, 80 (2009) 6.

[81] F.H. Dalla Torre, D. Klaumünzer, R. Maaß, J.F. Löffler, Acta Mater., 58 (2010) 3742-3750.

[82] H.M. Chen, J.C. Huang, S.X. Song, T.G. Nieh, J.S.C. Jang, Appl. Phys. Lett., 94 (2009) 3.

[83] S.X. Song, X.L. Wang, T.G. Nieh, Scripta Materialia, 62 (2010) 847-850.

[84] W.J. Wright, M.W. Samale, T.C. Hufnagel, M.M. LeBlanc, J.N. Florando, Acta Materialia, 57 (2009) 4639-4648.

[85] X.H. Lin, W.L. Johnson, Journal of Applied Physics, 78 (1995) 6514-6519.

[86] X. Gu, L.Q. Xing, T.C. Hufnagel, J. Non-Cryst. Solids, 311 (2002) 77-82.

[87] W.C. Oliver, G.M. Pharr, J. Mater. Res., 7 (1992) 1564-1583.

[88] M.D. Uchic, D.A. Dimiduk, Mater. Sci. Eng. A-Struct. Mater. Prop. Microstruct. Process., 400 (2005) 268-278.

[89] J. MacSleyne, M.D. Uchic, J.P. Simmons, M. De Graef, Acta Mater., 57 (2009) 6251-6267.

[90] H. Zhang, B.E. Schuster, Q. Wei, K.T. Ramesh, Scr. Mater., 54 (2006) 181-186.

[91] S. Reyntjens, R. Puers, J. Micromech. Microeng., 11 (2001) 287-300.

[92] A.R. Yavari, J.J. Lewandowski, J. Eckert, Mrs Bulletin, 32 (2007) 635-638.

[93] J.F. Loffler, Intermetallics, 11 (2003) 529-540.

[94] C. Fan, P.K. Liaw, C.T. Liu, Intermetallics, 17 (2009) 86-87.

[95] Y.Q. Cheng, A.J. Cao, H.W. Sheng, E. Ma, Acta Materialia, 56 (2008) 5263-5275.

[96] G. Kumar, T. Ohkubo, K. Hono, Journal of Materials Research, 24 (2009) 2353-2360.

[97] J.T. Wang, P.D. Hodgson, J.D. Zhang, W.Y. Yan, C.H. Yang, Journal of Materials Processing Technology, 209 (2009) 4601-4606.

[98] D.V. Louzguine-Luzgin, T. Saito, J. Saida, A. Inoue, Journal of Materials Research, 23 (2008) 515-522.

[99] L.Q. Xing, T.C. Hufnagel, J. Eckert, W. Loser, L. Schultz, Applied Physics Letters, 77 (2000) 1970-1972.

[100] Y. Liu, H. Bei, C.T. Liu, E.P. George, Applied Physics Letters, 90 (2007).

[101] X. Hu, S.C. Ng, Y.P. Feng, Y. Li, Physical Review B, 64 (2001).

[102] L.Y. Chen, A.D. Setyawan, H. Kato, A. Inoue, G.Q. Zhang, J. Saida, X.D. Wang, Q.P. Cao, J.Z. Jiang, Scripta Materialia, 59 (2008) 75-78.

[103] Y.H. Xiao, Y. Wu, Z.Y. Liu, H.H. Wu, Z.P. Lu, Science China-Physics Mechanics & Astronomy, 53 (2010) 394-398.

[104] Y.J. Huang, J. Shen, J.F. Sun, Applied Physics Letters, 90 (2007).

[105] Y.H. Liu, C.T. Liu, A. Gali, A. Inoue, M.W. Chen, Intermetallics, 18 (2010) 1455-1464.

[106] W.C. Oliver, G.M. Pharr, Journal of Materials Research, 7 (1992) 1564-1583.

[107] J.M. Antunes, J.V. Fernandes, N.A. Sakharova, M.C. Oliveira, L.F. Menezes, International Journal of Solids and Structures, 44 (2007) 8313-8334.

[108] B. Yang, C.T. Liu, T.G. Nieh, Appl. Phys. Lett., 88 (2006) 221911.

[109] L.A. Davis, Mechanical Behavior of Rapidly Solidified Materials, The Metallurgical Society, 1986.

[110] F. Zeng, Y. Gao, L. Li, D.M. Li, F. Pan, Journal of Alloys and Compounds, 389 (2005) 75-79.

[111] Y. Yang, J.C. Ye, J. Lu, F.X. Liu, P.K. Liaw, Acta Materialia, 57 (2009) 1613-1623.

[112] J.C. Ye, J. Lu, Y. Yang, P.K. Liaw, Intermetallics, 18 (2009) 385-393.

[113] Y. Choi, H.S. Lee, D. Kwon, Journal of Materials Research, 19 (2004) 3307-3315.

[114] W.F. Wu, Z. Han, Y. Li, Applied Physics Letters, 93 (2008).

[115] C. Fan, D. Chen, P.K. Liaw, H. Choo, C. Benmore, J. Siewenie, G.L. Chen, J.X. Xie, C.T. Liu, Applied Physics Letters, 93 (2008) 3.

[116] C.A. Angell, Science, 267 (1995) 1924-1935.

[117] B. Frick, D. Richter, Science, 267 (1995) 1939-1945.

[118] B. Jerome, J. Commandeur, Nature, 386 (1997) 589-592.

[119] P.G. Debenedetti, F.H. Stillinger, Nature, 410 (2001) 259-267.

[120] J.Y. Cavaille, J. Perez, G.P. Johari, Physical Review B, 39 (1989) 2411-2422.

[121] K.L. Ngai, P. Lunkenheimer, C. Leon, U. Schneider, R. Brand, A. Loidl, Journal of Chemical Physics, 115 (2001) 1405-1413.

[122] J. Perez, J.Y. Cavaille, L. David, Journal of Molecular Structure, 479 (1999) 183-194.

[123] K. Kaminski, E. Kaminska, M. Paluch, J. Ziolo, K.L. Ngai, Journal of Physical Chemistry B, 110 (2006) 25045-25049.

[124] C. Gainaru, R. Bohmer, R. Kahlau, E. Rossler, Physical Review B, 82 (2010) 104205.

[125] J.S. Harmon, M.D. Demetriou, W.L. Johnson, K. Samwer, Phy. Rev. Lett., 99 (2007) 135502.

[126] A. Concustell, J. Sort, A.L. Greer, M.D. Baro, Appl. Phys. Lett., 88 (2006) 171911.

[127] Y. Yang, J.C. Ye, J. Lu, P.K. Liaw, C.T. Liu, Appl. Phys. Lett., 96 (2010) 011905.

[128] Y.H. Liu, D. Wang, K. Nakajima, W. Zhang, A. Hirata, T. Nishi, A. Inoue, M.W. Chen, Phy. Rev. Lett., 106 (2011) 125504.

[129] D.B. Miracle, T. Egami, K.M. Flores, K.F. Kelton, MRS Bulletin 32 (2007) 629-634.

[130] C. Fan, P.K. Liaw, C.T. Liu, Intermetallics, 17 (2009) 86-87.

[131] A.S. Argon, Acta Metall. Mater., 27 (1979) 47-58.

[132] Y.C. Lo, H.S. Chou, Y.T. Cheng, J.C. Huang, J.R. Morris, P.K. Liaw, Intermetallics, 18 (2010) 954-960.

[133] I.M. Ward, J. Sweeney, An introduction to the mechanical properties of solid polymers, 2nd ed., John Wiley & Sons, Ltd, 2004.

[134] H.B. Yu, W.H. Wang, H.Y. Bai, Y. Wu, M.W. Chen, Phy. Rev. B, 81 (2010) 220201(R).

[135] J.C. Ye, J. Lu, C.T. Liu, Q. Wang, Y. Yang, Nature Mater., 9 (2010) 619-623.

[136] Y. Yang, J.F. Zeng, J.C. Ye, J. Lu, Appl. Phys. Lett., 97 (2010) 261905.

[137] M.L. Falk, J.S. Langer, Phy. Rev. E, 57 (1998) 7192-7205.

[138] F. Spaepen, Acta Metall., 25 (1977) 407-415.

[139] T. Egami, JOM, 62 (2010) 70-75.

[140] A. Hirata, P. Guan, T. Fujita, Y. Hirotsu, A. Inoue, A.R. Yavari, T. Sakurai, M.W. Chen, Nature Mater., 10 (2010) 28-33.

[141] M.D. Uchic, D.M. Dimiduk, J.N. Florando, W.D. Nix, Science, 305 (2004) 986-989.

[142] Y. Yang, J. Ye, J. Lu, F. Liu, P. Liaw, Acta Mater., 57 (2009) 1613-1623.

[143] Y. Yang, J.C. Ye, J. Lu, F.X. Liu, P.K. Liaw, Acta Mater., 57 (2009) 1613-1623.

[144] C.J. Lee, J.C. Huang, T.G. Nieh, Appl Phys Lett, 91 (2007) 161913.

[145] B. Schuster, Q. Wei, T. Hufnagel, K. Ramesh, Acta Materialia, 56 (2008) 5091-5100.

[146] O.P. Bobrov, V.A. Khonik, S.N. Laptev, M.Y. Yazvitsky, Scr. Mater., 49 (2003) 255-260.

[147] Y. Zhang, A.L. Greer, Appl. Phys. Lett., 89 (2006) 3.

[148] S.X. Song, H. Bei, J. Wadsworth, T.G. Nieh, Intermetallics, 16 (2008) 813-818.

[149] A. Vinogradov, Scripta Materialia, 63 (2010) 89-92.

[150] W. Dmowski, T. Iwashita, C.-P. Chuang, J. Almer, T. Egami, Phy. Rev. Lett., 105 (2010) 205502.

[151] C.A. Schuh, A.C. Lund, T.G. Nieh, Acta Mater., 52 (2004) 5879-5891.

[152] S.X. Song, T.G. Nieh, Intermetallics, 17 (2009) 762-767.

[153] Y. Yang, J.C. Ye, J. Lu, Y.F. Gao, P.K. Liaw, JOM-US, 62 (2010) 93-98.

[154] F.F. Wu, Z.F. Zhang, S.X. Mao, Acta Mater., 57 (2009) 257-266.

[155] J.W. Yeh, Annales De Chimie-Science Des Materiaux, 31 (2006) 633-648.

[156] W.H. Wu, C.C. Yang, J.W. Yeh, Annales De Chimie-Science Des Materiaux, 31 (2006) 737-747.

[157] J.W. Yeh, S.K. Chen, S.J. Lin, J.Y. Gan, T.S. Chin, T.T. Shun, C.H. Tsau, S.Y. Chang, Advanced Engineering Materials, 6 (2004) 299-303.

[158] X.F. Wang, Y. Zhang, Y. Qiao, G.L. Chen, Intermetallics, 15 (2007) 357-362.

[159] H.Y. Chen, C.W. Tsai, C.C. Tung, J.W. Yeh, T.T. Shun, C.C. Yang, S.K. Chen, Annales De Chimie-Science Des Materiaux, 31 (2006) 685-698.

[160] C.J. Tong, Y.L. Chen, S.K. Chen, J.W. Yeh, T.T. Shun, C.H. Tsau, S.J. Lin, S.Y. Chang, Metallurgical and Materials Transactions A, 36 (2005) 881-893.

[161] J.W. Yeh, S.K. Chen, J.Y. Gan, S.J. Lin, T.S. Chin, T.T. Shun, C.H. Tsau, S.Y. Chang, Metallurgical and Materials Transactions a-Physical Metallurgy and Materials Science, 35A (2004) 2533-2536.

[162] C.Y. Hsu, W.R. Wang, W.Y. Tang, S.K. Chen, J.W. Yeh, Advanced Engineering Materials, 12 44-49.

[163] G.Y. Ke, S.K. Chen, T. Hsu, J.W. Yeh, Annales De Chimie-Science Des Materiaux, 31 (2006) 669-683.

[164] Y. Zhang, G.L. Chen, L. Gan, Journal of ASTM International, 7 (2010) Paper ID: JAI102527

[165] S. Singh, N. Wanderka, B.S. Murty, U. Glatzel, J. Banhart, Acta Materialia, doi: 10.1016/j.actamat. 2010.09.023 (2010).

[166] C.J. Tong, M.R. Chen, S.K. Chen, J.W. Yeh, T.T. Shun, S.J. Lin, S.Y. Chang, Metallurgical and Materials Transactions a-Physical Metallurgy and Materials Science, 36A (2005) 1263-1271.

[167] C.W. Tsai, M.H. Tsai, J.W. Yeh, C.C. Yang, Journal of Alloys and Compounds, 490 160-165.

[168] U.S. Hsu, U.D. Hung, J.W. Yeh, S.K. Chen, Y.S. Huang, C.C. Yang, Materials Science and Engineering A-Structural Materials Properties Microstructure and Processing, 460 (2007) 403-408.

[169] T.E. Mason, D. Abernathy, I. Anderson, J. Ankner, T. Egami, G. Ehlers, A. Ekkebus, G. Granroth, M. Hagen, K. Herwig, J. Hodges, C. Hoffmann, C. Horak, L. Horton, F. Klose, J. Larese, A. Mesecar, D. Myles, J. Neuefeind, M. Ohl, C. Tulk, X.L. Wang, J. Zhao, Physica B-Condensed Matter, 385-86 (2006) 955-960.

[170] X.L. Wang, T.M. Holden, G.Q. Rennich, A.D. Stoica, P.K. Liaw, H. Choo, C.R. Hubbard, Physica B-Condensed Matter, 385 (2006) 673-675.

[171] X.L. Wang, T.M. Holden, A.D. Stoica, K. An, H.D. Skorpenske, A.B. Jones, G.Q. Rennich, E.B. Iverson, Materials Science Forum, 652 (2010) 105-110.

[172] J.R. Greer, W.C. Oliver, W.D. Nix, Acta Materialia, 53 (2005) 1821-1830.

[173] J.W. Yeh, S.Y. Chang, Y.D. Hong, S.K. Chen, S.J. Lin, Materials Chemistry and Physics, 103 (2007) 41-46.

[174] S. Singh, N. Wanderka, B.S. Murty, U. Glatzel, J. Banhart, Acta Materialia, In Press, Corrected Proof (2010).

[175] A. Takeuchi, A. Inoue, Materials Transactions, 46 (2005) 2817-2829.

[176] J.C. Ye, J. Lu, Y. Yang, P.K. Liaw, Intermetallics, 18 385-393.

[177] H. Bei, S. Shim, E.P. George, M.K. Miller, E.G. Herbert, G.M. Pharr, Scripta Materialia, 57 (2007) 397-400.

[178] D. Henkel, A.W. Pense, Structure and Properties of Engineering Materials (5th Edition), McGraw-Hill, New York, 2001.

[179] M.D. Uchic, P.A. Shade, D.M. Dimiduk, Annual Review of Materials Research, 39 (2009) 361-386.

[180] E.M. Nadgorny, D.M. Dimiduk, M.D. Uchic, Journal of Materials Research, 23 (2008) 2829-2835.

[181] S.I. Rao, D.M. Dimiduk, T.A. Parthasarathy, M.D. Uchic, M. Tang, C. Woodward, Acta Materialia, 56 (2008) 3245-3259.